

© 2016 by Jaseung Ku. All rights reserved.

MEISSNER QUBIT: ARCHITECTURE, CHARACTERIZATION AND
VORTEX-PROBING APPLICATIONS

BY
JASEUNG KU

DISSERTATION

Submitted in partial fulfillment of the requirements
for the degree of Doctor of Philosophy in Physics
in the Graduate College of the
University of Illinois at Urbana-Champaign, 2016

Urbana, Illinois

Doctoral Committee:

Professor James Eckstein, Chair
Professor Alexey Bezryadin, Director of Research
Professor Jon Thaler
Assistant Professor Bryan Clark

Abstract

Quantum computing has drawn enormous attention in physics community in both scientific and technological perspectives. Among several promising architectures for quantum computer are superconducting qubits based on Josephson junctions. Over the last few decades, there has been a dramatic improvement on the coherence time by a few orders of magnitude from a few nanoseconds to about a hundred microsecond. Such improvements were possible due to the elimination or suppression of various decoherence sources. Thus, it is critical to investigate the origin of such decoherence to extend our understanding and practically improve the coherence time. For example, Abrikosov vortices knowingly could be one of the decoherence source, and yet the quantitative research on the interaction of a superconducting qubit with such vortices has been lacking.

We present a new type of transmon split-junction qubit which can be tuned by Meissner screening currents in the adjacent superconducting film electrodes. The qubits were measured using a 3D microwave cavity in the dispersive regime at the base temperature 45 mK. The measurement protocols were based on the circuit quantum electrodynamics (cQED) architecture and so-called high-power measurement. The achieved period of oscillation with magnetic field was much smaller than in usual SQUID-based transmon qubits, thus a strong effective field amplification has been realized. The best measured relaxation time was of the order of 50 μ s and the dephasing time about 40 μ s. This Meissner qubit allows an efficient coupling to superconducting vortices, which were induced by external applied magnetic field. We intend to present a quantitative analysis of the radiation-free energy relaxation in the qubits coupled to the Abrikosov vortices. The estimated relaxation rate combined with vortex counting process provided a good agreement with the experimental results. Also, the observation of coherent quantum oscillations provides strong evidence that vortices can exist in coherent quantum superposition of different position states. According to our suggested model, the wave function collapse is defined by Caldeira-Leggett dissipation associated with viscous motion of the vortex cores.

To my wife.

Acknowledgments

First, I would like to thank my advisor, Alexey Bezryadin, who helped me pursue my Ph.D work. He brought in the new research area of superconducting qubits and microwave measurement technique to our lab. I have to say I became very interested in the new research field, and without him I would not have been able to start working on such interesting physics research. Also, I really enjoyed discussing various ideas on interesting projects with him and learned how important physical intuition could be in performing scientific research. I would like to thank previous group members of Bezryadin group, Robert Dinsmore, Mitrabanu Sahu, Ulas Coskun, Thomas Aref, and Matthew Brenner for showing and training me various experimental skills of, not limited to, DC transport measurement and nanofabrication. They were always willing to help me and provide helpful feedbacks. Also, I would like to acknowledge current group members for fruitful discussion and feedback. Regarding my main Ph.D work, I would like to thank Zack Yoscovits for fabricating precious samples for me, and thank James Eckstein and Alex Levchenko for all the discussion and feedback on the manuscript for publication. I would like to thank Russell Giannetta for allowing me to take over his dilution refrigerator from his lab. Without that refrigerator system, my Ph.D research on superconducting qubits would not have been possible to conduct since it is an essential equipment in low temperature physics research, in particular, qubits. Also he showed me how to run the refrigerator and gave technical advice whenever I encountered equipment problems. I would like to acknowledge the staffs in the Center for Microanalysis and Materials (CMM) and Micro/Nanofabrication Facility in the Frederick Seitz Materials Research Laboratory (MRL), for helping me to operate state-of-art instruments to fabricate and analyzing nano-fabricated samples. Also, they provided professional trainings and technical support for me to operate the instruments without any difficulty. Finally, in particular, I would like to thank my wife, Jiin Choi, for her endless support and love in all aspects. This work was supported by the National Science Foundation under the Grant No. ECCS-1408558 and ECCS-1407875.

Table of Contents

Chapter 1	Introduction	1
1.1	Quantum computing: quantum bit	1
1.2	Superconducting qubits	3
1.3	Transmon and Meissner qubit	4
1.4	2D and 3D circuit quantum electrodynamics (cQED)	5
1.5	Thesis overview	6
Chapter 2	Superconducting qubit and 3D circuit quantum Electrodynamics	8
2.1	Superconducting qubits	8
2.1.1	Quantum circuit as a qubit	8
2.1.2	Description of two level systems	10
2.1.3	Rabi oscillations	13
2.1.4	Relaxation time, Ramsey fringe, and spin echo measurement	17
2.2	Transmon qubit	21
2.3	3D circuit quantum electrodynamics (cQED)	25
2.3.1	circuit quantum electrodynamics	25
2.3.2	Dispersive measurement	28
2.3.3	Readout of transmon in dispersive regime	28
2.4	Rectangular microwave cavity resonator	30
Chapter 3	Sample fabrication	33
3.1	Meissner transmon	33
3.1.1	Substrate preparation	33
3.1.2	e-beam lithography and removal of residue	34
3.1.3	Deposition and post-deposition process	35
3.2	Design rules and parameters of transmon	36
Chapter 4	Experimental setup and preparation	38
4.1	Microwave setup in cryogenics	38
4.1.1	Cryogenic wiring: RF	38
4.1.2	Cryogenic wiring: DC	42
4.1.3	Noise filtering	44
4.2	Microwave room-temperature electronics setup	44
4.2.1	Pulse generation: microwave modulation	44
4.2.2	Readout: microwave demodulation	46
4.3	Measurement preparation: sample mounting and cool-down	49
4.3.1	Copper cavity resonator	49
4.3.2	Superconducting solenoid	49
4.3.3	Sample mounting and preparation for cool-down	52
4.3.4	Sample cool-down in dilution fridge	52

Chapter 5	Frequency-domain measurement of Meissner qubit	57
5.1	Transmission measurement of cavity-qubit system	59
5.2	Calibrating drive power: high-power measurement	60
5.3	Spectroscopy	62
5.4	Magnetic field dependence of transmission	64
5.5	Periodicity of qubit frequency oscillation	67
5.6	Magnetic field dependence of Meissner qubit frequency	69
Chapter 6	Time-domain measurements of Meissner qubit	72
6.1	Rabi oscillation measurement	72
6.1.1	Calibrating π and $\pi/2$ pulses	75
6.2	Relaxation time, Ramsey fringe and Hahn spin echo measurement	77
6.2.1	Relaxation time measurement	77
6.2.2	Ramsey fringe measurement	78
6.2.3	Hahn spin echo measurement	80
6.3	Low magnetic field	81
6.4	High magnetic field	83
6.5	Relaxation rate	86
6.6	Vortex counting and vortex-qubit interaction	86
Chapter 7	Conclusion	93
Appendix A	Recipe	94
A.1	Stainless steel powder filter	94
A.2	Infrared-absorbing material	96
Appendix B	Measuring on/off ratio of microwave pulses	98
Appendix C	Influence of microwave leakage on time-domain measurement	101
Appendix D	Creating a phase-tunable microwave pulse	103
Appendix E	Quantum mechanical description in a rotating frame	104
References		105

Chapter 1

Introduction

1.1 Quantum computing: quantum bit

Quantum computing is a framework of computation that makes use of quantum mechanical phenomena. As theoretically proposed, quantum computation to solve problems can be performed utilizing a superposition and entanglement of quantum states. Unlike a conventional classical digital computing based on traditional transistors where ‘0’ and ‘1’ form a classical bit, quantum computing or a quantum computer utilizes so-called quantum bits as a basic building block to solve various problems much faster than classical computers can possibly do with best algorithm. Quantum bits comprise of a superposition state $|\Phi\rangle$ of two quantum eigenstates, say, ground and excited state, denoted by $|0\rangle$ and $|1\rangle$ with energy E_0 and E_1 , respectively (see Fig. 1.1(a)). The qubit state $|\Phi\rangle$ is commonly represented in so-called Bloch sphere, a geometrical representation of the qubit on the surface of the sphere. Any qubit state can be parametrized by two angles θ and ϕ as shown in Fig. 1.1(b) (more details in Sec. 2.1.2).

Such quantum bits in large scale combined with quantum algorithms have enormous potential to solve problems that would not be possible to solve with classical computers in practical time frame. Quantum algorithm can offer exponential speed-up of computation and in some case polynomial speed-up. Such potentials have sparked the general interest and motivation to building quantum bits, eventually, quantum computers, in both theoretical and experimental manner. For example, in 1994, Shor’s algorithm [1], a quantum algorithm named after mathematician Peter Shor, was formulated and shown to be capable of finding prime factors—i.e., integer factorization—much more efficiently than any currently existing classical factoring algorithm. This could be critical in the field of cryptography for security purpose. Also, Grover’s algorithm [2, 3], another quantum algorithm, was shown to search a database quadratically faster than classical algorithm. Another field arising recently related with quantum computing is quantum simulation as initiated by Richard Feynman [4], who introduced an idea of using quantum computers for quantum simulation.

The first step toward building a quantum computer is to build quantum bits—qubits. A qubit is basically

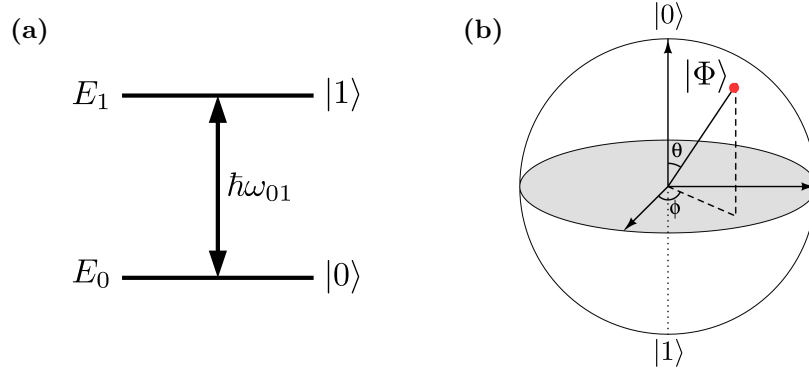


Figure 1.1: (a) Energy diagram of a two-level quantum system with two energy states. $|0\rangle$ denotes the ground state with energy E_0 and $|1\rangle$ the excited state with energy E_1 . The energy difference is $\hbar\omega_{01}$, where ω_{01} is the qubit transition frequency. A general qubit state is denoted as $|\Phi\rangle$. (b) A Bloch sphere representation of a qubit state $|\Phi\rangle = [\cos(\theta/2)]|0\rangle + [\sin(\theta/2)e^{i\phi}]|1\rangle$. The Bloch sphere is commonly used to graphically represent the qubit state on the surface of the sphere. The qubit state can be parametrized by two angles θ and ϕ . The north pole and south pole represent $|0\rangle$ and $|1\rangle$, respectively.

a quantum system with two accessible energy states, which serves as an artificial atom. Such qubits can be realized in different quantum systems and there have been extensive research on the quantum bits using different physical systems during the last few decades. Some examples are superconducting qubit [5], spin qubit [6], trapped ion qubit [7], and more. What distinguishes the different types of qubits is what forms two qubit states. For example, in the spin qubit, a single electron spin trapped in a potential well and embedded in a semiconductor under magnetic field can have two energy states by the Zeeman effect, forming a qubit, while in the trapped ion qubit, the ionized atoms with two hyperfine ground states form a qubit.

There are multiple stages toward implementing real quantum computing [5]. The first and second stage are qubit operation on single physical qubits, and quantum algorithm on multiple physical qubits (entangled states). To achieve these two stages, the qubits should satisfy five requirements called DiVincenzo's criteria [8]. They are listed here:

1. A scalable physical system with well characterized qubits.
2. The ability to initialize the state of the qubits to a simple fiducial state, such as $|000\dots\rangle$.
3. Long relevant decoherence times, much longer than the gate operation time.
4. A “universal” set of quantum gates.
5. A qubit-specific measurement capability.

First, a qubit system should be scalable, i.e., one qubit is not enough, but many qubits for quantum computing. Second, the qubit should be able to be initialized, analogous to resetting an 8-bit IC register

chip to all zero. Third, the qubit should have longer coherence time than gate operation time—qubit should hold its superposition state without losing coherence before gate operations or computations are finished. Fourth, like a set of logic operations on digital chips, the qubit needs to have a universal set of quantum gate that can work on any qubit system and manipulate the qubit state. Fifth, there should be method/measurement by which each qubit can be selectively addressed.

The third stage requires quantum error corrections [9], and this has been demonstrated recently in several qubit systems. The research on the qubits has been driven to make process toward meeting the DiVincenzo criteria at least, and even some qubit systems are on a verge to reach the higher stages. Among such qubits is the superconducting qubit, one of the most promising system in the race for successful implementation of quantum computing.

1.2 Superconducting qubits

Several promising architectures for quantum computers are based on the superconducting qubits [10, 11, 12] based on Josephson junctions (JJs). These superconducting qubits are normally macroscopic solid-state objects, consisting of normal or superconducting films and Josephson junctions. Usually, the size of an object becomes smaller and smaller, the object starts to exhibit quantum mechanical behavior, and the energy levels becomes quantized like in a quantum dot—1D potential well. However, such system is susceptible to decoherence of quantum states due to microscopic degree of freedom easily interacting with environmental noise. However, since the superconducting qubits have the *macroscopic* degree of freedom or macroscopic quantum variable, e.g. phase difference across the JJ, they exhibit much improved quantum coherence—harder to disturb such quantum system by environmental noise. The “quantum circuit” of the superconducting qubits utilize either charge [13], phase [14] or flux [15, 16] degrees of freedom. These systems have made tremendous progress in recent years in realizing increasingly sophisticated quantum states, measurements and operations with high fidelity [5]. Superconducting qubits are also attractive technologically because they can be naturally integrated into large-scale quantum circuits [17, 18] and are relatively easy to couple to external control circuits with strong coupling. However, this main advantage of superconducting qubits brings a substantial challenge at the same time since strong coupling also implies a substantial interaction between the qubits and their environment, which can break quantum coherence. The presence of Abrikosov vortices is one important example of such environment. Understanding the limiting factors of qubit operation is of fundamental and practical importance. Previously a separation of various contributing factors to the qubit relaxation and decoherence has been achieved [19, 20, 21, 22]. Dissipation

caused by vortices has also been studied, but not in a qubit setting [23]. We studied Meissner qubits to quantify dissipation effects produced by single vortices.

In characterizing the superconducting qubits, one of the most important characteristics is the coherence time, called T_2 . It is the time scale over which a qubit loses the phase coherence between the ground and excited state, i.e., there is no definite phase difference between the coefficients of $|0\rangle$ and $|1\rangle$. For example, one of the limiting factors for the coherence time is the relaxation process by which the excited state of the qubit relaxes down to the ground state, losing energy. Also, the infinitesimal energy exchange of the qubit with environment causes the loss of the coherence, since the qubit energy difference between the ground and excited state fluctuates. Over the last several decades, there have been dramatic improvement on such coherence time by orders of magnitude from nanoseconds to microseconds [24]. Yet, it is still important to investigate remaining decoherence mechanism for further improvement on the time scales.

1.3 Transmon and Meissner qubit

A major advance in the superconducting qubit performance became possible after the invention of the *transmon qubit* in Yale university [25]. The transmon is basically a type of the charge qubit with a large shunt capacitance across JJ so that it can be operated in different parameter regime. This new design allowed one to achieve much longer coherence time (a few hundreds μ s) than the previous charge qubit, by making the transmon much less sensitive to the charge noise—major dephasing source of the charge qubit. When combined with this three-dimensional circuit-quantum electrodynamics (cQED) platform developed in Ref. [26], the transmon has shown huge improvements of the coherence time, even up to several hundreds microseconds [27, 24].

Meanwhile, one interesting theoretical possibility of drastically improving quantum coherence in qubits is to couple them to Majorana fermions [28, 29]. A qubit based on Majorana states is expected to exhibit especially long coherence times. One approach to create Majorana states is to deposit a superconductor onto a topological insulator and to create vortices in the superconductor. In this case Majorana states can nucleate in the vortex core [28]. Thus a study of qubits coupled to vortices is needed, in order to determine whether a qubit coupled to a vortex can preserve its quantum coherence and for how long, which is one of the motivations of our study.

Like the common transmon, our device involves two Josephson junctions with a large shunt capacitance. The main difference is that our qubit is coupled to the Meissner current and the supercurrents generated by vortices—thus we call our device “Meissner qubit”. Because in our qubit design the Meissner current is

allowed to flow, partially, into the qubit, a significant amplification of the magnetic field effect is demonstrated. The qubit transition frequency is periodically modulated by the applied magnetic field, but the period is much smaller compared to the value estimated by dividing the flux quantum by the qubit loop geometric area.

The Meissner qubit allows a strong coupling to the vortices in the leads. Yet the relaxation time of such device, designed to probe the environment, is rather large, namely about $50\ \mu\text{s}$ in the best case. We performed a detailed study of the radiation-free decoherence effects produced by the vortex cores. It should be stressed that the qubit relaxation time may be shortened by the presence of a vortex in the superconducting film, due to the Bardeen-Stephan viscous vortex flow. No quantitative study has been done so far to test how qubit quantum states relax due to coupling to Abrikosov vortices. Our key finding is that vortices can remain, over many microseconds, in quantum superposition states generated, because the Lorentz force experiences strong quantum fluctuations. The relaxation rate added to the qubit by each single vortex was measured and appears to be surprisingly low, of the order of 10 kHz. We propose a semi-quantitative model which allows us to estimate this radiation-free relaxation rate caused by viscous flow of vortices. Up until now it was well established that classical supercurrents can generate heat through viscous flow of vortices [23]. Now we establish that quantum superposition currents, such as those existing in qubits and characterized by zero expectation value, can also generate heat through the same mechanism. Such heat dissipation occurs through the spread of the wavefunction of the vortex center followed by a collapse of this smeared wave function.

1.4 2D and 3D circuit quantum electrodynamics (cQED)

The transmon qubit was originally measured using a two dimensional superconducting resonator which can be strongly coupled to the transmon. The quantum circuit consisting of a qubit and superconducting coplanar waveguide (CPW) resonator acting as a harmonic oscillator is analogous to an atom in an optical cavity system in quantum electrodynamics (QED). As the research on the interaction of atoms with optical photons is called quantum electrodynamics (QED), the new measurement scheme, based on the strong coupling of microwave photons in the resonator with the artificial atom—qubit, was named *circuit quantum electrodynamics* (cQED). The first demonstration of the strong coupling in the cQED was done by Wallraff et al. [30] in Yale university, and they showed that the qubit and single photon can exchange energy quanta with the rate g (rad/s)—this phenomenon is called vacuum Rabi oscillation—when they are in resonance, i.e., qubit transition frequency is equal to the photon frequency. The strong coupling means that the exchange

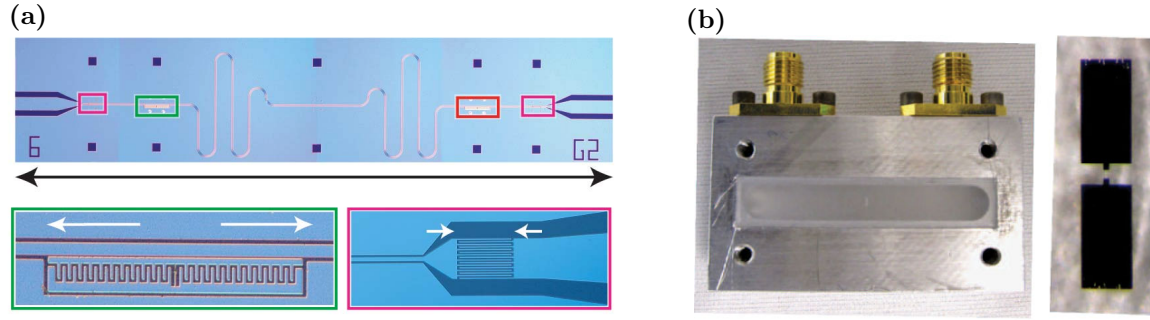


Figure 1.2: (a) A photograph of a 2D coplanar waveguide (CPW) superconducting resonator with a transmon capacitively coupled to the center conductor line of the resonator. In the bottom left picture, the interdigital structure acts as a shunt capacitor. The bottom right picture represent a coupling capacitor of the resonator to external RF transmission line. This figure was taken from Ref. [31]. (b) A photograph of a 3D aluminium superconducting cavity. Two SMA connectors in gold serve as input and output port. The picture on the right is the transmon on sapphire substrate. Two rectangles serve as an RF antenna as well as a shunt capacitor. One Josephson junction (not visible) bridges the two rectangular films. For measurement, the transmon is placed in the center of the cavity space, where the fundamental cavity mode has the strongest dipole coupling. The picture was taken from Ref. [26].

rate is faster than both the decay rate of the qubit (inverse of lifetime) and the leak rate of the photons—photons can leak through “mirrors”, the interface between the resonator and outside world. The advantage of the cQEC measurement scheme comes when the technique is used to detect the qubit state. When the qubit transition frequency ω_{01} is far from the resonant frequency ω_r of the resonator such that the difference is much greater than the coupling frequency g , i.e., $|\omega_q - \omega_r| \gg g$, the system is said to be in the *dispersive* regime. In the dispersive regime, the resonant frequency is pulled via the qubit-resonator interaction by $\pm\chi$, i.e., $\omega_r \rightarrow \omega_r \pm \chi$, and such shift depends on the qubit state (see Sec. 2.3.1). Therefore, the measurement of the resonant frequency can be used for detecting the qubit state. In addition, the dispersive measurement in cQED is known to be quantum non-demolition (QND) measurement, meaning that once the qubit is projected to either $|0\rangle$ and $|1\rangle$ state, the subsequent measurement provides the same result when repeated.

Since the cQED technique was developed, it became quite successful in measuring other types of qubits as well [32, 33]. Later, instead of the two dimensional resonator, a three dimensional superconducting cavity was used to measure the transmon, demonstrating greatly improved quantum coherence, up to an order of $100 \mu s$ [26, 27]. Two representative pictures of the transmon in 2D and 3D resonator are shown in Fig. 1.2 as an example.

1.5 Thesis overview

Starting from the next chapter, detailed description of the Meissner qubits will be given including theoretical background, sample fabrication, experimental setup, experimental results, and conclusion. Specifically, in

Chap. 2, a general description of the superconducting qubit will be given, including quantum circuit as a qubit, quantum mechanical description of a two-level system (qubit), its dynamical behavior under harmonic irradiation (qubit manipulation), and conventional measurement techniques used to measure three important time scales. In the following sections, the principles of the transmon qubit, circuit quantum electrodynamics (cQED), and microwave cavity will be given for theoretical background.

In Chap. 3, the procedures of sample fabrication will be given briefly in three categories: substrate preparation, patterning with e-beam lithography, and deposition of superconducting films. Also, importantly, the design rules for the fabrication of transmons are presented to give an idea of how to choose appropriate circuit parameters.

In Chap. 4, all the details on the experiment setup and measurement preparation will be explained. This chapter includes the cryogenic setup for microwave measurement in the dilution refrigerator, microwave room-temperature electronics, and measurement preparation steps. In particular, it is important to understand how to create microwave pulses and how to use them to measure the transmission of microwave cavity, which serves as a detection technique of our qubits.

In Chap. 5, we will present main experimental results, in particular, the frequency-domain measurement of the Meissner qubit. We will investigate the spectrum of and the magnetic dependence of the Meissner qubits in the low range of the magnetic field—not high enough to have vortices strongly interacting with the qubit. This chapter will provide not only the characterization of the Meissner qubit in frequency domain, but also actual qubit measurement scheme in the cQED architecture.

In Chap. 6, we will move on to the time-domain measurement of the Meissner qubit—study of dynamical behavior. The time-domain measurement requires solid understanding of how Rabi oscillation measurement works. Then three different types of measurement required to obtain three time scales will be provided. In the rest of the chapter, we will delve into the time-domain characteristics of the Meissner qubit in the low and high magnetic field. In the latter case, we focus on investigating the interaction of the qubit with the induced vortices. In particular, the relaxation process caused by such interaction will be presented in detail, including vortex counting and estimation of relaxation rate.

Finally, we will end the thesis with summarizing the results and providing future outlook. In appendix, useful miscellaneous information will be presented, which would be too technical and detailed to be included in the main text. At the end of the appendix comes a list of references.

Chapter 2

Superconducting qubit and 3D circuit quantum Electrodynamics

2.1 Superconducting qubits

In this chapter, we will give theoretical background on a two-level system and 3D circuit QED architecture. First, the concept of quantum circuit is explained, followed by a quantum mechanical description of the qubit and its time-evolution. The time-evolution of the qubit under harmonic irradiation—Rabi oscillation—and the measurement principles to obtain three characteristic scales are illustrated. Then the transmon qubit theory as well as 3D circuit QED measurement technique are explained in detail. Finally, a rectangular microwave cavity is presented.

2.1.1 Quantum circuit as a qubit

Quantum circuits are solid state electrical circuits whose behavior should be described quantum mechanically. These circuits are governed by *macroscopic* degree of freedom rather than microscopic degree of freedom like in a hydrogen atom. The electrical circuit's classical variables should be treated as quantum mechanical variables. A simple example of the quantum circuit would be a simple LC-circuit as shown in Fig. 2.1(a). The Hamiltonian of this system can be written by

$$H = \frac{Q^2}{2C} + \frac{\Phi^2}{2L}, \quad (2.1)$$

where C is capacitance, L inductance, Q charge stored in the capacitor, and Φ magnetic flux created in the inductor. Quadratic in Q and Φ , this Hamiltonian represents a simple harmonic oscillator. When two classical variables Q and L are treated quantum mechanically, they become operators that satisfies the commutation relation $[\Phi, Q] = i\hbar$. Since the Hamiltonian is quadratic, it can be simplified to, using creating and annihilating operator a^\dagger and a

$$H = \hbar\omega_0 \left(a^\dagger a + \frac{1}{2} \right), \quad (2.2)$$

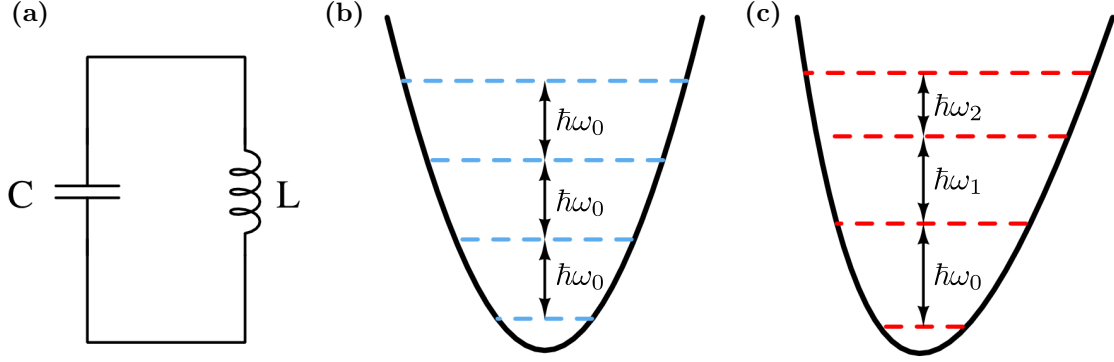


Figure 2.1: (a) A schematic of a simple LC circuit of a capacitor (C) and inductor (L). In quantum mechanical description, the charge Q in the capacitor and flux Φ in the inductor becomes canonical variables with a commutation relation, $[\Phi, Q] = i\hbar$. The charging energy and inductive energy play a role of kinetic and potential energy, respectively. (b) A diagram of quadratic potential energy and quantized energy level in a harmonic oscillator. The energy spacing is equal to $\hbar\omega_0$. (c) A diagram of an anharmonic potential energy. The energy difference is not equal any more, i.e., $\hbar\omega_0 \neq \hbar\omega_1 \neq \hbar\omega_2$ and thus, the lowest and second lowest energy levels can be used as a qubit.

, where $a = (1/\sqrt{2\hbar})[(L/C)^{1/4}Q - i(C/L)^{1/4}\Phi]$. The quantized energy states are shown in Fig. 2.1(b). However, the energy states are equally spaced, so the harmonic oscillator can not work as a qubit since it is not possible to address only two states. Thus, it is necessary to make unequal energy states. To make a qubit, we need to make the system *anharmonic*—a nonlinear element is required. Typically, a Josephson junction (JJ) substitutes for the linear inductor in conventional JJ-based superconducting qubits because the JJ serves as a nonlinear as well as non-dissipative inductor.

Meanwhile, a superconducting nanowire was investigated as another potential nonlinear element to realize a superconducting nanowire qubit in Ref. [34, 35]. Unfortunately, the research has not been led to implementing a working nanowire qubit so far. However, the study of the nonlinear property of the nanowire was branched out to the observation of single phase slips, coupled to a coplanar waveguide (CPW) superconducting resonator [36]. Still, the superconducting nanowire may hold promise for a useful element in building better qubits, as demonstrated in the coherent phase-slip qubit [37, 38, 39].

A typical JJ widely used in the superconducting qubits is a Josephson tunnel junction made of a thin aluminium oxide layer sandwiched by two aluminium films. Such JJ is characterized by a critical current I_c and a junction capacitance C_J . Supercurrent can flow through JJ by Josephson effect [40], even though there is an insulating layer. The amplitude of the supercurrent I_s depends on the phase difference φ between order parameters in two electrodes, and determined by a sinusoidal current-phase-relationship (CPR),

$$I_s = I_c \sin(\varphi). \quad (2.3)$$

The inductance L of the JJ can be calculated in the following:

$$L = \left(\frac{dI_s}{d\Phi} \right)^{-1} \quad (2.4)$$

$$= \frac{\Phi_0}{2\pi} \left(\frac{dI_s}{d\varphi} \right)^{-1} \quad (2.5)$$

$$= \left(\frac{\Phi_0}{2\pi I_c} \right) \frac{1}{\cos(\varphi)}, \quad (2.6)$$

where $\Phi = \int V dt = \int [\hbar/(2e)] \dot{\varphi} dt = \Phi_0(\varphi/(2\pi))$ ¹, and $L_J \equiv \Phi_0/(2\pi I_c)$ is called Josephson inductance.

Therefore, the inductance of a JJ is a nonlinear element, i.e., L depends on I_s .

Meanwhile, the total energy stored in the JJ, E , is given by,

$$E = \int V \cdot I_s dt = \left(\frac{\hbar I_c}{2e} \right) \int \dot{\varphi} \sin(\varphi) dt = \left(\frac{\hbar I_c}{2e} \right) \int \sin(\varphi) d\varphi = -E_J \cos(\varphi) + C, \quad (2.7)$$

where $E_J \equiv \hbar I_c/(2e)$ is called the Josephson energy.

Now that the inductor in Fig 2.1(a) is replaced with the Josephson junction, and the new Hamiltonian becomes,

$$H = \frac{Q^2}{2C} - E_J \cos \varphi. \quad (2.8)$$

The second term can be seen as a potential energy of the Josephson junction, and obviously it is not harmonic. The new Hamiltonian is in fact the Hamiltonian of the transmon qubit, which we will describe in more detail in Sec 2.2.

2.1.2 Description of two level systems

In this section, we provide general quantum mechanical description of a two-level system—qubit. The description of the two-level system is equivalent to that of a spin-1/2 system in a static magnetic field. Thus the mathematical framework used to describe the spin system can be applied to the qubit in the same way. We consider two energy states separated by energy difference $\hbar\omega_0$. The two energy eigenstates are denoted by $|0\rangle$ and $|1\rangle$ with E_0 and E_1 eigenvalues, so that $\Delta E = E_1 - E_0 = \hbar\omega_0$. Alternatively, we will call them ground and excited state, respectively. These are the eigenstates of the system Hamiltonian \hat{H}_q given by,

$$\hat{H}_0 = \frac{\hbar\omega_0}{2} \hat{\sigma}_z \quad (2.9)$$

¹Here, we used the Josephson voltage-phase relationship, $\dot{\varphi} = (2e/\hbar)V$ and one of the Maxwell equations, $\dot{\Phi} = V$.

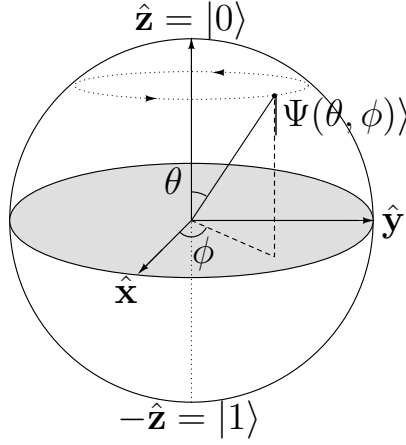


Figure 2.2: A representation of the qubit state $|\Psi(\theta, \phi)\rangle$ in the Bloch sphere is depicted. Any qubit state can be mapped on the surface of the Bloch sphere with two angles θ and ϕ . In the Bloch sphere, the north and south pole represent the ground and excited state and thus θ is undefined. The state on the equator corresponds to a 50/50 superposition state, $1/\sqrt{2}(|0\rangle + e^{i\phi}|1\rangle)$.

,where $\hat{\sigma}_z$ is one of the Pauli matrices, and ω_q the qubit transition frequency. A general qubit state can be written in the superposition of $|0\rangle$ and $|1\rangle$: $|\Psi(0)\rangle = \alpha|0\rangle + \beta|1\rangle$, where $|\alpha|^2 + |\beta|^2 = 1$ for the normalization of $|\Psi(t)\rangle$. The time evolution of the state by Schrödinger equation can be obtained by applying a unitary operator $\hat{U} = e^{-i\hat{H}_0 t/\hbar}$ to $|\Psi(0)\rangle$.

$$|\Psi(t)\rangle = \hat{U}|\Psi(0)\rangle = e^{-i\hat{H}_0 t/\hbar}|\Psi(0)\rangle \quad (2.10)$$

$$= \alpha e^{-iE_0 t/\hbar}|0\rangle + \beta e^{-iE_1 t/\hbar}|1\rangle \quad (2.11)$$

$$= e^{-iE_0 t/\hbar}[\alpha|0\rangle + \beta e^{-i(E_1 - E_0)t/\hbar}|1\rangle] \quad (2.12)$$

Without losing generality, the exponential factor $e^{-iE_0 t/\hbar}$ can be dropped off in Eq. (2.12), and the final qubit state is given by

$$|\Psi(t)\rangle = \alpha|0\rangle + \beta e^{-i\omega_0 t}|1\rangle \quad (2.13)$$

One can see the relative phase factor ($e^{-i\omega_0 t}$) rotates through 2π as time evolves. This phase rotation can be viewed equivalent to Larmor frequency of a spin 1/2 under a constant magnetic field.

The dynamics of the qubit state can be conveniently represented as one point on so-called Bloch sphere as shown in Fig. 2.2. The Bloch sphere is commonly used to visualize the state of the two-level system by mapping the state on the surface of the Bloch sphere with two angles θ and ϕ . Any qubit state on the Bloch

sphere is expressed in the following way:

$$|\Psi(t)\rangle = \cos(\theta/2)|0\rangle + e^{i\phi} \sin(\theta/2)|1\rangle \quad (2.14)$$

In the Bloch sphere, the north pole corresponds to $|0\rangle$ state, the south pole to $|1\rangle$, and the equator to an equal superposition state $1/\sqrt{2}(|0\rangle + \exp^{i\phi}|1\rangle)$. Generally, the time evolution of the qubit state appears as a trajectory on the Bloch sphere. The time-evolution of the state in Eq. (2.13) corresponds to the rotation of a unit vector at an angular frequency ω_0 around the $\hat{\mathbf{z}}$ axis (The trajectory is shown as a dotted line in Fig. 2.2).

Often it is more convenient to deal with dynamics of a system in a different reference frame, where a system dynamics can be simplified—stationary. If a precessing unit vector is seen on a rotating frame that rotates at the same precession frequency as the vector, the unit vector would appear stationary. The transformation of quantum mechanical description to a rotating frame can be done as described in Appendix E. Accordingly, the qubit Hamiltonian \hat{H} in the lab frame can be transformed to a new Hamiltonian \hat{H}_R in a rotating frame by

$$\hat{H}_R = \hat{U}^\dagger \hat{H} \hat{U} - \hat{A}, \quad (2.15)$$

where $\hat{U} = e^{-i\hat{A}t/\hbar}$ and $\hat{A} = \hbar\omega\hat{\sigma}_z/2$. Therefore, the Hamiltonian in the rotating frame becomes

$$\hat{H}_R = \frac{\hbar(\omega_0 - \omega)}{2} \hat{\sigma}_z \quad (2.16)$$

If a rotating frame is chosen for $\omega = \omega_0$, the Hamiltonian \hat{H}_R becomes zero and thus the state doesn't evolve. This can be seen in the following way: $|\Psi_R(t)\rangle = \hat{U}^\dagger |\Psi(t)\rangle = \hat{U}^\dagger \hat{H}_0 |\Psi(0)\rangle = |\Psi(0)\rangle$, i.e., $|\Psi_R(t)\rangle$ is time-independent.

In order to make use of the qubit, one should be able to manipulate the qubit state in a controllable way—qubit rotation. The qubit state can be controlled normally by applying classical harmonic electromagnetic field. The oscillation field acts as a perturbing Hamiltonian \hat{V} and the full Hamiltonian becomes $\hat{H} = \hat{H}_0 + \hat{V}$ and can be given by

$$\hat{H} = \frac{\hbar\omega_0}{2} \hat{\sigma}_z + \hbar\Omega \cos(\omega t + \varphi) \hat{\sigma}_x, \quad (2.17)$$

where $\hbar\Omega = \langle 1|\hat{\mathbf{d}} \cdot \mathbf{E}_0|0\rangle$, $\hat{\mathbf{d}}$ the dipole moment operator, \mathbf{E}_0 the amplitude of harmonics radiation $\mathbf{E} = \mathbf{E}_0 \cos(\omega t)$.

As shown in the case of the unperturbed case above, it is convenient to describe qubit rotation in a rotating frame rotating with the same angular frequency ω as the classical field. To calculate the Hamiltonian \hat{H}_R

in the rotating frame, we set $\hat{A} = (\hbar\omega/2)\hat{\sigma}_z$. Then Hamiltonian \hat{H}_R can be written by

$$\hat{H}_R = \hat{U}^\dagger \hat{H} \hat{U} - \hat{A} \quad (2.18)$$

$$= e^{-i\frac{\omega t}{2}\hat{\sigma}_z} \left(\frac{\hbar\omega_0}{2}\hat{\sigma}_z + \hbar\Omega \cos(\omega t + \varphi)\hat{\sigma}_x \right) e^{i\frac{\omega t}{2}\hat{\sigma}_z} - \frac{\hbar\omega}{2}\hat{\sigma}_z \quad (2.19)$$

$$= [\hbar\Omega \cos(\omega t + \varphi)] \left[e^{-i\frac{\omega t}{2}\hat{\sigma}_z} \hat{\sigma}_x e^{i\frac{\omega t}{2}\hat{\sigma}_z} \right] + \frac{\hbar(\omega_0 - \omega)}{2}\hat{\sigma}_z \quad (2.20)$$

$$= [\hbar\Omega \cos(\omega t + \varphi)] [\cos(\omega t)\hat{\sigma}_x + \sin(\omega t)\hat{\sigma}_y] + \frac{\hbar\Delta\omega}{2}\hat{\sigma}_z \quad (2.21)$$

$$\approx \frac{\hbar\Omega}{2} (\cos\varphi\hat{\sigma}_x - \sin\varphi\hat{\sigma}_y) + \frac{\hbar\Delta\omega}{2}\hat{\sigma}_z \quad (2.22)$$

$$= \left(\frac{\hbar\Omega}{2} \cos\varphi, \frac{\hbar\Omega}{2} \sin\varphi, \frac{\hbar\Delta\omega}{2} \right) \cdot (\hat{\sigma}_x, -\hat{\sigma}_y, \hat{\sigma}_z) \quad (2.23)$$

$$= \frac{\hbar\vec{\omega}}{2} \cdot \hat{\sigma}, \quad (2.24)$$

where $\vec{\omega} = (\Omega \cos\varphi, -\Omega \sin\varphi, \Delta\omega)$ and $\hat{\sigma} = (\hat{\sigma}_x, \hat{\sigma}_y, \hat{\sigma}_z)$. In deriving the Eq. (2.22), one of trigonometric identities is used: $\cos(\omega t + \varphi) \cos(\omega t) = (1/2)[\cos(2\omega t + \varphi) + \cos\varphi]$. Also, the $\cos(2\omega t + \varphi)$ term which oscillates rapidly is neglected and this approximation is called Rotating wave approximation (RMA).

Now the time-evolution of the state in the rotating frame is given by $|\Psi_R(t)\rangle = e^{-i\hat{H}_R t/\hbar} |\Psi_R(0)\rangle = e^{-i(\vec{\omega}t/2) \cdot \hat{\sigma}} |\Psi_R(0)\rangle$. In fact, the operator $e^{-i(\vec{\omega}t/2) \cdot \hat{\sigma}}$ is a rotation operator of the form $R_{\mathbf{n}}(\delta) = e^{-i\delta \mathbf{n} \cdot \hat{\sigma}}$, where \mathbf{n} is a unit vector. What this implies is that the rotation axis in the Bloch sphere can be controlled by changing the phase shift φ of the classical harmonic radiation. When applied to the qubit state, $R_{\mathbf{n}}(\delta)$ makes the Bloch vector rotate around the \mathbf{n} axis in right hand rule. Therefore, $e^{-i(\vec{\omega}t/2) \cdot \hat{\sigma}}$ makes $|\Psi_R(0)\rangle$ rotate around the axis \mathbf{n} by the angle ωt on the Bloch sphere.

In the resonant case, i.e., $\omega_0 = \omega$, the initial state $|\Psi_R(0)\rangle$ of the qubit is rotated around the axis $\mathbf{n} = (\cos\varphi, -\sin\varphi, 0)$ by the angle $\theta = \Omega t$ during time t in the Bloch sphere. For example, for $\varphi = 0$, the rotation axis becomes just x-axis.

2.1.3 Rabi oscillations

In this section, we will describe quantum oscillation phenomena of a two-level system—Rabi oscillation. When a superconducting qubit is radiated continuously by weak harmonic classical radiation, the probability of both the ground and excited state oscillates as a function time, which is normally called Rabi oscillation, named after a physicist Rabi [41]. This property can be used to prepare a quantum state, typically in pure excited state ($|\Phi\rangle = |1\rangle$) or a 50/50 superposition state ($|\Phi\rangle = 1/\sqrt{2}(|0\rangle + e^{i\varphi}|1\rangle)$). To describe Rabi oscillation more quantitatively, let's consider a two-level system interacting with weak classical microwave. The two level system has the ground ($|0\rangle$) and excited ($|1\rangle$) state, and the transition frequency $\omega_0 =$

$(E_1 - E_0)/\hbar$. Now we apply harmonic radiation $\mathbf{E}(t) = \mathbf{E}_0 \cos(\omega t)$. Then the total Hamiltonian can be written as

$$\hat{H} = \frac{\hbar\omega_0}{2}\sigma_z - \hbar\Omega_0 \cos(\omega t)\sigma_x, \quad (2.25)$$

where $\hbar\Omega_0 = \langle 1|\hat{\mathbf{d}} \cdot \mathbf{E}_0|0\rangle/\hbar$, $\hat{\mathbf{d}}$ is the dipole moment operator, and \mathbf{E}_0 is the amplitude of the harmonic radiation. We write a wavefunction as

$$|\Phi(t)\rangle = C_0(t)e^{-iE_0t/\hbar}|0\rangle + C_1(t)e^{-iE_1t/\hbar}|1\rangle, \quad (2.26)$$

where $E_0 = -\hbar\omega_0/2$ and $E_1 = \hbar\omega_0/2$. By plugging the wavefunction to the Schrödinger equation, we obtain two coupled equations

$$\dot{C}_0 = i\Omega_0 \cos(\omega t)e^{-i\omega_0 t}C_1, \quad (2.27)$$

$$\dot{C}_1 = i\Omega_0 \cos(\omega t)e^{i\omega_0 t}C_0. \quad (2.28)$$

Using $\cos(\omega t) = 1/2(e^{i\omega t} + e^{-i\omega t})$, we have two terms, slowly rotating term $e^{\pm i(\omega - \omega_0)t}$ and quickly rotating term $e^{\pm i(\omega + \omega_0)t}$. Since the wavefunction $|\Phi(t)\rangle$ evolves much slowly than ω_0 , we can neglect the quickly rotating term by approximation, which is called Rotating Wave Approximation (RWA). The RWA leads to

$$\dot{C}_0 = \frac{i}{2}\Omega_0 e^{i(\omega - \omega_0)t}C_1, \quad (2.29)$$

$$\dot{C}_1 = \frac{i}{2}\Omega_0 e^{-i(\omega - \omega_0)t}C_0. \quad (2.30)$$

$$(2.31)$$

By solving for $C_1(t)$, we have a second-order differential equation

$$\ddot{C}_1 + i(\omega - \omega_0)\dot{C}_1 + \frac{\Omega_0^2}{4}C_1 = 0. \quad (2.32)$$

The general solution of the differential equation (Eq. (2.32)) is $C_1(t) = C_+e^{i\lambda_+t} + C_-e^{i\lambda_-t}$, where $\lambda_{\pm} = 1/2(\Delta \pm \sqrt{\Delta^2 + \Omega_0^2})$ and $\Delta = \omega_0 - \omega_1$ is the detuning. Using the initial condition that $C_0(0) = 1$ and $C_1(0) = 0$, i.e., qubit in the ground state, we arrive at the final solution

$$C_1(t) = e^{i\Delta t/2} \left[\frac{\Omega_0}{\Omega_R} \sin(\Omega_R t/2) \right], \quad (2.33)$$

$$C_0(t) = e^{-i\Delta t/2} \left[\cos(\Omega_R t/2) + i \frac{\Delta}{\Omega_R} \sin(\Omega_R t/2) \right], \quad (2.34)$$

where Ω_R is called **Rabi frequency** and is expressed as follows:

$$\Omega_R = \sqrt{\Delta^2 + \Omega_0^2}. \quad (2.35)$$

Therefore, the wave function becomes

$$|\Phi(t)\rangle = \left[\cos(\Omega_R t/2) + i \frac{\Delta}{\Omega_R} \sin(\Omega_R t/2) \right] e^{-i(E_0 + \Delta)t/\hbar} |0\rangle + \left[\frac{\Omega_0}{\Omega_R} \sin(\Omega_R t/2) \right] e^{-i(E_1 - \Delta)t/\hbar} |1\rangle, \quad (2.36)$$

and for zero detuning $\Delta = 0$, the wave function is simplified to,

$$\begin{aligned} |\Phi(t)\rangle &= \cos(\Omega_0 t/2) e^{-iE_0 t/\hbar} |0\rangle + \sin(\Omega_0 t/2) e^{-iE_1 t/\hbar} |1\rangle \\ &= e^{-E_0 t/\hbar} [\cos(\Omega_0 t/2) |0\rangle + \sin(\Omega_0 t/2) e^{-i\omega_{01} t} |1\rangle] \end{aligned} \quad (2.37)$$

Thus, the probabilities to find the qubit in the ground and excited state become

$$P_1(t) = |C_1(t)|^2 \quad (2.38)$$

$$= \left(\frac{\Omega_0}{\Omega_R} \right)^2 \sin^2(\Omega_R t/2) \quad (2.39)$$

$$= \left(\frac{\Omega_0}{\Omega_R} \right)^2 \frac{1}{2} [1 - \cos(\Omega_R t)] \quad (2.40)$$

$$P_0(t) = |C_0(t)|^2 \quad (2.41)$$

$$= \cos^2(\Omega_R t/2) + \left(\frac{\Delta}{\Omega_R} \right)^2 \sin^2(\Omega_R t/2), \quad (2.42)$$

It is important to understand the meaning of the expressions derived, especially, the Rabi frequency Ω_R and the probability $P_1(t)$. First, in Eq.(2.39), we can see that the probability $P_1(t)$ to find the qubit in the excited state oscillates under the harmonic radiation with the Rabi frequency Ω_R . Second, the Rabi frequency is a function of both the detuning Δ and coupling energy $\hbar\Omega_0$, and the latter is proportional to the amplitude of the harmonic radiation; therefore, the Rabi frequency can depend on both the frequency (via Δ) and amplitude (via Ω_0) of applied harmonic radiation. However, when the detuning is zero, the Rabi frequency is solely dependent on the amplitude of harmonic radiation.

To do more quantitative explanation, let's consider two cases: zero detuning $\Delta = 0$ and non-zero detuning $\Delta \neq 0$. In the case of zero detuning $\omega = \omega_0$ when the harmonic radiation and qubit are in resonance, the Rabi frequency reduces to $\Omega_R = \Omega_0$. Also, $P_0(t) = \cos^2(\Omega_0 t)$ and $P_1(t) = \sin^2(\Omega_0 t)$. Since $\Omega_0 \propto |\mathbf{E}_0|$, the Rabi frequency becomes proportional to the amplitude of the harmonic radiation. In practice, the amplitude

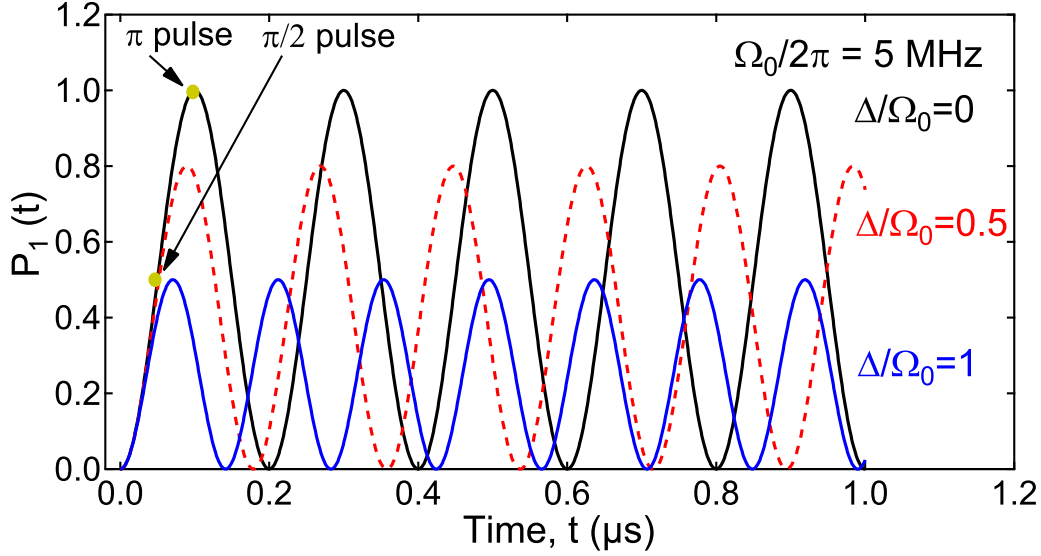


Figure 2.3: The calculated probability $P_1(t)$ versus time t is depicted for three different ratios of detuning to zero-detuning Rabi frequency: $\Delta/\Omega_0 = 0$ (black solid), $\Delta/\Omega_0 = 0.5$ (red dashed), and $\Delta/\Omega_0 = 1$ (blue solid). For all three plots, $\Omega_0/2\pi = 5$ MHz is used. Also, two positions corresponding to π and $\pi/2$ pulses are indicated by dark yellow dots.

of applied microwave signal is adjusted to set a desired Rabi frequency. On the other hand, the probability $P_1(t)$ varies sinusoidally from zero to one with the Rabi frequency Ω_0^2 . This behavior allows us to prepare the qubit initially in the pure excited state $|\Phi(t)\rangle = |1\rangle$ or a superposition state $|\Phi(t)\rangle = (1/2)(|0\rangle + e^{i\phi}|1\rangle)$, by simply applying a certain length of microwave pulse. Conventionally, the shortest microwave pulse which brings the qubit from ground to excited state is called " π pulse". The length of the π pulse, t_π can be found from $P_1(t_\pi) = 1$, i.e. $\Omega_0 t_\pi = \pi$ (this is why it's called π pulse), leaving $t_\pi = \pi/\Omega_0$. Similarly, the shortest microwave pulse that creates a 50/50 superposition state ($|\Phi(t)\rangle = 1/2(|0\rangle + e^{i\phi}|1\rangle)$) when the qubit is initially in the ground state, is called " $\pi/2$ pulse", because of the condition $\Omega_0 t_{\pi/2} = \pi/2$ for $P_1(t_{\pi/2}) = 1/2$.

The evolution of qubit state during the Rabi oscillation can be considered in Bloch sphere easily in Fig. 2.4. Initially, the qubit is in the ground state $|0\rangle$ and represented as a vector point to the north pole. As harmonic radiation is applied, the vector rotates around x -axis at an angular velocity of Ω_0 . Therefore, the azimuthal angle of the vector after time t will be $\Delta\varphi = \Omega_0 t$.

Now we turn to non-zero detuning case where $\Delta \neq 0$. We immediately see from $\Omega_R = \sqrt{\Delta^2 + \Omega_0^2}$ that the Rabi frequency is greater than that of zero-detuning case, $\Omega_R > \Omega_0$, and it is not proportional to Ω_0 and amplitude of harmonic radiation. The non-zero detuning case has some practical implication rather

²Note that $P_1(t) = \sin^2(\Omega_0 t) = [1 - \cos(\Omega_0 t)]/2$. So the frequency of oscillation is Ω_0 , not $\Omega_0/2$.

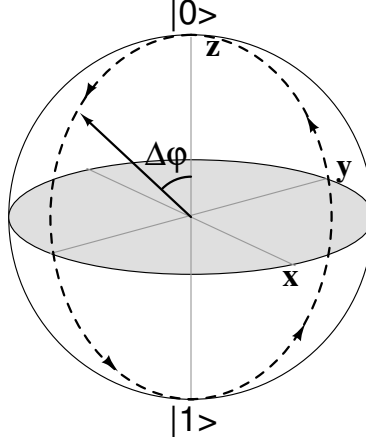


Figure 2.4: The representation of the trajectory for the qubit state to take during Rabi oscillation on the Bloch sphere. The Bloch vector rotates around x-axis by $\Delta\varphi = \Omega_0 t$, where Ω_0 is Rabi frequency and t is time duration of applied harmonic radiation.

than physical implication. In conventional qubit measurement, one finds π pulse and $\pi/2$ pulse associated with zero-detuned Rabi frequency Ω_0 . When one has to apply a slightly detuned microwave—as needed in Ramsey fringe measurement in next section, if Δ is much larger than Ω_0 ($\Delta \gg \Omega_0$), then since the Rabi frequency $\Omega_R \approx \Delta \gg \Omega_0$ becomes too far off from Ω_0 , the π and $\pi/2$ pulses found previously for Ω_0 would not serve as such pulses. Therefore, the non-zero detuning case should be taken into account when choosing Rabi frequency in the measurement. Another aspect different from the zero-detuning case is that the $P_1(t)$ does not oscillate in the full range of 0 to 1 as shown in Fig. 2.3. This means that if the frequency of the harmonic radiation is far detuned from the qubit transition frequency, we can not drive the qubit to the pure excited state.

2.1.4 Relaxation time, Ramsey fringe, and spin echo measurement

The dynamical behavior of a qubit is normally characterized by two times T_1 and T_2 associated with the duration of a qubit state. T_1 —called "relaxation time"—is the time required for a qubit to relax from the first excited state back to the ground state. This process is inherently accompanied by energy loss. This loss can be either radiative (energy loss through photons) or non-radiative (energy loss through phonon or heat), depending on the nature of loss mechanism. Meanwhile, T_2 called "dephasing time" is the time over which the (relative) phase relation between the ground and excited states is lost or randomized. Both relaxation and dephasing are described by the weak interaction of a qubit with environmental quantum noise. The relaxation process results from energy fluctuation at the qubit transition levels [42]. However, the dephasing

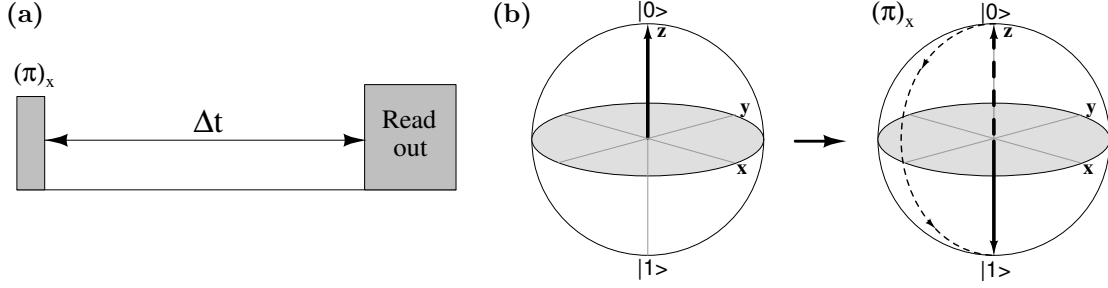


Figure 2.5: Schematic of pulse sequence and Bloch sphere representations for relaxation time measurement. (a) Microwave pulse sequence for relaxation time measurement. Δt is the time interval between π pulse and readout pulse. (b) Bloch sphere representation of a qubit state. The qubit is initialized in the ground state, followed by π pulse applied. The pure excited state $|1\rangle$ is reached.

rate—inverse of the dephasing time—arises from two channels:

$$\frac{1}{T_2} = \frac{1}{2T_1} + \frac{1}{T_\varphi}, \quad (2.43)$$

where T_φ is called "pure dephasing rate". The first channel by which dephasing occurs is the relaxation process. On the other hand, the second channel is pure dephasing process, which is attributed to low-frequency fluctuation through exchange of infinitesimal energy with environment.

Now we will describe how to measure those two time scales T_1 and T_2 . These time-domain measurements require to use a series of microwave pulses in the right timing. The measurement of relaxation time is typically carried out first by applying a π pulse to drive a qubit to the first excited state—explained in Sec. 2.1.3. Then after time interval Δt , the state of qubit is read out. Such measurements should be repeated many times ($10^5 - 10^6$) to obtain the probability $P_1(t)$ versus time t by ensemble average. The relaxation measurement shows how fast the probability $P_1(t)$ exponentially decays as a function of time, and the time constant by fitting data with e^{-t/T_1} can be extracted. A schematic of a typical pulse sequence used for relaxation time measurement is shown in Fig. 2.5(a). Also, it is useful to use Bloch sphere to visualize the trajectory of qubit state during time-domain measurements as shown in Fig. 2.5(b). For relaxation time measurement, first the qubit is initialized in the ground state, indicated by the arrow pointing the north pole in Fig. 2.5(b) (1st Bloch sphere). Then a π pulse is applied to bring the arrow down to the south pole by rotating it around the x -axis (counterclockwise when looked down), leading to the excited state $|1\rangle$.

Let's turn to T_2 measurement case. When one measures dephasing time, it is important to distinguish T_2 and T_2^* . T_2 is the intrinsic decoherence time of a single qubit. However, T_2^* is experimental decoherence time from ensemble measurement. In practice, a qubit needs to be measured repeatedly to acquire precise data, thus comprising ensemble measurement. Although each measurement is normally identical, slow fluctuations

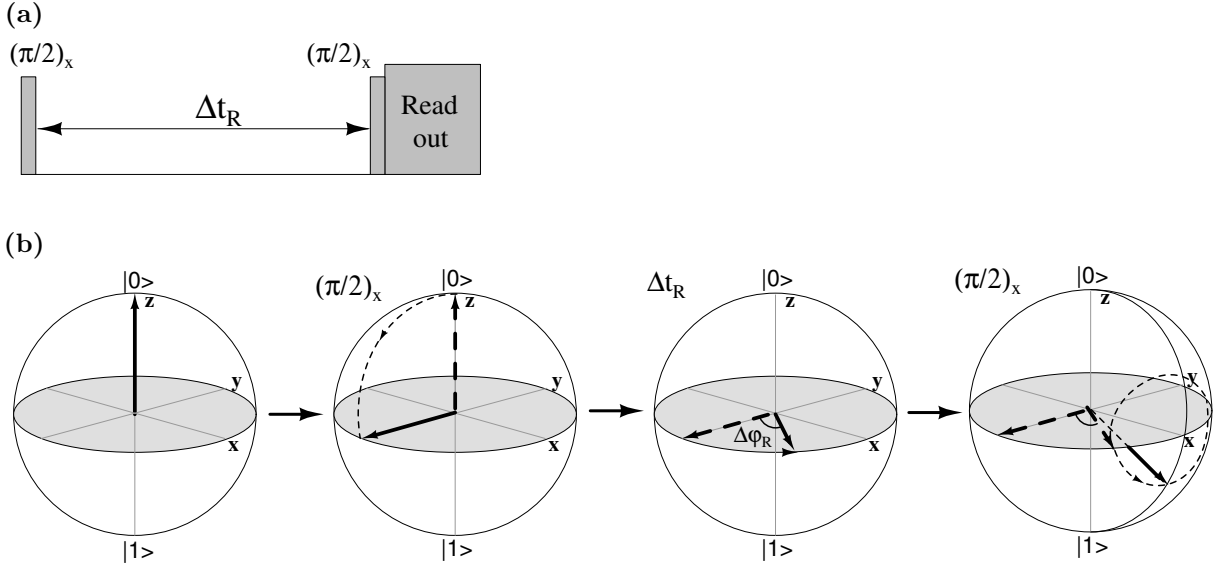


Figure 2.6: Schematic of pulse sequence and Bloch sphere representation for Ramsey fringe measurement. (a) Microwave pulse sequence for Ramsey fringe measurement. Δt_R is the Ramsey separation time between two $\pi/2$ pulses. (b) Bloch sphere representation of Ramsey fringe measurement. A qubit is initialized in the ground state first and $\pi/2$ pulse follows creating a 50/50 superposition state. The state evolves during Δt_R , and after that $\pi/2$ pulse is applied again. Immediately, the qubit state is read out.

of environmental noise on the time scale of each single run give rise to additional dephasing rate. Thus, T_2^* time is shorter than T_2 . To measure T_2^* , one performs Ramsey fringe measurement conventionally [43]. Ramsey fringe measurement is carried out by applying two $\pi/2$ pulses, separated by a time Δt_R and reading out the state immediately right after the second $\pi/2$ pulse. This pulse sequence and corresponding Bloch vector representation are depicted in Fig. 2.6(a) and Fig. 2.6(b), respectively. For Ramsey measurement, first, the qubit is initialized in the ground state. Then a $\pi/2$ pulse is applied to create a 50/50 superposition state. In Bloch sphere, this process is represented as the vector rotating around x -axis by 90 degree and landing on the equator. After the $\pi/2$ pulse, the qubit is left unperturbed to evolve during Δt_R . The vector in Bloch sphere rotates around z -axis on the equator by $\Delta\phi_R$. This free evolution naturally occurs as described by time-dependant Schrödinger equation [see Eq. (2.12)]. After the free evolution, the second $\pi/2$ pulse is applied, which makes the state vector rotate by 90 degree around x -axis. Finally, the state is read out immediately by projecting the state on the z -axis.

T_2 can be measured by called "spin echo" or alternatively "Hahn spin echo" technique, borrowed from NMR (Nuclear Magnetic Resonance). The basic idea involved in this technique is to insert a so-called refocusing pulse (π pulse) in the middle of two $\pi/2$ pulses, so that the broadened state vector during free evolution can refocused after the refocusing pulse. The pulse sequence and Bloch representation are shown

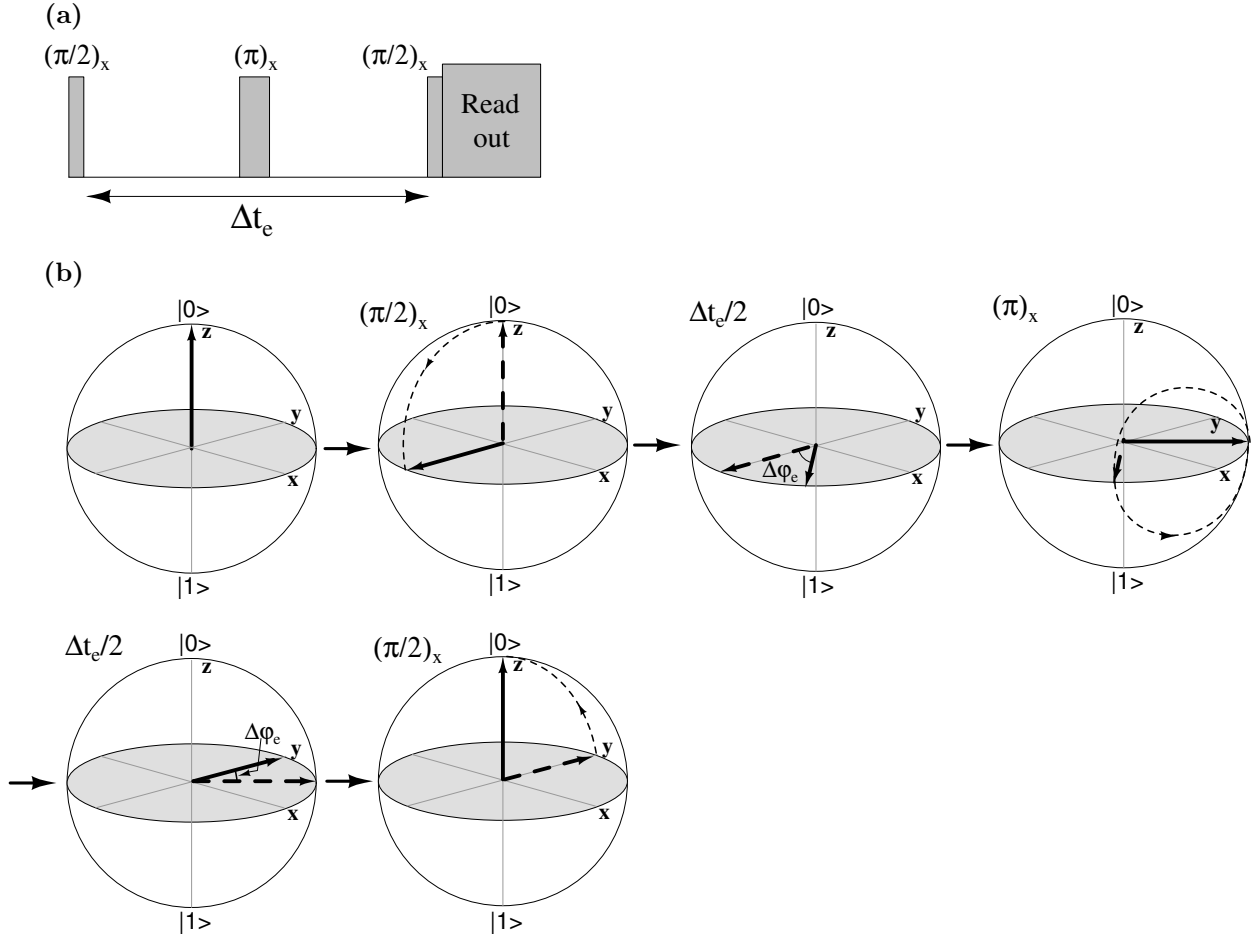


Figure 2.7: Schematic of pulse sequence and Bloch sphere representation for Hahn spin echo measurement. (a) Microwave pulse sequence for Hahn spin echo measurement. Δt_e is the spin echo separation time between two $\pi/2$ pulses. π pulse is inserted right in the middle of two $\pi/2$ pulses. (b) Bloch sphere representation of spin echo measurement. A qubit is initialized in the ground state first and $\pi/2$ pulse follows creating a 50/50 superposition state. The state evolves during $\Delta t_e/2$, and after that π pulse is applied. The state evolves again during $\Delta t_e/2$, followed by $\pi/2$ pulse applied. Immediately, the qubit state is read out.

in Fig. 2.7(a) and Fig. 2.7(b). For spin echo measurement, the qubit is initialized in the ground state first. Then a $\pi/2$ pulse is applied to create a 50/50 superposition, as represented as the state vector lying on the equator in Bloch sphere. The qubit free evolves during time interval $\Delta t_e/2$, and the state vector rotates by $\Delta\phi_e$. After the free evolution, a new π pulse is applied, which makes the state vector turns around x -axis by full 180 degree. The effect of this π pulse is to cancel out the broadening of the 50/50 superposition state during the next free evolution time $\Delta t_e/2$, i.e. refocusing the state. After the second free evolution, the second $\pi/2$ pulse is applied, which will bring the qubit almost back to the ground state. Finally, the qubit state is read out.

Before we close this section, it's worth to notice that when we represented the qubit state in Bloch sphere, the geometrical trajectory of the state was described in the rotating frame which rotates counterclockwise

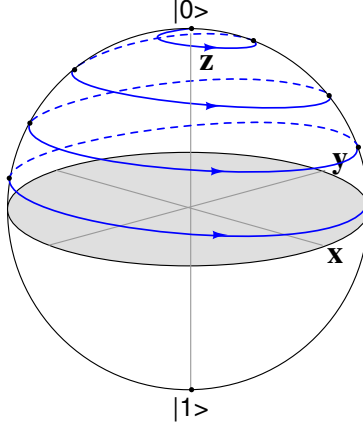


Figure 2.8: The trajectory of the qubit state on the Bloch sphere, initially in the ground state, is shown in the *lab* frame during $\pi/2$ pulse applied. The qubit evolves starting from the north pole $|0\rangle$ to somewhere on the equator.

with an angular frequency ω , i.e. applied microwave frequency. Therefore, for example, if the trajectory of the qubit evolution during $\pi/2$ pulse is seen in the lab frame, it takes a spiral path on the Bloch sphere as shown in Fig. 2.8

2.2 Transmon qubit

In this section, we will describe about transmon qubits. A new type of superconducting qubit was proposed theoretically and demonstrated experimentally by superconducting qubit groups in Schoelkopf group in 2007-2008. The new qubit is a transmission-line shunted plasma oscillation qubit, called *transmon*. The design of the transmon is closely related with the Cooper pair box (CPB) qubit or charge qubit. However, the transmon is operated at a totally different ratio of Josephson energy E_J to Coulomb energy E_C , i.e., E_J/E_C . This new operating condition enables one to improve dephasing time dramatically by suppressing charge noise, which was known to be a main source of dephasing of the charge qubit. The main idea behind the transmon is that as the ratio E_J/E_C increases, the charge dispersion decreases exponentially, however, the anharmonicity decreases as a weak power law. Consequently, one can achieve a reduction of charge sensitivity to charge noise relative to the charge qubit, while the qubit is anharmonic enough to maintain fast qubit control capability.

In terms of the design, the transmon is the Cooper pair box (CPB) shunted by a large shunting capacitor as shown in Fig. 2.9. The \times symbol represents a Josephson junction (JJ) with a critical current I_C . The JJ normally has a junction capacitance C_J , which depends on the junction size and thickness of insulation

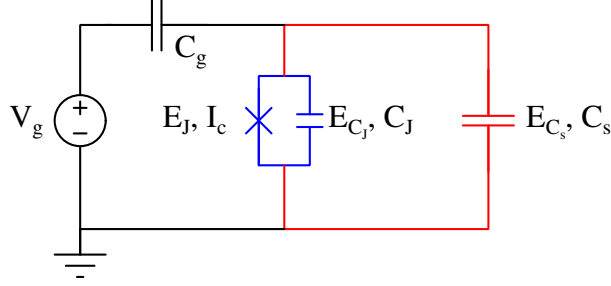


Figure 2.9: Effective circuit representation of transmon without coupling to readout circuit. The \times symbol is a Josephson junction (JJ) with a critical current of I_c and junction capacitance C_J . $E_J = \hbar I_c / 2e$ and $E_{C_J} = e^2 / 2C_J$ are the Josephson energy and charging energy of the JJ. C_s denotes a shunt capacitance and the charge energy associated with C_s is E_{C_s} . The gate voltage V_g is applied via the gate capacitance C_g . The JJ and both capacitors form an anharmonic oscillator, where the JJ acts as a nonlinear inductor that provides anharmonicity to the transmon system.

layer³. The capacitance C_s is a shunt capacitance, which is typically much larger than $C_J \ll C_s$. The capacitance C_g is a gate capacitance. Therefore, the total capacitance $C_\Sigma = C_J + C_s + C_g$ is dominated by C_s in choosing device parameters.

The Hamiltonian of the transmon—same as that of the CPB can be written as

$$\hat{H} = 4E_{C_\Sigma}(\hat{N} - N_g)^2 - E_J \cos \hat{\varphi}, \quad (2.44)$$

where $E_{C_\Sigma} = e^2 / (2C_\Sigma)$ is the total charging energy of a single electron, $E_J = \hbar I_c / (2e)$ is the Josephson energy set only by the critical current of the JJ, and $N_g = C_g V_g / e$ is the (induced) gate charge which is controlled by the gate voltage V_g . The number operator \hat{N} (number of Cooper pair) and phase operator $\hat{\varphi}$ (phase across the JJ) are canonical conjugate quantities, satisfying a commutation relation $[\hat{\varphi}, \hat{N}] = i$. The transmon is operated in the regime $E_J \gg E_C$, and this condition can be met by making the charging energy small compared to the Josephson energy. One way of doing it is to add a shunt capacitance.

The transmon Hamiltonian can be solved analytically in phase basis to obtain energy eigenvalues and corresponding eigenstates (see Appendix B in Ref [25]). Alternatively, the Hamiltonian can be numerically solved in charge basis. When solved analytically in phase basis, the eigenvalues $E_m(n_g)$ are given by

$$E_m(n_g) = E_C a_{2[n_g + k(m, n_g)]}(-E_J / (2E_C)), \quad (2.45)$$

³We only deal with a Josephson junction made of an aluminium tunnel junction Al/Al₂O₃/Al in a planar geometry.

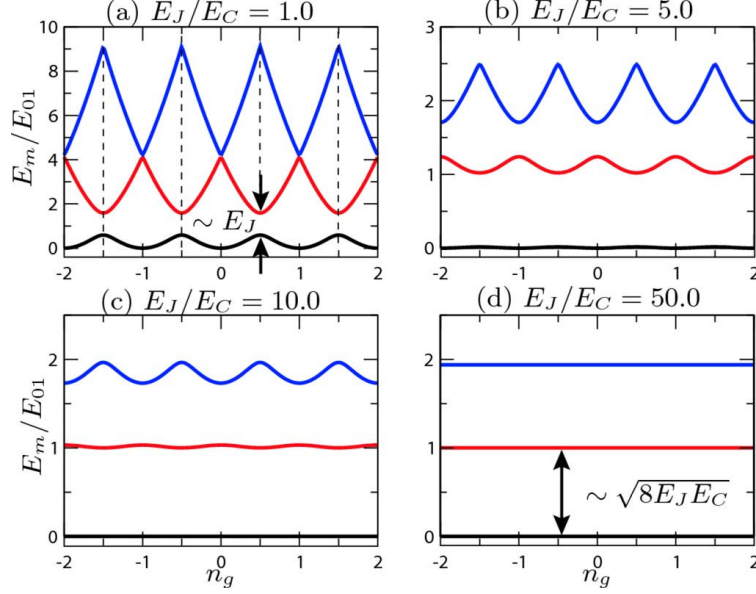


Figure 2.10: Eigenvalues of the Hamiltonian ((2.44)) are plotted as a function of the gate charge n_g for different ratios of $E_J/E_C = 1, 5, 10$, and 50 . E_{01} is the energy difference between E_0 and E_1 , evaluated at $n_g = 1/2$ (half-integer). The graphs were taken from Ref. [25].

where $a_\nu(q)$ is Mathieu's characteristic value, and $k(m, n_g)$ is

$$k(m, n_g) = \sum_{l=\pm 1} [\text{int}(2n_g + l/2) \bmod 2] \cdot \{\text{int}(n_g) + l(-1)^m[(m+1) \text{div } 2]\}, \quad (2.46)$$

where $\text{int}(x)$ is the integer closest to x , mod is a modulus, and $x \text{ div } y$ is the quotient of x/y .

The eigenvalues of the transmon versus the gate charge n_g , calculated for four different ratios of E_J/E_C , are shown in Fig. 2.10. The eigenvalues as a function of the gate charge n_g , $E_m(n_g)$, are plotted for different ratios of E_J/E_C . The $E_m(n_g)$ is normalized to E_{01} , which is the energy difference between the ground (E_0) and excited (E_1) energy levels, evaluated at the $n_g = 1/2$. We can see that as the ratio E_J/E_C increases, the energy levels become flatter, and in the case of $E_J/E_C = 50$, the energy levels are almost flat, leading to the qubit much more insensitive to charge noise than the charge qubit. Note that the qubit transition level E_{01} can be approximated to $\sim \sqrt{8E_JE_C}$ in the transmon case.

Now we will see how charge dispersion changes with E_J/E_C . The charge dispersion ϵ_m is defined to the difference between the maximum and minimum eigenvalues of the m -th eigenstate $E_m(n_g)$. The approximate charge dispersion can be obtained from Eq. (2.45) to be (asymptotics of the Mathieu's characteristic value $a_\nu(q)$ is considered in the limit of large Josephson energy)

$$\epsilon_m \simeq (-1)^m E_C \frac{2^{4m+5}}{m!} \left(\frac{E_J}{2E_C} \right)^{\frac{m}{2} + \frac{3}{4}} e^{-\sqrt{8E_JE_C}}, \quad (2.47)$$

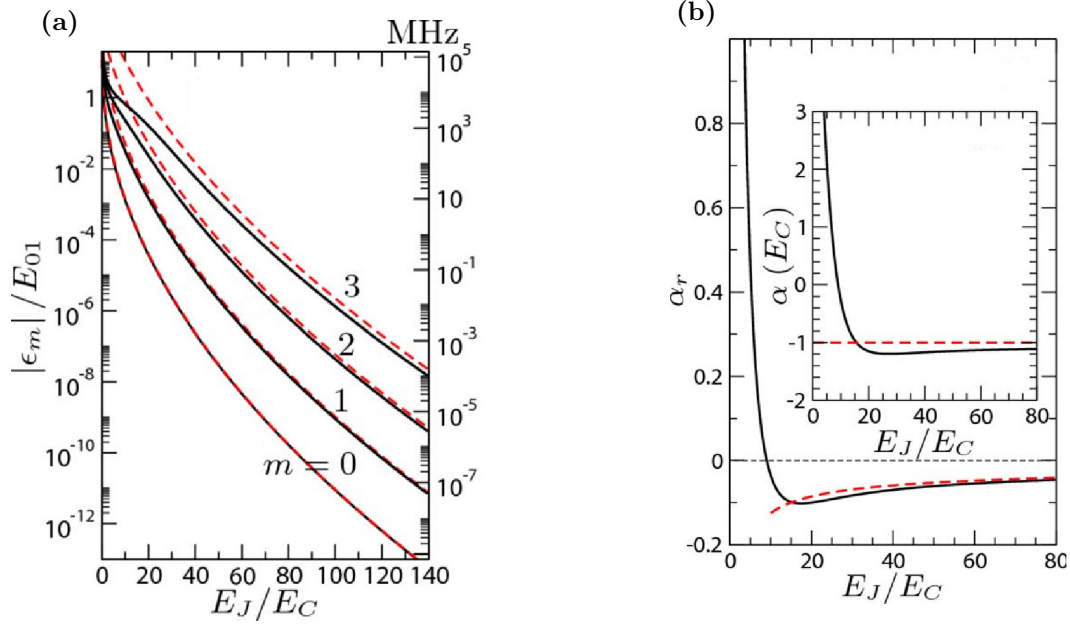


Figure 2.11: (a) The charge dispersion ϵ_m normalized to E_{01} versus E_J/E_C is depicted. (b) The relative anharmonicity α_r is shown as a function of E_J/E_C . For both (a) and (b), the solid lines are the solutions of the qubit Hamiltonian exactly solved. The red dashed lines shows the asymptotic results of the exactly solved solutions. The graphs were taken from Ref. [25].

which is valid for E_J/E_C . The charge dispersion ϵ_m normalized to E_{01} is plotted as a function of ratio E_J/E_C in Fig. 2.11(a). The key idea here is that the charge dispersion ϵ_m decreases *exponentially* as a function of E_J/E_C . This exponential reduction of the charge dispersion makes the transmon insensitive to the charge noise which causes high dephasing rate; the large charge dispersion means that qubit transition frequency is susceptible to fluctuations due to charge noise.

However, the increase of ratio E_J/E_C is not necessarily beneficial because it would mitigate anharmonicity of the qubit. It is anharmonicity that makes multi-level quantum system become a qubit, so that we can manipulate only the first and second energy level without another transitions with a reasonably short microwave pulses. In fact, the anharmonicity of the transmon turned out to decrease by a weak *power law* with the increase in E_J/E_C . Let us define a relative anharmonicity α_r as $\alpha_r = (E_{12} - E_{01})/E_{01}$. This quantifies how anharmonic three energy levels are, i.e., how different from an harmonic oscillator.

The asymptotic expression for the anharmonicity is

$$\alpha_r \simeq -1/\sqrt{8E_J/E_C}, \quad (2.48)$$

which indicates that the transmon anharmonicity decreases by a weak power law of $(E_J/E_C)^{-1/2}$, in contrary to the exponential decrease of the charge dispersion. Therefore, we can choose a certain range of E_J/E_C

with which the charge dispersion is negligibly small, but the anharmonicity is large enough to allow good control on the transmon. The anharmonicity α_r versus the ratio E_J/E_C is shown in Fig. 2.11(b). The solid line is the calculation based on the exactly solved eigenvalues, while the red dashed line is the asymptotic results of the exactly solved solution. It is seen that the relative anharmonicity decreases weakly with the increase of E_J/E_C .

2.3 3D circuit quantum electrodynamics (cQED)

In this section, we will describe the principle of circuit quantum electrodynamics (cQED) briefly.

2.3.1 circuit quantum electrodynamics

The circuit quantum electrodynamics (cQED) is an extension of conventional quantum electrodynamics (QED) to implementation of QED using a quantum circuit and 2D/3D resonator system. Also, it is often referred to as a new technique used to measure a superconducting qubit. The cQED developed in Schoelkopf group, has been extensively used in the study of various type of superconducting qubits, and its usage is even growing. The QED is the study of atom-light interaction and its behavior is completely described in the basis of quantum mechanics. Normally, to investigate the light-matter interaction in QEC, a number of photons are created and stored in a 3D Fabry-Perot (FP) optical cavity [44], and a series of atoms are sent to the cavity, passing through the cavity. In cQED, the FP cavity is replaced by a two-dimensional or three dimensional superconducting resonator⁴, and the atoms by superconducting qubits. For example, back in 2004, Wallraff et al. has demonstrated for the first time a single (microwave) photon can be strongly coupled to a superconducting qubit via the cQED [30]. They facilitated a 2D coplanar waveguide (CPW) superconducting resonator, which was coupled to a superconducting qubit (charge qubit) by strong electric dipole interaction. The coupling strength between the qubit and photons can be strong enough to observe many cycles of coherent quantum oscillations in the entangled qubit-photon states.

The cQED system can be described in terms of Jaynes-Cummings (JC) model in the same way as QED system. The JC model is a theoretical model used in quantum optics to explain the interaction of a two-level system with the quantized optical mode, i.e. photon. Suppose that there is a two-level system, e.g., qubit with the energy difference $\hbar\omega_q$, whose Hamiltonian is $H_q = \hbar\omega_q/2\sigma_z$, and a quantum harmonic oscillator with a Hamiltonian $H_r = \hbar\omega_r(a^\dagger a + 1/2)$. The interaction Hamiltonian H_{int} is given by $H_{\text{int}} = \hbar g(a^\dagger \sigma^- + \sigma^+ a)$.

⁴In the case of 3D resonators, not only superconductors, but normal metals like copper and brass, can be used to meet the need for the purpose of experiments

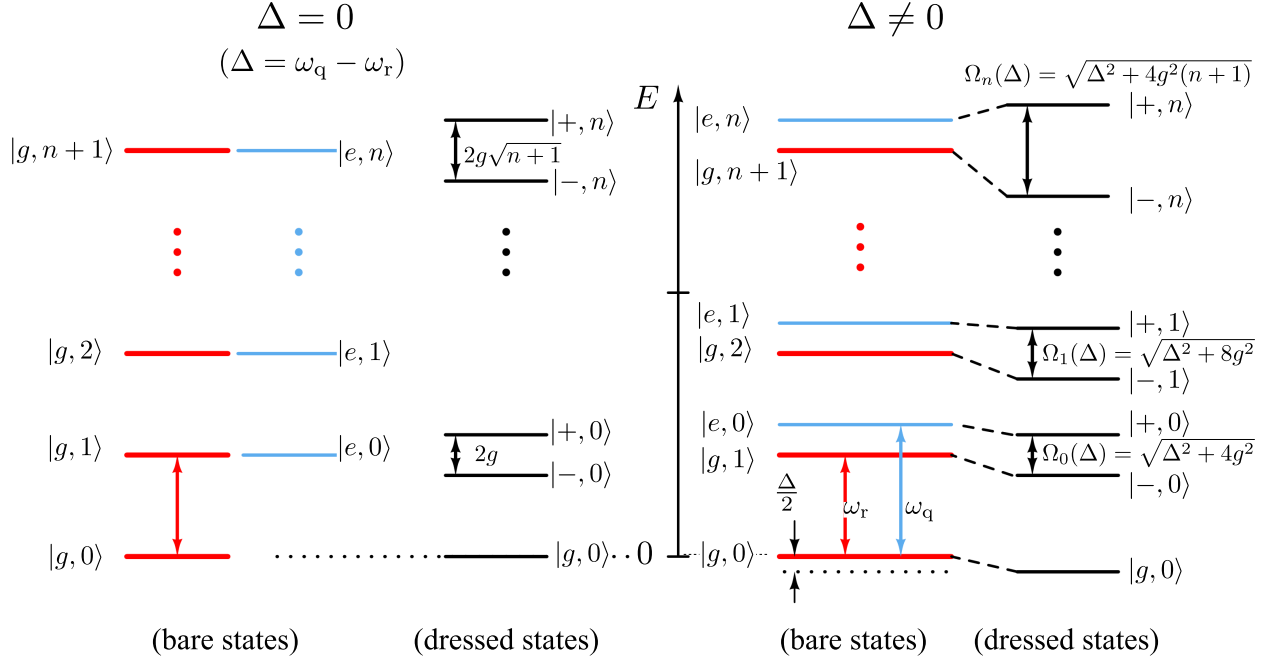


Figure 2.12: The energy spectrum diagrams of bare and dressed states of the Jaynes-Cummings Hamiltonian for zero-detuning and nonzero-detuning cases.

The Jaynes-Cummings Hamiltonian H_{JC} is given by [45]

$$\begin{aligned}
 H_{JC} &= H_r + H_q + H_{\text{int}} \\
 &= \hbar\omega_r \left(a^\dagger a + \frac{1}{2} \right) + \frac{\hbar\Omega}{2} \sigma_z + \hbar g (a^\dagger \sigma^- + \sigma^+ a),
 \end{aligned} \tag{2.49}$$

where σ_z is one of the Pauli operators (σ_x , σ_y , and σ_z), σ^+ and σ^- are the ladder operators defined by $\sigma^+ = \sigma_x + i\sigma_y$ and $\sigma^- = \sigma_x - i\sigma_y$, a and a^\dagger are annihilation and creation operators of a harmonic oscillator, and g is a coupling strength between the two-level system and photons. g is given by $g = E_0 d / \hbar$, where E_0 is the rms zero-point electric field and d is the transition dipole moment. The JC Hamiltonian can be exactly solved to get eigenvalue and eigenstate. In the case that there is no interaction between the qubit and photons, i.e. $H_{\text{int}}=0$, the eigenvalues are simply $E_{\pm,n} = \hbar\omega_r(n+1/2) \pm \hbar\Omega/2$, and the eigenstates are just the product states of the qubit and harmonic oscillator, $|g,n\rangle = |g\rangle|n\rangle$ and $|e,n+1\rangle = |e\rangle|n+1\rangle$ for $n \geq 0$. These states are called *bare states*. Now with the interaction turned on, the interaction Hamiltonian only allows the transitions between $|g,n+1\rangle$ and $|e,n\rangle$, thus we can consider a 2×2 subspace whose Hamiltonian matrix is given by

$$H^n = \begin{bmatrix} n\omega_r + \frac{1}{2}\hbar\omega_q & \hbar g\sqrt{n+1} \\ \hbar g\sqrt{n+1} & n\omega_r + \frac{1}{2}\hbar\omega_q \end{bmatrix}. \tag{2.50}$$

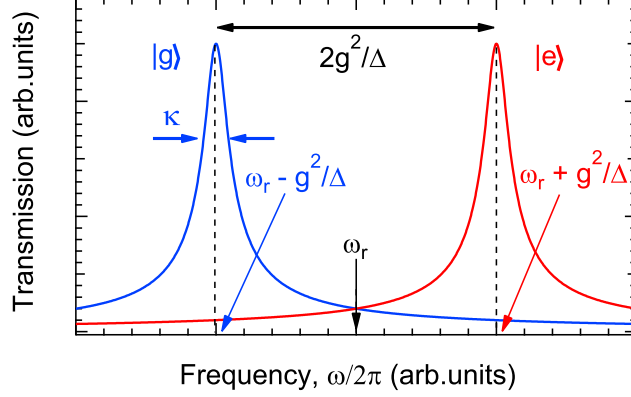


Figure 2.13: Transmission versus frequency for dispersive measurement. ω_r denotes the resonant frequency without the dispersive shift. Depending on the qubit state, the cavity frequency is pulled by $\pm g^2/\Delta$.

These eigenstates are called *dressed states*; the states are dressed (modified) with respect to the bare states.

The dressed states and their corresponding energies of the H_{JC} are given by

$$E_{g,0} = -\frac{\hbar\Delta}{2} \quad (2.51)$$

$$E_{\pm,n} = (n+1)\hbar\omega_r \pm \frac{\hbar}{2}\sqrt{\Delta^2 + \Omega_n^2(0)} \quad (2.52)$$

$$= (n+1)\hbar\omega_r \pm \frac{\hbar\Omega_n(\Delta)}{2} \quad (2.53)$$

$$|+,n\rangle = \cos\theta_n|e,n\rangle + \sin\theta_n|g,n+1\rangle \quad (2.54)$$

$$|-,n\rangle = -\sin\theta_n|e,n\rangle + \cos\theta_n|g,n+1\rangle, \quad (2.55)$$

where $\Delta = |\omega_q - \omega_r|$ is called the qubit-cavity detuning, $\Omega_n(0) = 2g\sqrt{n+1}$ is the n -photon Rabi frequency, $\Omega_n(\Delta) = \sqrt{\Delta^2 + \Omega_n^2(0)}$ is the n -photon Rabi frequency with nonzero detuning, and

$$\theta_n = \frac{1}{2} \tan^{-1} \left(\frac{\Omega_n(0)}{\Delta} \right) \quad (2.56)$$

$$\sin(\theta_n) = \frac{1}{\sqrt{2}} \sqrt{\frac{\Omega_n(\Delta) - \Delta}{\Omega_n(\Delta)}} \quad (2.57)$$

$$\cos(\theta_n) = \frac{1}{\sqrt{2}} \sqrt{\frac{\Omega_n(\Delta) + \Delta}{\Omega_n(\Delta)}} \quad (2.58)$$

The energy spectrum of the JC Hamiltonian is depicted in Fig. 2.12.

2.3.2 Dispersive measurement

The coupled system of a two-level and harmonic oscillator can be used to measure the qubit state. The hint for such idea can be seen when the effective Hamiltonian H_{eff} is obtained by the diagonalization of H_{JC} in the case of large detuning $g/\Delta \ll 1$ as follows.

$$H_{\text{eff}} = \hbar \left(\omega_r + \frac{g^2}{\Delta} \sigma_z \right) a^\dagger a + \frac{\hbar}{2} \left(\omega_q + \frac{g^2}{\Delta} \right) \sigma_z \quad (2.59)$$

$$= \hbar \omega_r a^\dagger a + \frac{\hbar}{2} \left(\omega_q + \frac{g^2}{\Delta} + \frac{2g^2}{\Delta} a a^\dagger \right) \sigma_z \quad (2.60)$$

There are two important points to make from the effective Hamiltonian. The first term implies that the frequency of the photon or cavity shifts by $\pm g^2/\Delta$, depending on the qubit state, i.e. state-dependant shift of resonant frequency ω_r , $\omega_r \rightarrow \omega_r \pm g^2/\Delta$. This property—the qubit pulls the cavity frequency—allows us to measure the qubit state by simply measuring the resonant frequency of cavity. In practice, the transmission of resonator is measured at a fixed frequency since the change of resonant frequency is reflected by the change of transmission [see Fig. 2.13]. On the other hand, as a backaction, the qubit transition frequency is also shifted, which is seen in the second expression in Eq. (2.59): $\omega_q \rightarrow \omega_q + g^2/(2\Delta) + g^2 n/\Delta$, where n is the number of photons in the cavity. The term $(g^2/\Delta)n$ indicates that the qubit frequency changes linearly as a function of the number of photons residing in the cavity, and this effect is called ac-Stark shift [46]. Especially, even a single photon can shift the qubit frequency by $(g^2/\Delta)/2\pi$ Hz. The last term $g^2/(2\Delta)$ is the Lamb shift [47].

The condition for the dispersive measurement is that the qubit-cavity detuning should be much larger than the coupling strength g . Also, the qubit measurement should be operated in a single photon regime to avoid dephasing caused by ac-Stark effect. Alternatively, a sequence of well-defined microwave pulses should be used to ensure that there exists always either readout photons (to measure transmission of cavity) or excitation photons (to control the qubit state).

2.3.3 Readout of transmon in dispersive regime

The transmon is usually measured in dispersive regime where $g_{01} \ll |\omega_{01} - \omega_c|$. However, since the transmon has higher levels with a relatively small anharmonicity, the dispersive shift is different from that of a two-level system. It is necessary to take into account higher level states in calculating the dispersive shift. Accordingly, the coupling strength should be generalized to g_{ij} between i th and j th states. g_{ij} is given by

$$\hbar g_{ij} = 2\beta e V_{\text{rms}}^0 \langle i | \hat{n} | j \rangle, \quad (2.61)$$

where $\beta = C_g/C_\Sigma$ is the ratio of gate capacitance to the total capacitance in the case of a transmon coupled to a 2D resonator, $V_{\text{rms}}^0 = \sqrt{\hbar\omega_r/(2C_r)}$ is the root-mean-square voltage of the resonator (C_r is the effective capacitance giving $\omega_r = 1/\sqrt{L_r C_r}$), \hat{n} is the Cooper-pair number operator, and the $\langle i|\hat{n}|j\rangle$ is the matrix element of \hat{n} with respect to the i th and j th eigenstates. In the case of the 3D cavity, the β and V_{rms}^0 will have to be replaced by appropriate equivalent parameters. It can be seen that the coupling strength g_{ij} asymptotically becomes as $E_J/E_C \rightarrow \infty$

$$g_{i+1,i} \propto \sqrt{\frac{i+1}{2}} \left(\frac{E_J}{E_C}\right)^{\frac{1}{4}} \quad (2.62)$$

$$g_{i+n,i} \rightarrow 0, \quad (2.63)$$

where $|n| = 2, 3, \dots$. First, we can see the only nearest neighbor coupling strength $g_{i\pm 1,i}$ provides significant contributions to coupling in high E_J/E_C regime. Second, we should note that the $g_{i\pm 1,i}$ grows as the power-law of the ratio E_J/E_C and the coupling between higher levels is stronger, i.e., $g_{12} > g_{01}$ as shown in Fig. 2.14(a).

Now when it comes to the dispersive shift, we consider in general the effective Hamiltonian of the transmon becomes [25]

$$H_{\text{eff}} = \frac{\hbar\omega'_{01}}{2}\sigma_z + (\hbar\omega'_r + \hbar\chi\sigma_z)a^\dagger a, \quad (2.64)$$

where $\omega' = \omega_{01} + \chi_{01}$ and $\omega'_r = \omega_r - \chi_{12}/2$. The effective dispersive shift χ is given by

$$\chi = \chi_{01} - \chi_{12}/2, \quad (2.65)$$

where χ_{ij} is the dispersive shift associated with i th and j th states and defined by

$$\chi_{ij} \equiv \frac{g_{ij}}{\omega_{ij} - \omega_r}, \quad (2.66)$$

where ω_{ij} and g_{ij} are the transition frequency and coupling strength between i th and j th states, i.e., $\omega_{ij} = \omega_j - \omega_i$. Therefore, the dispersive shifts for the ground $|0\rangle$ and the first excited state $|1\rangle$ are given by

$$\omega_r \rightarrow \omega_r - \chi_{01} \quad \text{for } |0\rangle \quad (2.67)$$

$$\omega_r \rightarrow \omega_r - \chi_{01} + \chi_{12} \quad \text{for } |1\rangle \quad (2.68)$$

To see how much the dispersive shifts for the ground and first excited state are, let's consider the case where $\omega_{01} < \omega_r$ and thus $\chi_{01} < 0$ and $\chi_{12} < 0$. The new cavity frequency for the ground state will be from

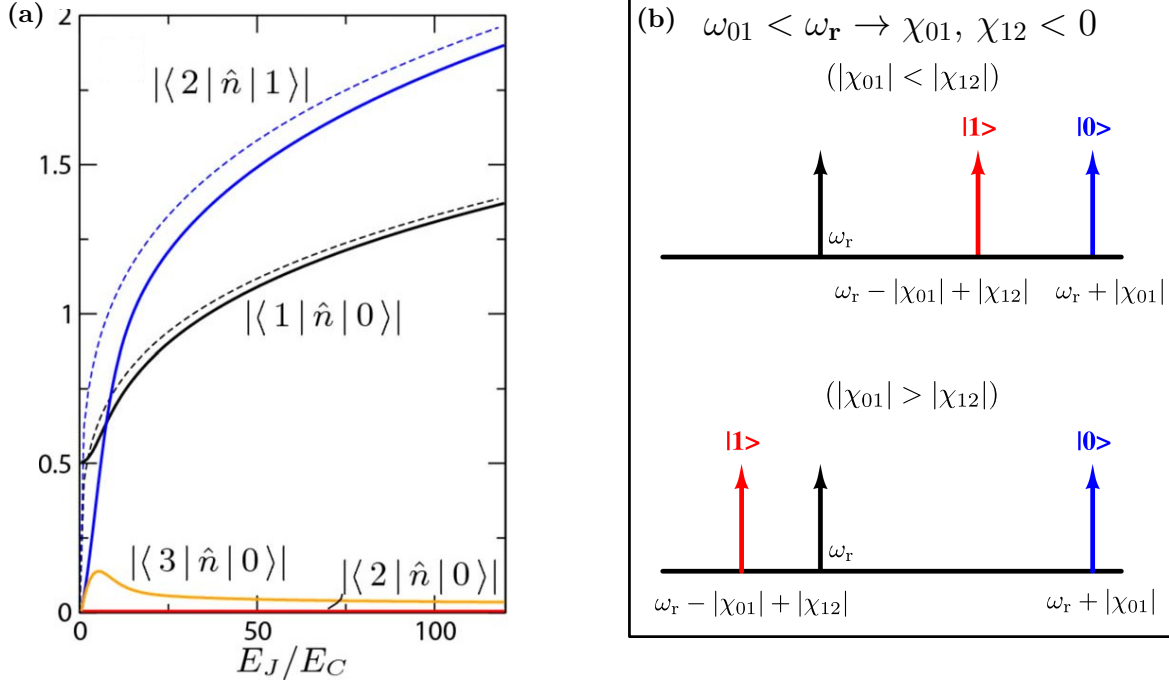


Figure 2.14: (a) The matrix element of Cooper-pair number operator, $\langle i | \hat{n} | j \rangle$ versus the ratio E_J/E_C is plotted. The matrix element is proportional to the coupling strength g_{ij} . The solid lines are exact solutions, and the dashed line are asymptotic behavior from Eq. (2.63). The only nearest-neighbor couplings are relevant in the regime of high E_J/E_C . This plot was excerpted from Ref. [25]. (b) The diagram of the dispersive shifts of transmon in the cavity. It is assumed that the detuning $\Delta = \omega_{01} - \omega_r$ is negative. The top diagram illustrates that if $|\chi_{01}| < |\chi_{12}|$, the dispersively shifted resonant frequency lies between the bare cavity frequency ω_r and the $\omega_r + |\chi_{01}|$. If $|\chi_{01}| > |\chi_{12}|$, the dispersive shift is negative. This diagram illustrates that the dispersive shift of the transmon is not symmetric with respect to the bare cavity frequency ω_r , unlike the symmetric shift expected in two-level system coupled to a harmonic oscillator from the JC Hamiltonian in Sec. 2.3.2. The graphs were taken from Ref. [25].

Eq. (2.64) $\omega_r' - \chi = \omega_r - \chi_{12}/2 - (\chi_{01} - \chi_{12}/2) = \omega_r - \chi_{01} = \omega_r + |\chi_{01}|$, and therefore, the dispersive shift δ_g becomes $\delta_g = |\chi_{01}|$. Similarly, the dispersive shift δ_e for the first excited state becomes $\delta_e = \chi_{01} - \chi_{12}$. In the case of our Meissner qubits that will be presented later, $|\chi_{12}| > |\chi_{01}|$. Consequently, $\delta_e = -|\chi_{01}| + |\chi_{12}| > 0$ and $0 < \delta_e < \delta_g$ in contrary that the dispersive shift is $\pm\delta$ in the case of the JC Hamiltonian—a two-level system coupled to a harmonic oscillator.

2.4 Rectangular microwave cavity resonator

In the circuit-QED architecture, a resonator or cavity is an essential element which serves as a harmonic oscillator. A microwave cavity is a 3-dimensional resonator where specific electromagnetic modes can form inside. In general, it can be made of a metal, superconductor or high dielectric constant material. The cavity modes are normally excited through a magnetic coupling loop or electric dipole antenna. For transmission

measurement through the cavity, two ports for input and output are mounted in the cavity

The dimension of the inner space determines the frequencies of cavity modes, i.e., resonant frequency. If each dimension of the cavity is a , b , and c ($a > b > c$), the resonant frequencies f_{mnp} become

$$f_{mnp} = \frac{c}{2\sqrt{\mu_r \epsilon_r}} \sqrt{\left(\frac{m}{a}\right)^2 + \left(\frac{n}{b}\right)^2 + \left(\frac{p}{c}\right)^2}, \quad (2.69)$$

where m, n , and p are integers. In the cavity, there can exist two types of modes: TE (transverse electric) and TM (transverse magnetic) mode. However, not all the combinations of m, n , and p are possible— $E = B = 0$ for certain combinations. The selection rules for TE and TM mode are as follows. For the TE mode,

$$m = \{0, 1, 2, \dots\}, n = \{0, 1, 2, \dots\}, p = \{1, 2, 3, \dots\}, m = n \neq 0 \quad (2.70)$$

For TM (transverse magnetic) mode,

$$m = \{1, 2, 3, \dots\}, n = \{1, 2, 3, \dots\}, p = \{0, 1, 2, \dots\} \quad (2.71)$$

Therefore, given that $a=5$, $b=22$, and $c=28$ mm, the lowest resonant frequency of the TE mode becomes TE₀₁₁.

Each mode holds specific distributions of electric and magnetic field inside the cavity, and in specially, we used the TE₀₁₁ to achieve the maximum electric coupling to transmon qubits. The TE₀₁₁ has the electric field antinode in the middle of the cavity as shown in Fig. 4.6(e). The expressions for the electric and magnetic field distributions of TE and TM modes are given in the following. For TE modes ($E_z = 0$),

$$E_x(x, y, z) = E_{x,0} \cos\left(\frac{m\pi x}{a}\right) \sin\left(\frac{n\pi y}{b}\right) \sin\left(\frac{p\pi z}{c}\right) \quad (2.72)$$

$$E_y(x, y, z) = E_{y,0} \sin\left(\frac{m\pi x}{a}\right) \cos\left(\frac{n\pi y}{b}\right) \sin\left(\frac{p\pi z}{c}\right) \quad (2.73)$$

$$E_z(x, y, z) = 0 \quad (2.74)$$

$$H_x(x, y, z) = H_{x,0} \sin\left(\frac{m\pi x}{a}\right) \cos\left(\frac{n\pi y}{b}\right) \sin\left(\frac{p\pi z}{c}\right) \quad (2.75)$$

$$H_y(x, y, z) = H_{y,0} \cos\left(\frac{m\pi x}{a}\right) \sin\left(\frac{n\pi y}{b}\right) \sin\left(\frac{p\pi z}{c}\right) \quad (2.76)$$

$$H_z(x, y, z) = H_{z,0} \cos\left(\frac{m\pi x}{a}\right) \cos\left(\frac{n\pi y}{b}\right) \sin\left(\frac{p\pi z}{c}\right) \quad (2.77)$$

For TM modes ($H_z = 0$),

$$E_x(x, y, z) = E_{x,0} \cos\left(\frac{m\pi x}{a}\right) \sin\left(\frac{n\pi y}{b}\right) \cos\left(\frac{p\pi z}{c}\right) \quad (2.78)$$

$$E_y(x, y, z) = E_{y,0} \sin\left(\frac{m\pi x}{a}\right) \cos\left(\frac{n\pi y}{b}\right) \cos\left(\frac{p\pi z}{c}\right) \quad (2.79)$$

$$E_z(x, y, z) = E_{z,0} \sin\left(\frac{m\pi x}{a}\right) \sin\left(\frac{n\pi y}{b}\right) \cos\left(\frac{p\pi z}{c}\right) \quad (2.80)$$

$$H_x(x, y, z) = H_{x,0} \sin\left(\frac{m\pi x}{a}\right) \cos\left(\frac{n\pi y}{b}\right) \cos\left(\frac{p\pi z}{c}\right) \quad (2.81)$$

$$H_y(x, y, z) = E_{y,0} \cos\left(\frac{m\pi x}{a}\right) \sin\left(\frac{n\pi y}{b}\right) \cos\left(\frac{p\pi z}{c}\right) \quad (2.82)$$

$$H_z(x, y, z) = 0 \quad (2.83)$$

The cavity modes were excited by dipole antennas which are simply straight metal wires. The microwaves were fed in through two SMA connectors. The length of two antennas set the coupling strength to the electromagnetic modes. The coupling strength was quantified by a external quality factor Q_e . The higher the Q_e , the weaker the coupling. We adjusted the length of the antennas to set the desired Q_e . The Q_e can be calculated using the Eq. 2.84 and Eq. 2.85 once the loaded quality factor Q_L and insertion loss IL are measured with known internal quality factor Q_i . The internal quality factor can be measured at a certain temperature simply by making the $Q_e \gg Q_i$ —the antennas made very short—and measuring the Q_L . In this case, $Q_i \approx Q_L$.

$$\frac{1}{Q_L} = \frac{1}{Q_e} + \frac{1}{Q_i} \quad (2.84)$$

$$IL = 20 \log\left(\frac{Q_i}{Q_i + Q_e}\right) \quad (2.85)$$

$$(2.86)$$

Chapter 3

Sample fabrication

3.1 Meissner transmon

In this section, we will describe how our Meissner qubits were fabricated. The Meissner qubits were fabricated by Zack Yoscovits in James Eckstein’s group as a collaboration. Thus we intend to summarize the fabrication procedures based on his Ph.D thesis[48] and to provide essential steps worth noting. One may want to refer to that thesis for more details.

Before we start to describe the detailed fabrication steps, we show the schematics of the Meissner qubit first in Fig. 3.1. Our Josephson junctions are conventional Josephson tunnel junctions with trilayer structure, aluminium/aluminium oxide/aluminium. The junctions were made using called double-angle or shadow-mask technique[49]. Such shadow mask method allows us to make a tiny junction (area less than $0.01 \mu\text{m}^2$) easily. After a bridge pattern—shadow mask—was defined by e-beam lithography, first aluminium film was deposited at a certain angle with respect to the surface normal. Then the top of the first aluminium film was oxidized normally by oxygen diffusion *in situ*—without breaking vacuum. The second aluminium film was evaporated at a different angle, making overlapped areas form a Josephson tunnel junction.

3.1.1 Substrate preparation

First, an appropriate substrate was chosen and cleaned before the growth of aluminium film. A c-plane sapphire (Al_2O_3) was chosen as a substrate to prepare for aluminium growth. A sapphire is widely used as a substrate for superconducting qubits, because it has very low loss tangent ($\tan \delta < 10^{-7}$), making it an ideal for microwave application. Both a-plane and c-plane sapphires were tested for aluminium growth and it turned out that the latter provided a better film quality in terms of roughness.

The first step to prepare the substrate was to sonicate it in the ultrasound bath of TCE (Trichloroethylene), acetone and IPA (Isopropyl alcohol) for five minutes each in order. This process should remove any organic contaminant residing on the surface. After this sonication, the sapphire was annealed in the furnace at 1110°C under an environment of ultra-high-pure oxygen at atmospheric pressure for six hours. This

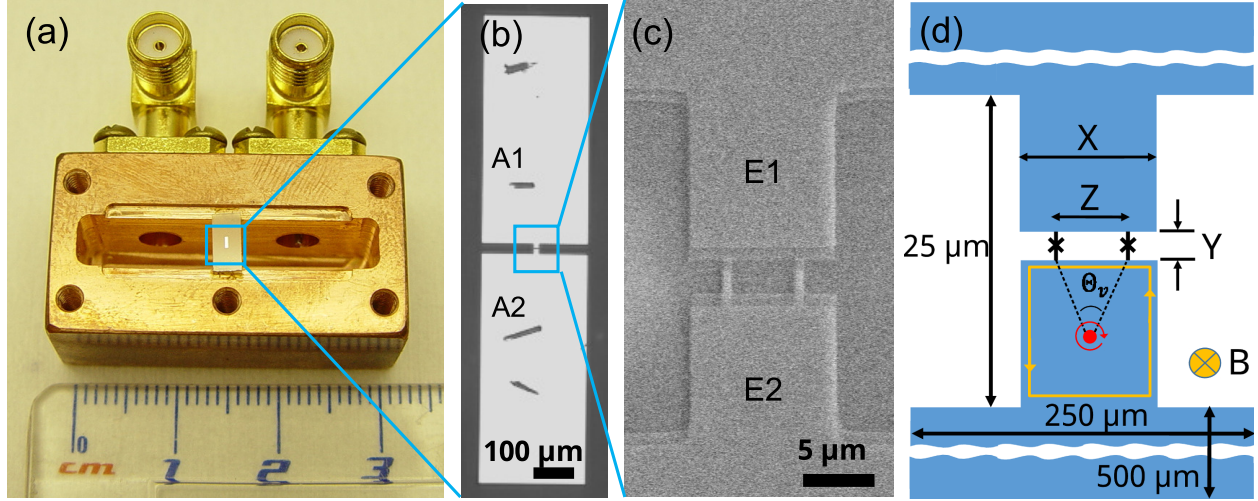


Figure 3.1: (a) Optical image of the Meissner transmon qubit fabricated on a sapphire chip, which is mounted in the copper cavity. (b) A zoomed-in optical image of the qubit. Two rectangular pads marked A1 and A2 act as an RF antenna and shunt capacitor. (c) Scanning electron microscope (SEM) image of the electrodes marked E1 and E2, and a pair of JJs. (d) Schematics of the Meissner qubit. The X, Y and Z denote the width, the distance between the electrodes, and the distance between two JJs, which are indicated by \times symbols. The red dot and circular arrow around it in the bottom electrode represent a vortex and vortex current flowing clockwise, respectively. Θ_v is a polar angle defined by two dashed lines connecting the vortex and two JJs. The orange rectangular loop on the boundary of the bottom electrode indicates the Meissner current circulating counterclockwise.

process may fill in oxygen vacancies near the surface of the sapphire. After the oxygen annealing process, the substrate went through the ultrasonic cleaning one more time.

3.1.2 e-beam lithography and removal of residue

To define a shadow mask pattern, multilayer of e-beam resist is needed to make a undercut below the topmost layer that acts as a shadow mask. To prepare for lithography, the clean substrate was first baked on a hotplate at 200 $^{\circ}\text{C}$ for 3 minutes to get rid of any water from the surface. Next, MMA EL-13 (Microchem) was spun at 2000 rpm and followed by baking at 200 $^{\circ}\text{C}$ for 3 minutes to completely remove solvent (anisole). After that, ZEP 520 A7 (Zeon Chemicals) ¹ was spun at 2000 rpm to become 300 nm thick and baked at 200 $^{\circ}\text{C}$ for 10 minutes. Finally, aquaSAVE—conductive polymer—to prevent charging during e-beam exposure was spun at 1500 rpm and was baked for 5 minutes at 70 $^{\circ}\text{C}$.

The e-beam lithography was performed using a Raith system. The e-beam of 20 kV was set with 10 μm aperture, giving a beam current of about 0.04 nA for small features such as JJ junctions and electrodes. The exposure dosage used was 160 $\mu\text{C}/\text{cm}^2$. For large antenna exposure, the aperture size was changed to

¹ZEP is a high performance e-beam resist with high resolution and high resistance to dry etching. It is developed by n-amyl acetate, whereas the MMA is developed by MIBK (Methyl isobutyl ketone). This allows the two layers to be developed using different temperatures and times which allow for the undercut to be controlled.

120 μm with a beam current of 5 nA, and the exposure dosage was 200 $\mu\text{C}/\text{cm}^2$.

To develop the e-beam resists, the aquaSAVE was first removed by rinsing it in water for 60 seconds—aquaSAVE is water-soluble. Next, the ZEP resist was developed by n-amyl acetate in an ice bath for 60 seconds, and rinsed with IPA to stop the development. After that, the MMA was developed in 1:3 MIBK:IPA for 140 seconds at room temperature.

It is common to have the residue of an e-beam resist left in regions developed—supposedly bare substrate. Such residue should be removed because otherwise it could make Josephson junctions unreliable over times[50], e.g., drift of critical current, and also could be a source of TLSs (Two level system) that would be a source of decoherence of superconducting qubits[51]. To remove such residue, the oxygen plasma in a RIE (Reactive ion etching) machine was performed to ash it. Finally, it was etched for 30 seconds in BOE (buffered oxide etch) solution, which is believed to roughen the surface creating nucleation sites, leading to a flatter film. The substrate was rinsed in deionized water and blown dry with nitrogen gas.

3.1.3 Deposition and post-deposition process

Once the pattern was defined, the substrate was mounted on a sample holder, loaded into the transfer chamber of MBE system, and left there overnight for outgassing. The sample holder was transferred to the main chamber with a base pressure of 10^{-11} Torr. The aluminium cell when heated created a flux of atomic beam of aluminium. The aluminum cell was pointed to the substrate at a certain angle for evaporation. The first layer of aluminium film was deposited with 45 nm thickness. Next, the sample holder was transferred to the oxidation chamber, where the deposited aluminium film was exposed to a mixture of 10% Ar and 90% O_2 gases with a desired pressure. The critical current density J_c of a Josephson junction made depends on the product of the oxygen partial pressure P and the exposure time t . Therefore, it would be useful to have a calibration graph of the critical current density versus the product of partial pressure and exposure time— J_c versus $P \cdot t$. After the oxidation process, the sample holder was moved back to the main chamber and rotated by 180 degree for the second evaporation of aluminium.

Once the sample was taken out of the MBE chamber, the aluminium films were lift-off in acetone overnight. Next the substrate was spun with photoresist to protect it from sapphire debris created during dicing, and then diced into individual pieces of transmon qubits. A couple of secondary electron microscope (SEM) images of the Josephson junction area are shown in Fig. 3.2. The images are magnified from Fig. 3.2(a) to Fig. 3.2(d) in the order. In Fig. 3.2(b), two electrodes connected by two Josephson junction bridges are shown. The actual Josephson junction formed by the shadow evaporation can be seen in the yellow dashed circle in Fig. 3.2(d).

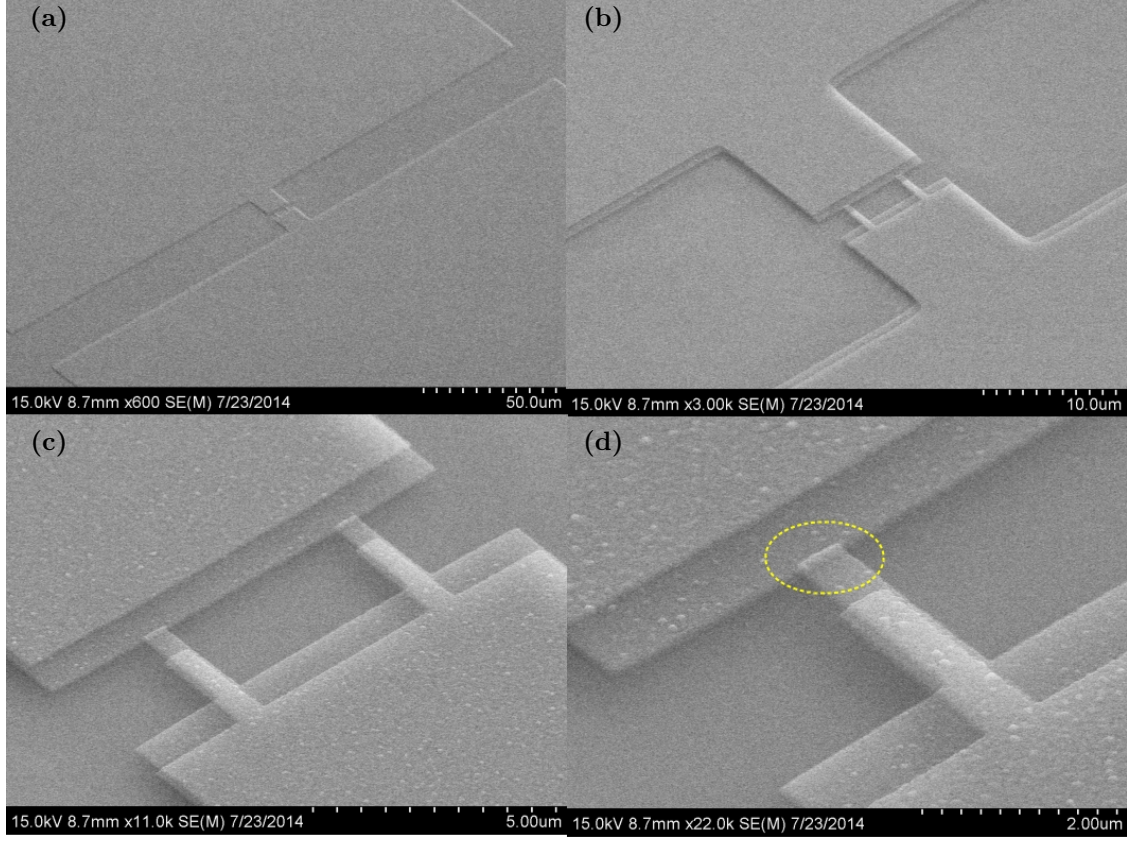


Figure 3.2: SEM images of tilted view of a Meissner qubit taken in four different magnifications: (a) 600 , (b) 3k , (c) 11k and (d) 22k . In (a), the width of the antennas can be seen 250 μm . In (b), the electrodes and JJ bridges are shown. In (c) and (d), the shadows formed by the double-angle evaporation are visible. The Josephson junction can be seen in the dashed yellow circle.

3.2 Design rules and parameters of transmon

In this section, we will explain how transmon parameters and corresponding experimental parameters were chosen. In fabricating a transmon-type qubit, it is important to choose appropriate junction parameters and to achieve the design goal. First, two parameters E_J and E_C (Josephson and charging energy) should be selected. Since the JJ-based superconducting qubits are operated in different parameter space of E_J and E_C , the combination of the two energy scales is critical . In the case of the transmon, they are determined by taking into account the qubit transition frequency and the ratio E_J/E_C . Those two numbers should be enough to determine both E_J and E_C . First, the qubit transition frequency f_{01} —energy difference between the ground and first excited state divided by the Planck constant \hbar —is approximately given by $f_{01} \approx \sqrt{8E_J E_C}/\hbar$. Thus, the f_{01} sets the product $E_J E_C$. Second, the ratio of the Josephson energy to the charging energy, E_J/E_C , determines the charge dispersion and anharmonicity, as explained in Sec. 2.2. Normally, the transmon should work in the regime of $10 < E_J/E_C < 10^4$. If the ratio is too small, then

the charge dispersion becomes large, leading to increase in the dephasing rate, but anharmonicity becomes larger. In contrast, if the ratio is too large, then the charge dispersion decreases, but the anharmonicity decreases. In practice, one may typically choose E_J/E_C between 50 and 100.

Once E_J and E_C are selected, we should choose the critical current I_c of the Josephson junction and the total capacitance C_Σ . Note that $E_J = \hbar I_c / (2e)$ and $E_C = e^2 / (2C_\Sigma)$. First, since the critical current is the product of critical current density J_c and junction area A ($I_c = J_c \cdot A$), we have a degree of freedom for either the J_c or A . The J_c totally depends on the thickness of the aluminium oxide layer, so the J_c can be controlled by oxidation parameters. As explained in the previous section, the J_c depends on the product of oxygen partial pressure (P) and oxidation time (t). Based on the calibration data of J_c versus $P \cdot t$, the desired critical current density can be achieved. Meanwhile, the junction area (A) can be defined by the e-beam lithography with good precision. Typically, the junction area is an order of $0.1 \mu\text{m}^2$. The importance of the junction area lies in the fact that it sets the junction capacitance $C_J = \epsilon A / d$, where ϵ is the dielectric constant of aluminium oxide, A the junction area, and d the thickness of aluminium oxide. For a junction size $0.1 \mu\text{m}^2$ with 0.5-1 nm thick oxide layer, the capacitance $C_J \approx 10 \text{ fF}$ [52]. In the case transmon, the total capacitance is dominated by the shunt capacitance C_s , typically, $C_s \gg C_J$, so the junction size of an order of $0.1 \mu\text{m}^2$ should be fine. If the junction size is too small, there might be deviation of the critical current from the design value. Now, regarding the charging energy, since the total capacitance is close to the shunt capacitance, it is a matter of choosing the shunt capacitance to find E_C . The shunt capacitance can be found by a microwave simulation software given a geometry of a shunt capacitor. In our work, the shunt capacitance $C_s \approx 70 \text{ fF}$ is provided by the two large rectangular pads of an order of a few hundreds μm on each side.

Chapter 4

Experimental setup and preparation

4.1 Microwave setup in cryogenics

In general, superconducting qubits should be measured at low cryogenic temperature. The low transition temperature T_c of a superconductor (aluminium, $T_c \sim 1.2$ K) and more importantly the qubit transition frequency of an order of GHz¹ require the operation of a dilution refrigerator ($T < 50$ mK) since the thermal energy $k_B T$ should be smaller than the qubit transition frequency $\hbar\omega$, i.e., $k_B T \ll \hbar\omega$. Also, superconducting qubits are very sensitive to environmental noise, so care must be taken in cryogenic microwave setup to minimize any possible noise coming down to samples and also to thermalize each component well. We will describe how the cryogenics wiring for both RF and DC was performed, and also what kind of noise filtering method was used.

4.1.1 Cryogenic wiring: RF

Our microwave setup was designed to measure the transmission of microwave through two-port cavity resonators. For the simplest setup, all we need would be two coaxial microwave transmission lines for input and output running from the top of the fridge insert to the mixing chamber. However, since one of the most important design considerations for measuring qubits is to minimize the noise reaching the cavities (or samples), various microwave components should be normally installed at different temperature stages for their own reasons. The schematic diagram of the cryogenic wiring is shown in Fig. 4.1. Also, the optical photographs of the fridge insert and each temperature stage were depicted in Fig. 4.2

Let us look at the input line setup first. From room-temperature port down to mixing chamber, a series of microwave attenuators were installed to eliminate the room-temperature black-body radiation and stray radiation that might reach samples. Thus the coaxial input line was heavily attenuated by attenuators at various temperature stages. The attenuators were mounted at temperature stages mainly for two reasons: noise reduction and thermalization. As for the noise reduction, attenuators attenuate noise, especially,

¹6 GHz corresponds to 0.3 K in energy scale.

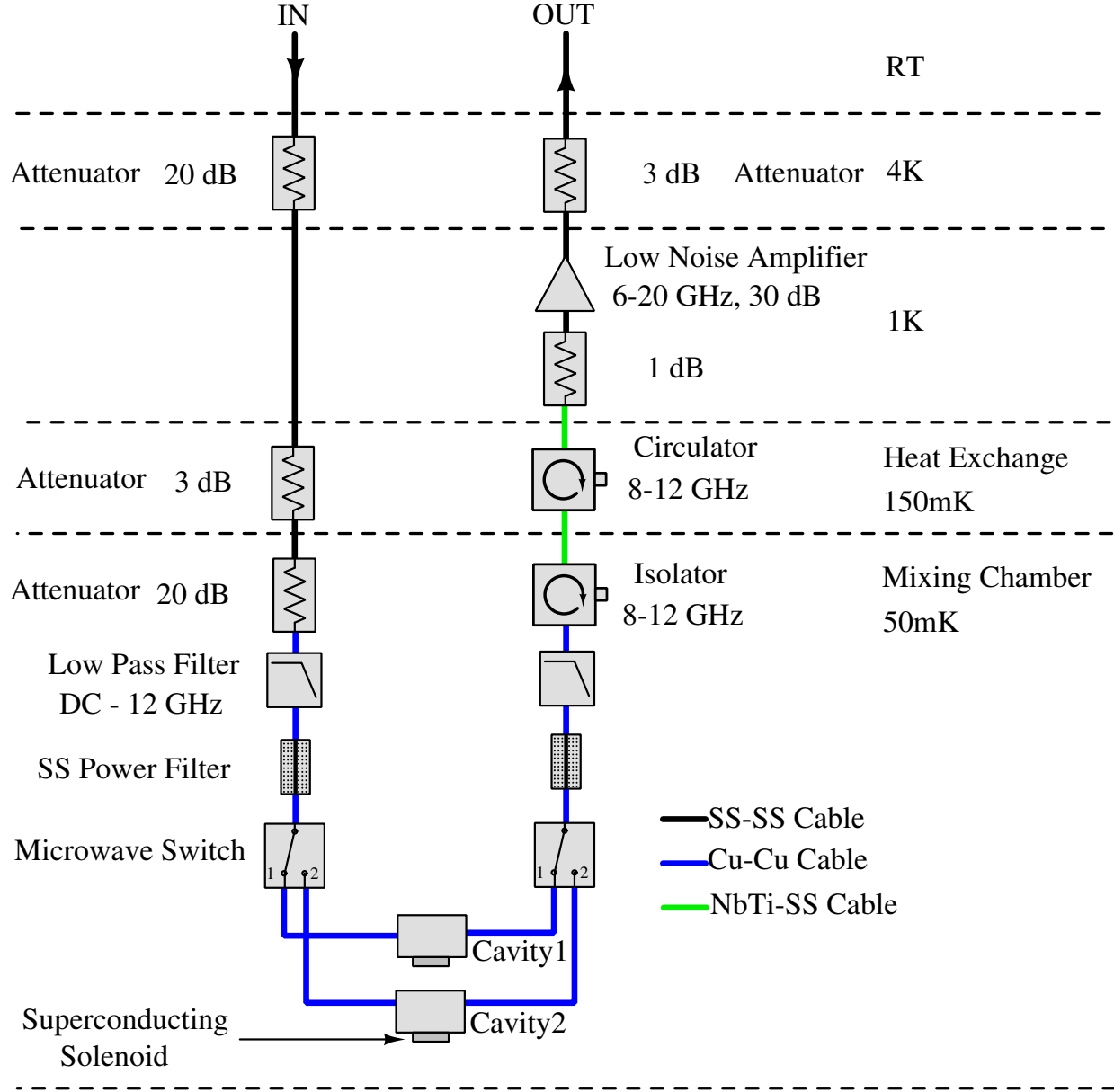


Figure 4.1: Schematic diagram of RF cryogenic wiring in the dilution refrigerator. Each temperature stage is separated by the dashed lines. This microwave setup is dedicated for transmission measurement only, as seen from all components connected in series. Each microwave components must be anchored at each temperature stage and well thermalized. The detailed description on each component can be found in the text.

room-temperature black-body radiation. It is crucial to prevent such thermal radiation from sneaking into the sample stage because if not properly filtered out, it could adversely relax qubit states and act as a decoherence source. For example, a 20 dB attenuator reduces the effective noise temperature of 300 K to 3 K by a factor of 100. Also, it should be noted that attenuators have working frequency range—typically DC-18 GHz, so they can not filter out out-of-band noise.

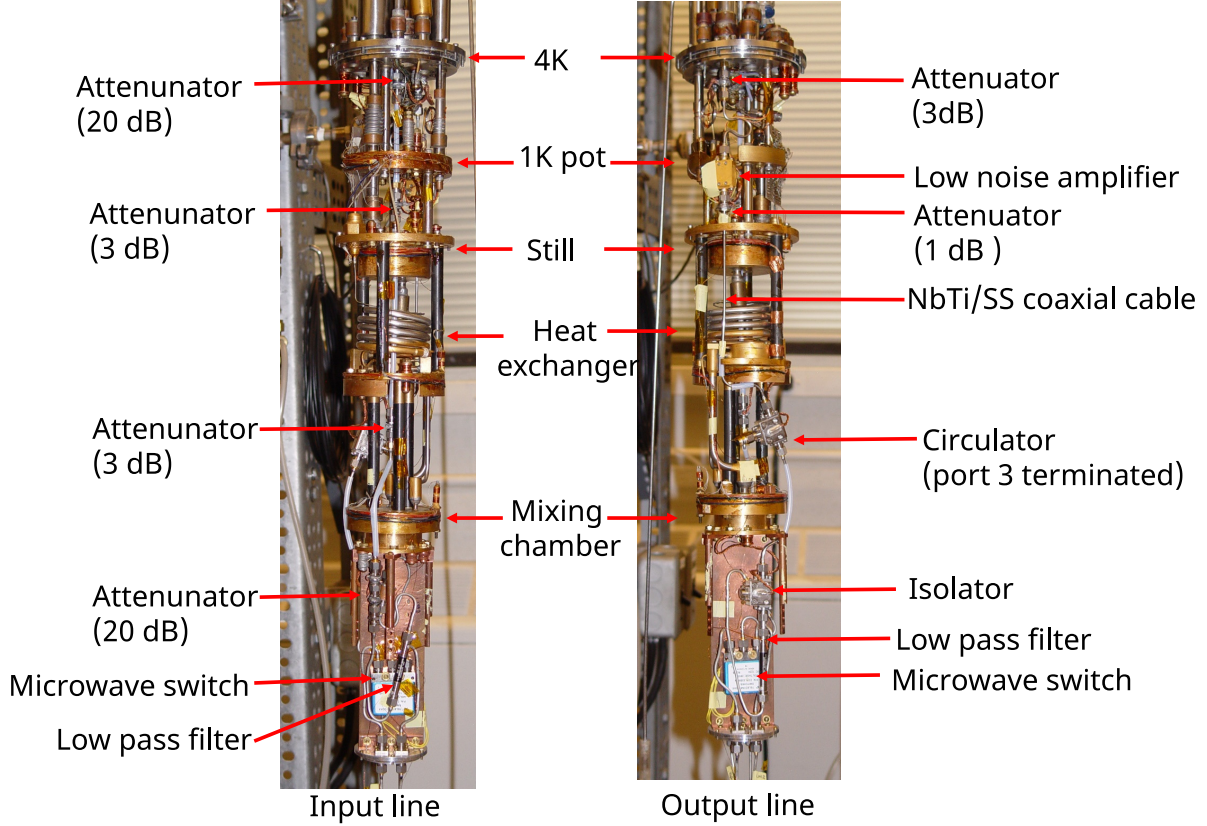


Figure 4.2: Optical photographs of the dilution fridge insert. All microwave components are thermally anchored at temperature stages. The components at different temperature stage are connected by either a stainless steel (SS) semi-rigid coaxial cable or NbTi-SS superconducting cable. The section of Faraday cage where samples are mounted is not shown here, but in Sec. 4.3.3. Also, two stainless steel powder filters are not clearly visible due to small size.

As for the other role of the attenuators, the thermalization of the center conductor of a semi-rigid cable is important because it emits black-body radiation that could induce the decoherence of qubits. Also, in practice, the hot center conductor could raise the base temperature of the fridge. However, the center conductor is hard to cool down because of the dielectric, i.e., usually bad thermal conductor, while the outer conductor or shield can be thermally anchored to thermal bath quite well. Attenuators can thermalize the center conductor due to the network of resistors between the center and outer conductor, i.e., better heat conduction between the center and outer conductor than just through the dielectric.

At the mixing chamber stage, a commercial low-pass filter (K&L Microwave, 6L250-12000, DC-12 GHz) and home-made stainless steel powder filter were inserted for noise filtering at both the input and output side of the cavities. The SS powder filters had a cutoff frequency of about 8.5 GHz. Those two filters are expected to block out-of-band (>12 GHz) noise. More details about filtering will be discussed in Sec. 4.1.3.

Next, after the filters come microwave switches. We used the microwave switches (Teledyne, CCR-

33S6O-N) between the SS powder filter and cavities to multiplex two cavities. They are broadband (DC-18GHz), SPDT(Single Pole, Double Throw), latching electromechanical switches. The latching actuators, i.e., solenoids, switch a microwave signal from a common input (com) to either of two outputs(1 and 2). Because of latching mechanism, they only take short current pulses (10 ms max) for switching, which means no need to sustain DC current, which definitely would heat up the mixing chamber. The maximum actuation current at room-temperature is 65 mA. For switch operation at cryogenic temperature (below 4.2 K), we applied about 1.6 V DC voltage using a Keithley source (Keithly, K2400) for a fraction of second ² This caused the base temperature to rise by about 50 mK, but the temperature normally could be stabilized within 30 minutes. To minimize such heat load, it is advised to build a simple electronic circuit that can create a voltage pulse with an order of millisecond consistently in the future.

Now we turn to the output line, which requires quite different configuration from the input line. Unlike the input line, the output line can not be heavily attenuated with attenuators, as the output signal would be too small—we lose too much photons that come out of the cavity. On the other hand, there must be a way to block out noise coming down to the output port of the cavities. To solve this dilemma, special microwave components called circulators (Pamtech, CTB1296K-2) or isolators (Pamtech, XTE1271K) are normally used. A circulator is a three-port device which allows only one-way pass; microwave signal entering port 1 comes out of port 2 only (symbolically, $1 \rightarrow 2$). Similarly, $2 \rightarrow 3$ and $3 \rightarrow 1$. An isolator is basically a circulator with the port 3 terminated with 50Ω . Thus, within the bandwidth of those components, signal can pass, but noise can be blocked as much as isolation is allowed, typically, 20 dB. We used two isolators ³ to increase the isolation level at two temperature stages simply due to spacial limitation at the mixing chamber. Those two devices also protect superconducting qubits from the noise generated by a low temperature amplifier at 1K pot stage. However, they do not block out-of-band noise as much as in-band noise. Another drawback is that they use magnetic material for asymmetric nature of their behavior, and could impose offset magnetic field on samples. Fortunately, circulators with magnetic shields have become available recently, so they should be used for experiment sensitive to stray magnetic field.

The outgoing signals need amplified as they are normally quite small. We used a commercial low noise amplifier (Low Noise Factory, LNF-LNC6-20A) at 1K stage. Such amplifier is made of HEMP (High-Electron-Mobility Transistor) to work at cryogenics temperature and has very low noise temperature below 10 K. It requires stable power supply that normally is purchased together with the amplifier itself. These are all sensitive to static charge, so care must be taken in handling them. The amplifier consumes about 22 mW and it seemed to heat up the center conductor of a coaxial cable raising the temperature of the heat

²At 4.2 K, the resistance of the actuator coil is about 30Ω . So 1.6 V gives 50 mA.

³A circulator was used as an isolator by attaching a 50Ω microwave terminator to port 3.

exchanger slightly. Thus 1 dB attenuator—so without too much signal loss—was inserted between the LNA (Low Noise Amplifier) and isolator to thermalize the center conductor.

The microwave components mentioned so far were interconnected by various microwave semi-rigid cables: stainless steel, copper and NbTi cables. We mainly used a stainless steel semi-rigid cable for both input and output lines except specific position. The stainless steel cable (Microstock, UT-85SS-SS) was chosen to minimize the heat conduction between temperature stages as the stainless steel has low thermal conductivity. The trade-off, of course, is high cable loss, i.e., low electrical conductivity, but this is not a problem on the input transmission line as we can simply use higher microwave power. The copper cables (Microstock, UT-85C-TP) were used at the mixing chamber, where all microwave components should be in thermal equilibrium, since copper is a good electrical and thermal conductor. Also, they are quite flexible mechanically, so it's much easier to form a desired shape than a SS cable. Finally, the superconducting NbTi cable (Coax Co., LTD., SC-219/50-NbTi-SS) was used between the isolator and 1 dB attenuator. This cable or NbTi has higher electrical conductivity (superconducting NbTi) and lower thermal conductivity than the SS cable, so it was ideal to place before the LNA. The SS outer shield was chosen for the ease of solderability; NbTi is hard to solder in the air.

4.1.2 Cryogenic wiring: DC

In the previous section, the microwave transmission line setup in the dilution fridge is described, and here we look into DC setup. The DC setup is necessary for the amplifier, microwave switch, and solenoids. Just like the microwave components are thermally anchored at each temperature stage, the DC lines, i.e., wires, need thermalization at the temperature stages. Here the thermalization means that an object has so good thermal contact to temperature bath that the temperature of the object is maintained at the same temperature as the bath. A common technique for good thermalization is to make a small copper or brass bobbin, wind the wire around the bobbin in enough length, and fix it to the bobbin with an epoxy with good thermal conductivity. The length of the wire wound around the bobbin should be long, otherwise, it wouldn't have enough thermal contact to the bath temperature ⁴.

Related with the length of the wound wire, the type of wire should be chosen to minimum amount of heat between the temperature stages. Thus, high-resistive wires are usually used for DC wires, unless a high current is required to flow. The high-resistive wires have much lower thermal conductivity than a normal metal due to high resistivity. Such wires can be purchased from Supercon, Inc. or Lake shore cryogenics.

First, we look at the low noise amplifier (LNA). The LNA is powered by three lines: V_g (gate voltage),

⁴There is a guideline to the required length for different types of wire in Lake shore cryogenics website.

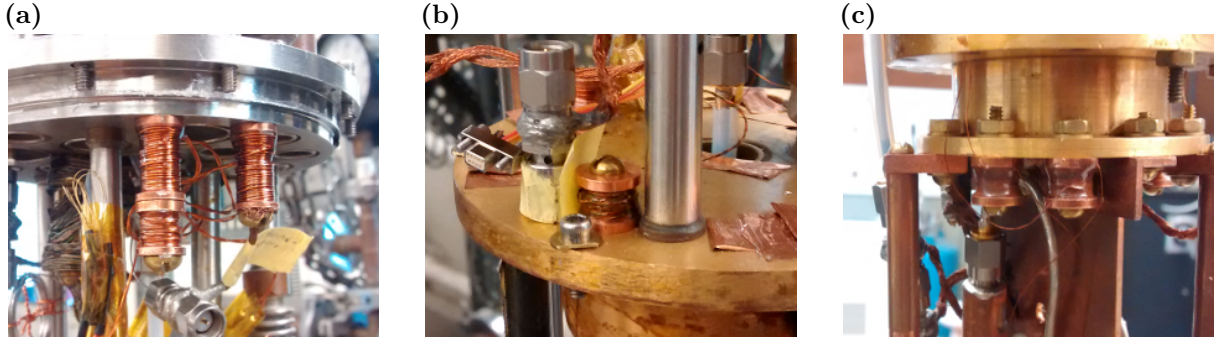


Figure 4.3: (a) Copper bobbins mounted at 4.2 K stage were used for thermal anchoring of copper wires that run down from room-temperature stage. Copper wires were seen wound around the copper bobbins. (b) A copper bobbin with high-resistive wires was mounted on the still. The wires were used for the DC line of the microwave switches on the mixing chamber. (c) Copper bobbins were mounted on the mixing chamber. The superconducting wires were wound around the copper bobbins and glued with mixture of copper powder and Stycast epoxy. The copper powder mixture serves as a low pass filter to suppress high-frequency noise.

Vd (drain voltage) and GND (ground). However, it doesn't require high current, so high-resistive wires (Advance, $1.8 \Omega/\text{ft}$, Pelican wire company) were connected from the three BNC connectors at room-temperature to 1K pot stage. The wires were wound around a copper bobbin many times and glued with Stycast for thermal contact between the wire and bobbin.

The microwave switches need three DC lines, one for GND and the other two for coil 1 and coil 2. A twisted pair of 30 AWG magnet copper wire was connected from BNC connectors at RT to a copper bobbin at 4.2 K stage. Then high-resistive wires (WQT-36-25, Quad-Twist 36 AWG wire, Lake shore cryogenics) were connected from the 4.2 K stage to the still, and again to the mixing chamber. A pair of the wire was connected to the GND and the other two wires to the coil 1 and 2 of both microwave switches in parallel. Epoxy (M-bond 610 Adhesive, Ted Pella) was used for glue.

The DC wiring for the superconducting solenoids is a bit different from the LNA and RF switches. We wanted to be able to flow high current to the solenoids. Therefore, a superconducting wire (SC-T48B-M-0.1mm, Supercon Inc.) instead of a high-resistive wire was used from the 4.2 K stage down to the mixing chamber. However, the connection from RT down to 4.2 K was made by multiple 30 AWG magnet wires ⁵. The superconducting wire was thermally anchored at 1K pot, still, heat exchanger, and mixing chamber using copper bobbins. In particular, the superconducting wire was glued to the copper bobbin with mixture of copper powder and Stycast. The copper powder is expected to filter out high-frequency noise ($> 1 \text{ GHz}$) by skin effect. A few examples of thermal anchor with copper bobbin are shown in Fig. 4.3.

⁵A brass wire can be used, which has lower electrical conductivity, but lower thermal conductivity than a copper wire.

4.1.3 Noise filtering

Filtering out noise that might come to samples is critical to have long coherence time of superconducting qubits. As explained in the previous section, the cryogenic microwave wiring was set up in such a way to minimize electromagnetic noise that could reach samples. Several methods were implemented for noise filtering. First, the attenuators were used to reduce the black-body radiation that comes from the higher temperature stage. For example, the 20 dB attenuator at 4 K aims to eliminate the 300 K black-body radiation. The attenuation value was chosen in such a way that the noise temperature reduced by the attenuator is lower than the temperature of the attenuator itself. Second, the commercial LPFs (Low Pass Filter) filter out photon noise above 12 GHz. They would be helpful on the output line to filter out the out-of-band noise of the isolators (bandwidth: 8-12 GHz). However, since those filters are made from lumped elements, they start to fail at certain high frequency (presumably, tens of GHz). Third, the homemade stainless steel powder filters were used to cover the high frequency range where the attenuators and LPFs do not work effectively [53]. The SS powder filters were designed to have a cutoff frequency of about 8.5 GHz and characteristic impedance of 50 Ω . See the appendix A.2 for more detail. Lastly, we used microwave absorbing compound to minimize the infrared radiation [54]. It is known that the stray in-fared radiation causes a significant loss in superconducting qubits due to creation of quasi-particles [55]. This black material can help absorb the stray infrared black-body radiation coming into the Faraday cage.

4.2 Microwave room-temperature electronics setup

In this section, we will describe the microwave electronics setup at room-temperature. This microwave setup is used to create microwave pulses for readout and spectroscopy and to measured transmitted microwave signals. The schematic diagram of the electronics setup is shown in Fig. 4.4.

4.2.1 Pulse generation: microwave modulation

In the measurement of transmons, we used microwave square pulses for both spectroscopy and readout. The pulses were synthesized by mixing a strong continuous microwave from a microwave generator (E8267C, Agilent; HP 8341B, Hewlett-Packard) and a square voltage pulse from an arbitrary waveform generator (AWG520, Tektronix) with several microwave mixers (M8-0420LS, Markis; ZX05-153, mini-circuit). The strong microwave signal is fed into local oscillator port (LO) and the voltage pulse into intermediate frequency port (IF) of a mixer; the resulting microwave pulse comes out of the RF port of the mixer.

We will look into the readout pulse generation section in Fig. 4.4 (blue dashed square box); the spectro-

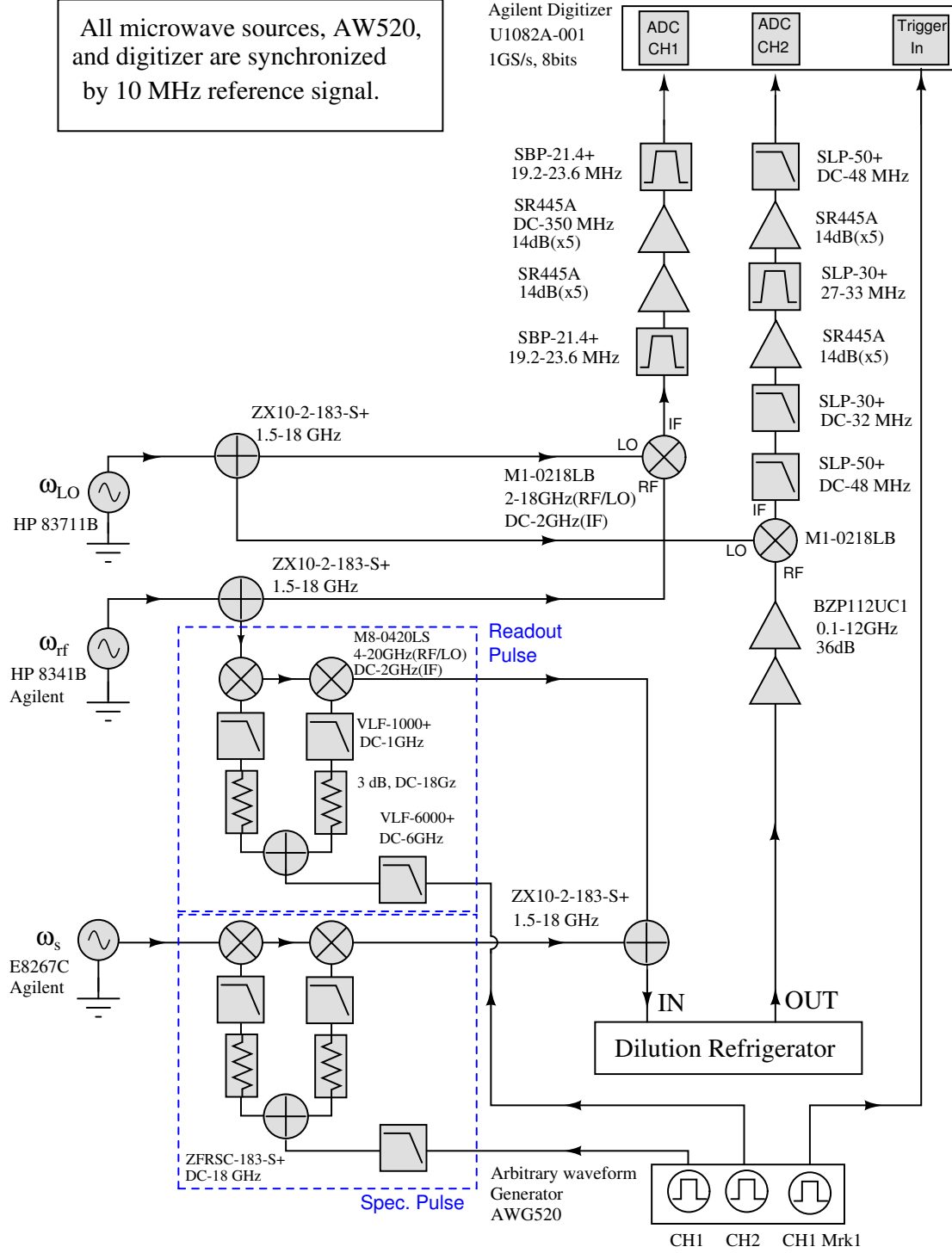


Figure 4.4: Schematic diagram of room-temperature microwave electronics setup. The arrow heads indicate the propagating direction of microwave or voltage pulses.

scopic pulses were created in the same way as the readout pulses except that a different microwave source (E8267C, Agilent) was used. The continuous microwave source ω_{RF} is divided by a power splitter/combiner

(ZX10-2-183-S+, Mini-circuit); one is used to create microwave pulse and the other one to create a reference signal that is used in demodulation later. The split microwave signal is mixed by a microwave mixer (M8-0429LS, Markis) with a square voltage pulsed generated by an arbitrary waveform generator (AWG520, Tektronix). The voltage pulse passes through a low-pass filter (VLF-1000+, Mini-circuit) and a 3 dB attenuator to suppress harmonics and any reflections that could exist.

In creating microwave pulses, it is essential to keep on/off ratio high enough to avoid any leakage of microwave tone to qubits; this could cause ac Stark shift by leakage readout photon or unexpected qubit operations. The on/off ratio is the ratio of voltage amplitudes in decibel when a pulse is on and off. Normally, the on/off ratio greater than at least 60 dB is required in qubit measurement. The leakage of LO microwave signal is always present in mixers and deteriorates the on/off ratio—this leakage is normally characterized by LO-RF *isolation* in the datasheet. To remedy this problem, we used two or three mixers in series to increase the isolation from LO to RF port, thus increasing the on/off ratio of microwave pulses. The actual on/off ration was measured using a spectrum analyzer (HP8556B, Hewlett Packard) in the way described in the appendix B.

4.2.2 Readout: microwave demodulation

For readout of the state of qubits, we need to measure the transmitted microwave signal through cavities; the state of qubit is encoded in the amplitude of the transmitted signal. The microwave signal is nothing but a high-frequency sinusoidal voltage with a certain amplitude and phase— $V(t) = V_0 \sin(\omega t + \phi)$. To measure the amplitude V_0 and phase ϕ , we used heterodyne method, where the GHz signal is down-converted to MHz signal which in turn is readily acquired by a high-speed digitizer (U1082A-001, Agilent). The down-conversion is necessary since GHz frequency is too high to be read directly by a digitizer. In practice, a RF signal is mixed with a LO signal to create an IF signal.

To show how the heterodyne technique works, we use mathematical expression for V_{RF} , V_{LO} , and V_{IF} as RF, LO and IF voltage signals; $V_{\text{RF}}(t) = V_{\text{RF}}^0 \sin(\omega_{\text{RF}}t + \phi)$ and $V_{\text{LO}}(t) = V_{\text{LO}}^0 \sin(\omega_{\text{LO}}t)$, where ϕ is a phase shift with respect to a reference signal. When two signals are mixed, two sine waves with frequencies

$|\omega_{\text{RF}} - \omega_{\text{IF}}|$ and $|\omega_{\text{RF}} + \omega_{\text{IF}}|$ are created; the higher one is filtered out normally by a low-pass filter.

$$V_{\text{IF}}(t) \propto V_{\text{RF}} \times V_{\text{LO}} \quad (4.1)$$

$$= V_{\text{RF}}^0 \sin(\omega_{\text{RF}}t + \phi) \times V_{\text{LO}}^0 \sin(\omega_{\text{LO}}t) \quad (4.2)$$

$$= \frac{V_{\text{RF}}^0 V_{\text{LO}}^0}{2} [\cos((\omega_{\text{RF}} - \omega_{\text{LO}})t + \phi) - \cos((\omega_{\text{RF}} + \omega_{\text{LO}})t + \phi)] \quad (4.3)$$

$$= \frac{V_{\text{RF}}^0 V_{\text{LO}}^0}{2} [\cos(\omega_{\text{IF}}t + \phi) - \cos((\omega_{\text{RF}} + \omega_{\text{LO}})t + \phi)] \quad (4.4)$$

$$(4.5)$$

After the IF is filtered by a low-pass filter, only the signal with the frequency ω_{IF} remains:

$$V_{\text{IF}}(t) = V_{\text{IF}}^0 \cos(\omega_{\text{IF}}t + \phi) \quad (4.6)$$

Here the amplitude of V_{IF} is proportional to that of V_{RF} and the phase shift ϕ is the same as that of V_{RF} ; thus we can measure the amplitude V_{RF} and the phase shift ϕ of the RF signal. The illustration of the demodulation process is depicted in Fig. 4.5.

To extract both the amplitude and phase, we used digital homodyne as follows. Let's denote an IF signal as $V_{\text{IF}}(t) = V(t) \sin(\omega_{\text{IF}}t + \phi)$. Then $V_{\text{IF}}(t)$ can be decomposed into in-phase and out-of-phase components (with respect to $\sin \omega_{\text{IF}}t$).

$$V_{\text{IF}}(t) = V(t) \sin(\omega_{\text{IF}}t + \phi(t)) \quad (4.7)$$

$$= [V(t) \cos \phi] \sin \omega_{\text{IF}}t + [V(t) \sin \phi] \cos \omega_{\text{IF}}t \quad (4.8)$$

$$= I(t) \sin \omega_{\text{IF}}t + Q(t) \cos \omega_{\text{IF}}t \quad (4.9)$$

$$(4.10)$$

$I(t)$ and $Q(t)$ are called in-phase and out-of-phase (or quadrature) components of V_{IF} . In our measurement, I (and Q) was obtained by integrating the product of V_{IF} and $\sin \omega_{\text{IF}}t$ (and $\cos \omega_{\text{IF}}t$) over one period $T = 2\pi/\omega_{\text{IF}}$.

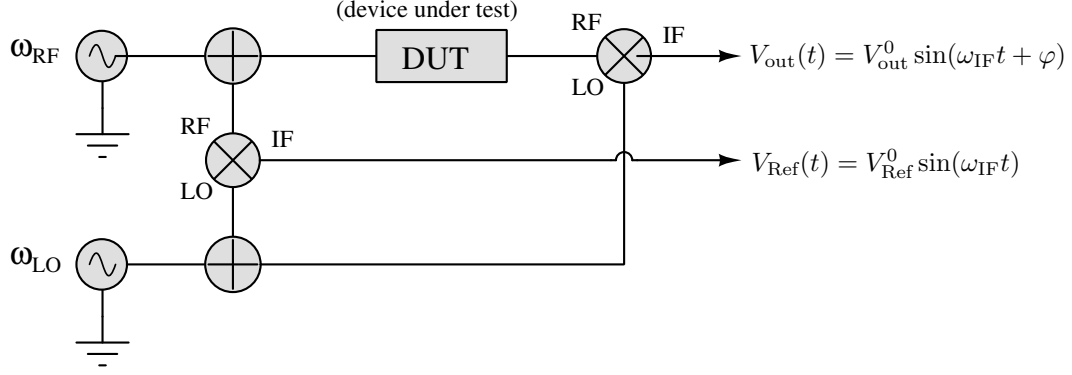


Figure 4.5: Schematic diagram of demodulation setup. The round symbol with cross is a microwave power splitter/combiner.

$$\langle I(t) \rangle = \frac{2}{T} \int_0^T V_{\text{IF}}(t) \sin(\omega_{\text{IF}} t) dt = \frac{2}{T} \int_0^T V(t) \sin(\omega_{\text{IF}} t + \phi) \sin(\omega_{\text{IF}} t) dt \quad (4.11)$$

$$= V(t) \cos \phi \quad (4.12)$$

$$\langle Q(t) \rangle = \frac{2}{T} \int_0^T V_{\text{IF}}(t) \cos(\omega_{\text{IF}} t) dt = \frac{2}{T} \int_0^T V(t) \sin(\omega_{\text{IF}} t + \phi) \cos(\omega_{\text{IF}} t) dt \quad (4.13)$$

$$= V(t) \sin \phi \quad (4.14)$$

$$V(t) = \sqrt{\langle I(t) \rangle^2 + \langle Q(t) \rangle^2} \quad (4.15)$$

$$\phi(t) = \tan^{-1}(\langle Q(t) \rangle / \langle I(t) \rangle) \quad (4.16)$$

$$(4.17)$$

Here, we assumed that the voltage amplitude $V(t)$ varies slowly compared to the IF signal frequency ω_{IF} . We used 25 MHz of the IF frequency and the period was 40 ns. The integration was carried out in Labview to get the voltage amplitude $V(t)$ and the phase shift $\phi(t)$. This digital homodyne in effect made data decimated.

For this digital homodyne, the signal $\sin \omega_{\text{IF}} t$ that acts as a LO signal —we call a reference signal— was created by mixing the readout microwave source and a new microwave source (HP 8371B, Hewlett Packard) by a mixer (M1-0218LB, Markis); the IF signal with 25 MHz is created. This IF travels through two bandpass filters (SBP-21.4+, Mini-circuit) and a room-temperature RF amplifier (SR445A, Stanford Research Systems), and is acquired by a high-speed digitizer (U1082A-001, Agilent). The amplitude of the signal was normalized to unity and used for the digital homodyne.

The transmitted signal coming out of the dilution fridge was first amplified by two room-temperature RF amplifiers (BZP112UC1, B&Z Technologies) before it was mixed with the LO signal. The resulting

25 MHz IF signal experiences a series of filters and amplifiers as shown in Fig. 4.4. Those filters were to remove the high harmonics, high-frequency noise. Finally, the IF signal was digitized, and post-processed to extract either amplitude and phase, when combined with the reference signal. The post signal-processing was performed using Labview programs in a computer.

In the setup, all microwave sources, the arbitrary waveform generator and digitizer were synchronized by 10 MHz reference signal provided by a Rubidium frequency standard (FS725, Stanford Research Systems).

4.3 Measurement preparation: sample mounting and cool-down

4.3.1 Copper cavity resonator

In measuring our superconducting qubits, we used a rectangular microwave cavity made of copper. The main reason why we chose copper instead of a superconductor such as aluminium was because we had to apply an external magnetic field from outside the cavity. A OFHC (Oxygen-free high thermal conductivity) copper was precisely machined in the chemistry machine shop. The photograph of a disassembled cavity is shown in Fig. 4.6(a). Two right angle SMA connectors serve the microwave input and output to the cavity. The bare center conductor of the connectors act as a RF dipole antenna to excite electromagnetic modes. The empty space milled in two copper pieces form an actual rectangular cavity when put together. The size of the cavity was $28 \times 2 \times 5 \text{ mm}^3$.

Our cavities turned out to have about $Q_i \approx 14000$ at 4 K, i.e., the maximum loaded quality factor achievable is 14000. If the Q_L is 14000 and the resonant frequency f_r is 8 GHz, the photon lifetime τ would become $\tau = Q_L/f_r = 1.75 \mu\text{s}$. We wanted to have a loaded quality factor as large as possible and to have the antenna overcoupled ($Q_i > Q_e$); the overcoupled cavity is desirable to have maximum transmission not to lose photons inside the cavity. This can be done in principle by gradually increasing the length of the antenna, however, we found that as the antenna starts to stick out of the cavity wall, the internal quality factor decreases, making it hard to get the cavity overcoupled. Therefore, we increased the coupling up to the point where the internal quality factor started to decrease. The cavity came out undercoupled, having $Q_L = 5000$, $Q_i = 8000$, $Q_e = 14000$ and $IL = -9 \text{ dB}$.

4.3.2 Superconducting solenoid

To apply a magnetic field perpendicular to the samples, we made small superconducting coils. Each coil was placed on the surface of each cavity in such a way that the magnetic field is perpendicular to a substrate. We could have used a configuration for Helmholtz coils to have more uniform field distribution, however, we

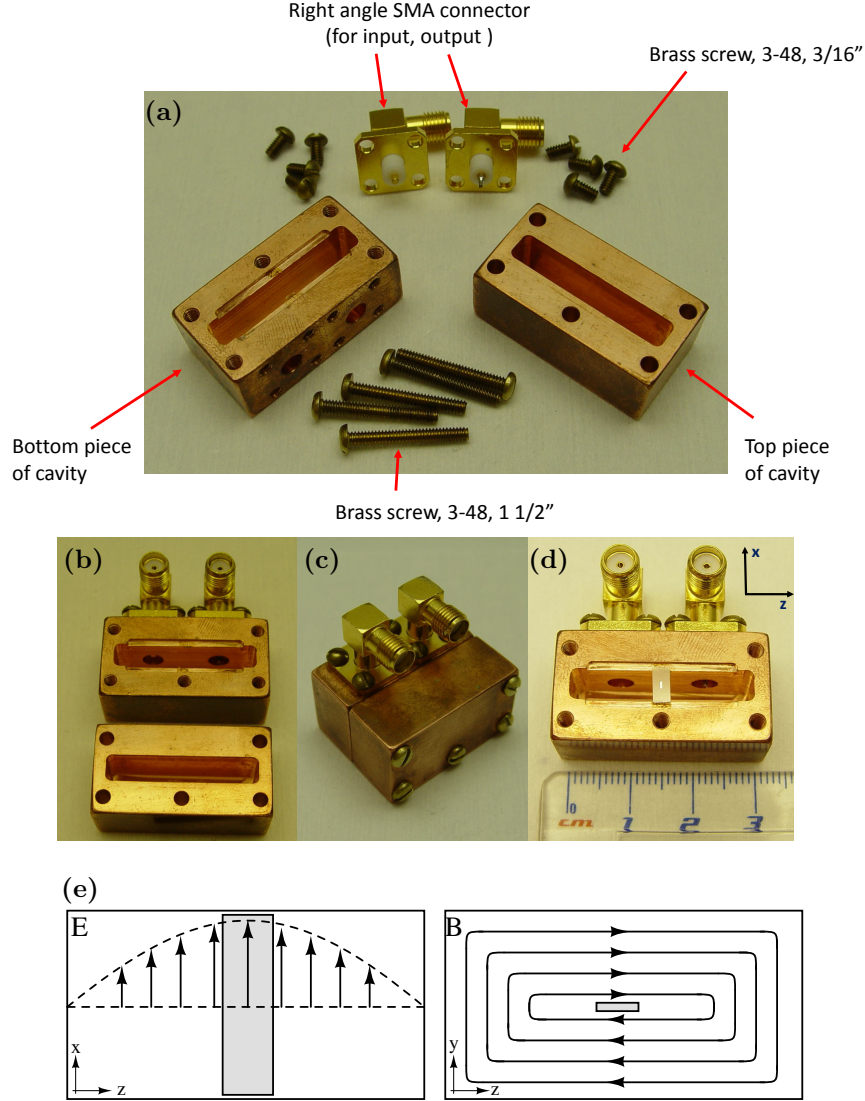


Figure 4.6: (a) Photograph of a disassembled copper cavity. (b) Two pieces of the copper cavity are shown before a sample is placed inside. (c) The cavity is completely assembled. (d) A transmon sample on the sapphire substrate is placed in the groove of the bottom piece of the cavity. On the upper-right corner is a coordinate showing the direction of x and z . (e) The electric (left) and magnetic (right) distributions of TE₀₁₁ mode are schematically drawn. The rectangular shaded boxes represents a substrate. Note the Cartesian coordinate is defined in the same way as in Fig. 4.6(d).

decided to place only one coil due to make setup simpler.

To make a superconducting coil, an OFHC (Oxygen-free high thermal conductivity) copper ⁶ was machined to be a hollow cylinder with two rims on top and bottom of the cylinder (copper bobbin), which serves a mechanical support for superconducting wires. The drawing is shown in Fig. 4.7(b). The copper was chosen to provide good thermalization to superconducting wires, but alternatively Teflon can be also

⁶OFHC copper has higher thermal conductivity than non-OFHC copper at cryogenic temperature.

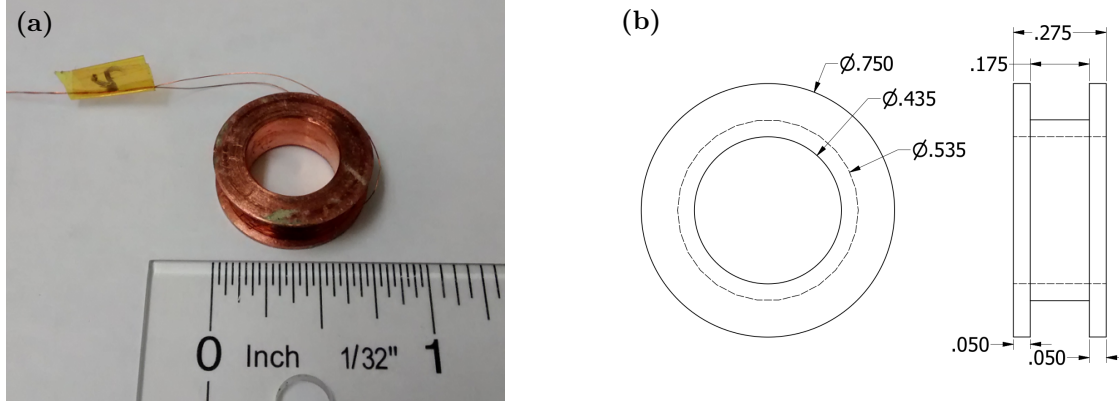


Figure 4.7: (a) A photograph of a superconducting solenoid made of a copper bobbin and NbTi superconducting wire. (b) CAD drawing showing dimensions of the copper bobbin. The unit is inch.

used.

After machining, the copper spool was sonicated in acetone for 3 minutes followed by IPA for 3 minutes to remove machine oil. The copper spool was mounted to a steel ball bearing to turn easily when a superconducting wire was wound around it. The wire (SC-T48B-M-0.1mm, Supercon Inc.) was a copper clad NbTi superconducting wire. It consists of 0.062 mm dia. NbTi, 0.1 mm dia. Cu cladding, and 0.126 mm dia. Formvar insulation. This wire has a critical current of 9 Amp at 3 Tesla at 4.2 K.

Before winding the wire, we applied a thin layer of an epoxy (M-bond 610 Adhesive, Ted Pella) ⁷ to the copper spool that serves an insulating layer between the superconducting wire and the spool ⁸. The wire was slowly wound around the copper spool and the epoxy was applied between several layers. The total number of turns were estimated with Mathematica program in advance for desired maximum magnetic field at the position of samples in the cavity. Since a sample in the cavity is far (about half an inch) away from the center of the solenoid, the magnetic field becomes quite low. Finally, the solenoid was baked on a hot plate at about 150 degree over 6 hours to remove solvent and speed up curing process.

After baking, the resistance of the solenoid was measured with a multimeter and checked to see if there was a short between the wire and copper. We performed the calibration of each solenoid in the following way—measurement of magnetic field strength for given current at the location of a sample in the cavity. A test sample that can show magnetic field dependence was fabricated. In particular, we fabricated a SQUID-type nanowire-loop with RF antenna made of a MoGe superconducting film, and mounted it in the cavity to measure the period of oscillation of transmission below T_c . Based on the period and the area of the loop, we calculated the magnetic field per 1 Amp, i.e., Gauss/A. This conversion factor was later to calculate the actual magnetic field applied to samples.

⁷This non-conductive epoxy works, by mixing two components, in the wide range of temperature (4 K to 643 K).

⁸Without the epoxy layer, a short between the NbTi wire and copper was occasionally found.

4.3.3 Sample mounting and preparation for cool-down

Each transmon qubit was mounted in the center of the copper cavity, where the electric field has antinode (Fig. 4.6(d)). We glued the substrate in the groove of the bottom piece of the cavity, using a little bit of GE varnish (VGE-7031, Lake shore cryogenics) ⁹. After the varnish is applied to the bottom of the substrate, the sample is gently placed in the groove and baked on the hotplate for about 10 minutes at 80-90 degree to quickly dry off the solvent from the varnish. Alternatively, a thermal grease (Apiezon-N) can be used to glue the sample on the groove. Unlike the varnish, it doesn't get dry, and thus can't provide a strong mechanical support on the substrate, especially, in case that a sample is suspended on one side. However, it is sticky enough to hold down a substrate on the cavity groove.

Once the samples are glued in the cavities, they are mounted on the stage of the Faraday cage through two semi-rigid copper cables. It is important to connect the cable to the correct SMA connector on the cavity, if the input and output couplings are not symmetric. If the couplings are not symmetric, the input coupling is normally weaker than the output coupling to increase the signal to noise ratio. If the couplings are nominally symmetric, the order of the copper cables do not matter. Then the superconducting solenoids are placed at the bottom of the cavities and taped with a (yellow) cryogenic tape (Lake shore) or a (brown) kepton tape first. For an additional support, the thin copper wires are wound around the cavity and solenoid together. A photograph of the mounted copper cavities and solenoids is shown in Fig. 4.8(a).

Once two cavities and solenoids were mounted on the stage of the Faraday cage, a series of cans were put on the dilution fridge insert in the order: aluminium Faraday cage, cryogenic Mu-metal shield, still radiation shield, and inner vacuum can (IVC) can. A sequential application of each can is shown in Fig. 4.8(b). All four cans except the IVC are secured in place with brass screws, and the IVC is sealed with a indium wire for vacuum seal. The space in the IVC is pumped by a mechanical roughing pump and later a turbo pump to reach less than low 10^{-4} Torr. It is recommended to perform a helium leak check with a residual gas analyzer (RGA) (RGA100, Stanford Research System). Finally, a small amount of helium gas (~ 5 mL) is injected into the IVC for the purpose of heat exchange gas.

4.3.4 Sample cool-down in dilution fridge

Now the dilution fridge insert including the samples can be cooled down. Since our dilution fridge is a wet-type, i.e., liquid helium is used, the cool-down usually takes two or three days to get to the base temperature and be ready for actual measurement, since lots of pumping and leak-check are required. An overview of

⁹It is advised to use this varnish in the fumehood as it emits strong smell. It has relatively good thermal conductivity at cryogenic temperature and an insulator electrically. The varnish can be very viscous and sticky when dry, so in that case, a little amount of acetone can be added to dilute it.

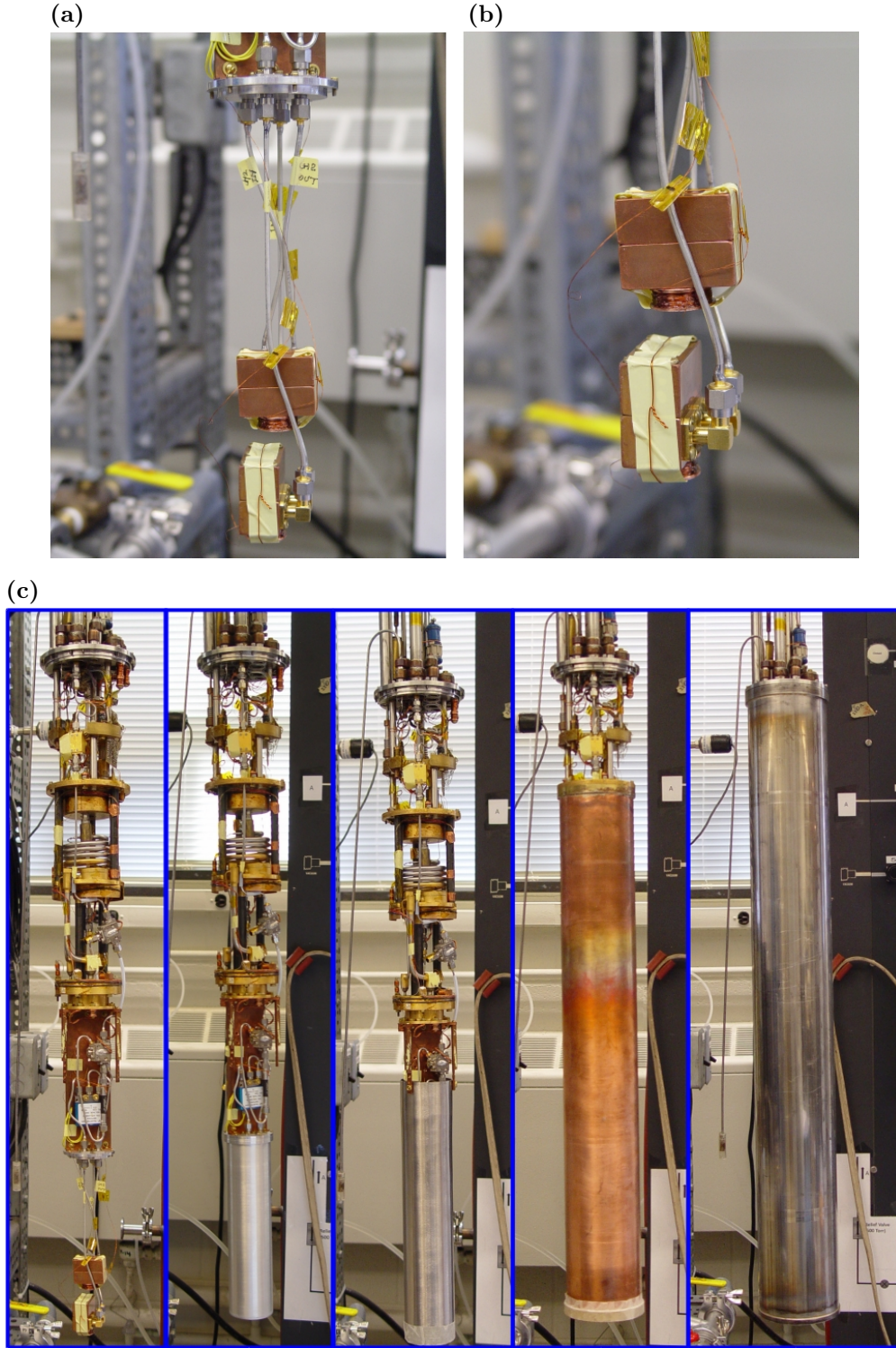


Figure 4.8: (a) Two copper cavities are mounted to the top flange of aluminium Faraday cage via copper semi-rigid cables. Also two superconducting solenoids are attached to the bottom side of the cavities using a cryogenic tape and copper wire. (b) Close-up of the cavities in (a). (c) A series of photos showing each mounting step of aluminium Faraday cage, cryogenic Mu-metal shield, (copper) still radiation shield, and inner vacuum can (IVC).

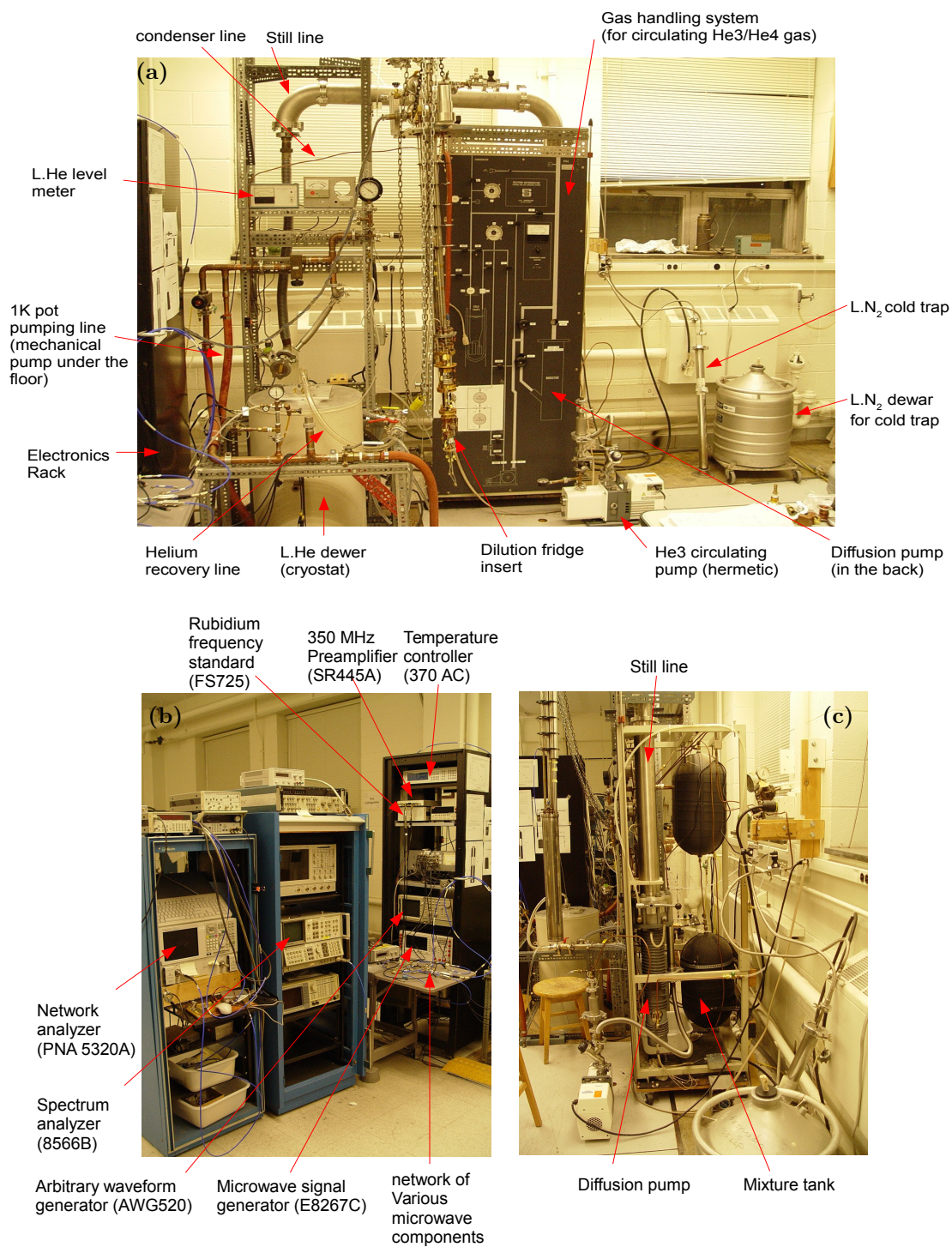


Figure 4.9: (a) A photograph of dilution refrigerator system. (b) A photograph of Room-temperature electronics. (c) A side view of the gas handling system .

the dilution fridge system is shown in Fig. 4.9(a) and 4.9(c). The system consists of a multiple parts mainly: dilution fridge insert, gas handling system, liquid helium cryostat, cold trap, and three pumps (He3 pump, 1K pot pump and diffusion pump). We intend to briefly describe how the dilution fridge is cooled down, as detailed procedures should be referred from the operational manual [56].

Now that the dilution fridge insert is ready for cool-down, it is slowly lowered into the cryostat. It is assumed that the cryostat is at room-temperature and empty. It is important to make sure an oring between the dilution fridge insert and the top flange of the cryostat is in the right place (in the groove) for perfect seal, otherwise, there might be a leak that leads to loss of lots of evaporated helium gas without recovery.

Next, the condenser/still lines from the gas handling system are connected to the dilution fridge insert, and those two lines (and some part of the gas handling system) need to be pumped down to less than an order of tens mTorr. It is advised to do leak test around valves and joints. All those pipelines are the passage where He3 and He4 mixture travels, so there should be absolutely no leak, otherwise, some of mixture would leak out and air entering the circulation path would make the condenser line clogged.

After the pumping is finished, liquid nitrogen is transferred into the cryostat for precooling. The cryostat needs to be pumped to remove air out before transferring liquid nitrogen. Then the cryostat is vented with nitrogen gas. Here one additional step is to pump out 1K pot line and keep flowing helium gas through 1K pot line (there is no needle valve in the 1K pot controlling the flow-in of liquid helium.) This is important to avoid 1K pot tubing being clogged just in case.

Once liquid nitrogen is transferred, then the cryostat and insert are left for a few hours for temperature inside the insert to reach 77 K. Next, the liquid nitrogen is back-transferred to a nitrogen dewar and the cryostat is pumped again to get rid of all nitrogen (both gas and liquid). The cryostat is vented with helium gas to 1 atm, and liquid helium can be transferred.

Now that the dilution fridge insert reaches 4.2 K, the helium exchange gas must be completely removed from the IVC. This is done by pumping the IVC and heating the 1K pot and still part by apply a current to two heaters mounted on them. This *bakeout* process helps helium gases quickly released from the surface of structures inside the IVC. After about 3 hours of the bakeout, the mixture should be condensed by the 1K pot; the 1K pot is continuously pumped by the 1K pot pump and kept at about 1.5 K. The condensing process is followed by circulation process of the mixture. Initially, the hermetic He3 pump circulates the mixture and when appropriate, the diffusion pump is operated to boost the circulation rate, leading to the base temperature.

Normally, the base temperature is quite stable over a long period of time, and only maintenance required would be to refill liquid helium in the cryostat and liquid nitrogen for the cold trap. Also, the pressures

in the condenser and still line of the gas handling system should be checked regularly to spot any unusual behavior.

Chapter 5

Frequency-domain measurement of Meissner qubit

In this chapter, we will present the results of frequency-domain measurements of the Meissner qubit. We will mainly present two representative samples, called N1 and N7, throughout current and next chapter. Before we move on to the first section, we present a quick summary of how the Meissner qubits were fabricated, what parameters they had, and how they were measured.

The Meissner qubits were fabricated on a c-plane sapphire using a novel modification of the double-angle evaporation technique, now achieved in ultra-high vacuum in a molecular beam epitaxy (MBE) growth system. The device design is shown in Fig. 3.1(d). The patterns were defined by electron beam lithography on the bi-layer of MMA EL-13 and ZEP 520 A7 in eLine Raith system, and after development the exposed surface was cleaned to remove MMA residue by both dry and wet etching—oxygen plasma by RIE (reactive-ion etching) and BOE (buffered oxide etch). The first and second layers of aluminium films, each with 45 nm thickness were deposited with background base pressure of 10^{-11} Torr. The oxide layer was formed by an exposure to Ar/O₂ mixture (10% O₂) under the proper conditions of pressure and time calibrated for critical current density of the JJs. Each large rectangle [marked A1 and A2 in Fig. 3.1(b)] acts as a radio-frequency (RF) antenna and has dimension of $250 \times 500 \mu\text{m}^2$. The spacing between the nearest edges of the antennas is $25 \mu\text{m}$ [Fig. 3.1(b)]. The antennas are bridged by two Al thin-film rectangles [called “electrodes” and marked E1 and E2 in Fig. 3.1(c)] and two JJs, connecting the electrodes and forming a SQUID-like loop [Figs. 3.1(c), 3.1(d)].

We will discuss two representative devices denoted by N1 and N7. The qubit transition frequency f_{01} of N1 at zero magnetic field was 6.583 GHz, the Josephson energy of both junctions taken together was $E_J^{\text{max}}=19.4$ GHz, the corresponding net critical current was 41 nA, and the Coulomb charging energy—mostly associated with the electric capacitance between the antennas—was $E_C=0.307$ GHz. Thus the ratio of the two energy scales was $E_J^{\text{max}}/E_C=63.2$ for device N1. For the qubit N7 the same type of parameters were $f_{01}=4.970$ GHz, $E_J^{\text{max}}=11.1$ GHz, the corresponding critical current at zero field was 23.4 nA, $E_C=0.318$ GHz, and $E_J^{\text{max}}/E_C=34.9$.

Each device was mounted in a 3D rectangular copper cavity with the dimension $28 \times 22 \times 5 \text{ mm}^3$

[Fig. 3.1(a)]. The qubits were coupled to electromagnetic cavity modes and in turn the cavity was used for qubit readout. The samples were positioned in the center of the cavity where the dipole coupling of the fundamental mode to the qubit is maximized, i.e., at the electric field anti-node. The TE_{011} mode of the empty cavity occurred at 8.679 GHz with the internal (unloaded) quality factor $Q_i=8000$, external quality factor $Q_e=14000$, and loaded ("experimental") quality factor $Q_L=5000$ ¹. An asymmetric coupling (larger at output) was used to maximize the signal to noise ratio. Although the smaller input coupling increases the signal-to-noise ratio, it should not be too small since otherwise the spectroscopic power at the input port of the cavity required to drive a qubit would be unattainably high beyond the possible output power of a microwave source. The bare cavity mode f_c at TE_{011} for sample N1(N7) was 8.403 GHz (8.435 GHz), and the coupling strength $g/2\pi$ was approximately 130 MHz for both samples. The bare cavity frequency f_c is the resonant frequency of the cavity without dispersive shift. It is the cavity frequency at large drive power where the cavity reaches the state of a near-unity transmission. f_c does not depend on the qubit transition frequency and state. A coupling strength g was calculated by $g^2/\delta = |\omega_c - \omega_0|$, where $\delta = |\omega_c - \omega_q|$ is qubit-cavity detuning, ω_c is a bare cavity frequency, and ω_q is a qubit transition frequency. ω_0 is a resonant frequency measured at low microwave power [26].

The cavity was mounted in a $^3\text{He}/^4\text{He}$ dilution refrigerator (S.H.E. Corp.) with the base temperature of 45 mK. The cavity was enclosed in a cylindrical aluminium Faraday cage, whose inner walls were coated with black infrared-absorbing material [54]. The Al cage is intended to prevent external stray photons from reaching the sample. The Al cage helps also to protect the sample from the influence of external stray magnetic fields, thanks to the Meissner effect. A cylindrical cryogenic μ -metal (Amuneal) cylinder was placed concentrically around the Al cage for additional magnetic shielding. The magnetic field was applied perpendicular to the substrate from an external home-made superconducting solenoid attached at the bottom of the copper cavity, i.e. inside the Al cage and the μ -metal shield.

For microwave transmission measurement, the input and output transmission lines were connected in series with a chain of cryogenic microwave components, including attenuators, isolators (PAMTEQ), a commercial low-noise HEMT (high-electron-mobility transistor) amplifier (Low Noise Factory, LNF-LNC6-20A) and low-pass filters. For noise filtering, commercial low-pass filters (K&L Microwave, 6L250-12000) and home-made stainless steel powder filters (3 dB at cutoff ≈ 8.5 GHz) were inserted in both input and output of the copper cavity.

The measurements were performed using the circuit QED technique in high-power regime [26, 57]. For

¹ Q_e was set by adjusting the length of the center pins of SMA connectors in the cavity. Q_e can be calculated, given measured internal quality factor (Q_i), loaded quality factor (Q_L) and insertion loss (IL) in the following expression: $1/Q_L = 1/Q_e + 1/Q_i$, $IL(\text{dB}) = 20 \log[Q_i/(Q_i + Q_e)]$

the spectroscopy and qubit readout, RF square pulses were created, added together and fed into the cavity. The pulses were shaped by mixing a continuous microwave tone (Agilent E8267C or HP 8341B) and a square voltage pulse from an arbitrary waveform generator (Tektronix AWG520) using pairs of rf mixers (Markis, M8-0420). The transmitted readout signal was down-converted to 25 MHz intermediate frequency (IF) signal by heterodyne demodulation, and the IF signal was acquired to read the amplitude by a high-speed digitizer (Agilent, U1082A-001). For qubit state readout, we adjusted the power of readout pulse (a few μs long) to maximize the contrast in transmitted microwave amplitude for the ground and first excited states.

5.1 Transmission measurement of cavity-qubit system

In superconducting qubit measurements in cQED architecture, the cavity or resonator serves as a detector to measure the qubit. Normally, the first thing to do is to measure the transmission of the cavity as a function of the drive frequency—the drive frequency is the frequency of input microwave to the cavity. Thus, we performed the transmission measurement of the cavity-qubit system first. Here in fact we mean by the transmission the voltage amplitude of the transmitted microwave at the output of a cavity (we will call this voltage amplitude “heterodyne voltage (V_H)” in the text since the amplitude of the transmitted microwave is measured by heterodyne technique in Sec. 4.2.2. Thus, the transmission becomes proportional to the voltage amplitude of microwave at the input of the cavity. The transmission was measured by sending a microwave pulse to the cavity and receiving the transmitted microwave pulse. The transmitted microwave pulse was then demodulated to get the microwave amplitude, which is denoted as V_H .

We show a representative plot of the transmission in log scale versus drive frequency at various input microwave powers P_r in Fig. 5.1. Each curve was measured at different microwave powers in dBm unit. First, we look at the low power case. All the measurements of the Meissner qubit were performed in the dispersive regime of the cQED scheme, i.e., qubit-cavity detuning $|\Delta| = |\omega_q - \omega_r| \gg g$. Therefore, when there are sufficiently small number of photons involved in the measurement, i.e., $N < N_{\text{crit}}$ in Sec. 2.3.2, we expect to see the cavity (resonant) frequency shifted by $g^2/|\Delta|$. It can be seen in Fig. 5.2 that there is a resonant peak at about 8.456 GHz measured at $P_r = -50$ dBm in the transmission versus drive frequency. The bare cavity frequency ² is at ~ 8.432 GHz as indicated by the resonant peak at the highest power $P_r = 4$ dBm, and is shifted by $g^2/|\Delta| = 24$ MHz due to qubit-cavity interaction. Therefore, this allows us to measure the coupling strength g once the detuning or qubit transition frequency is known from qubit spectroscopy.

²This is the cavity frequency without dispersive shift.

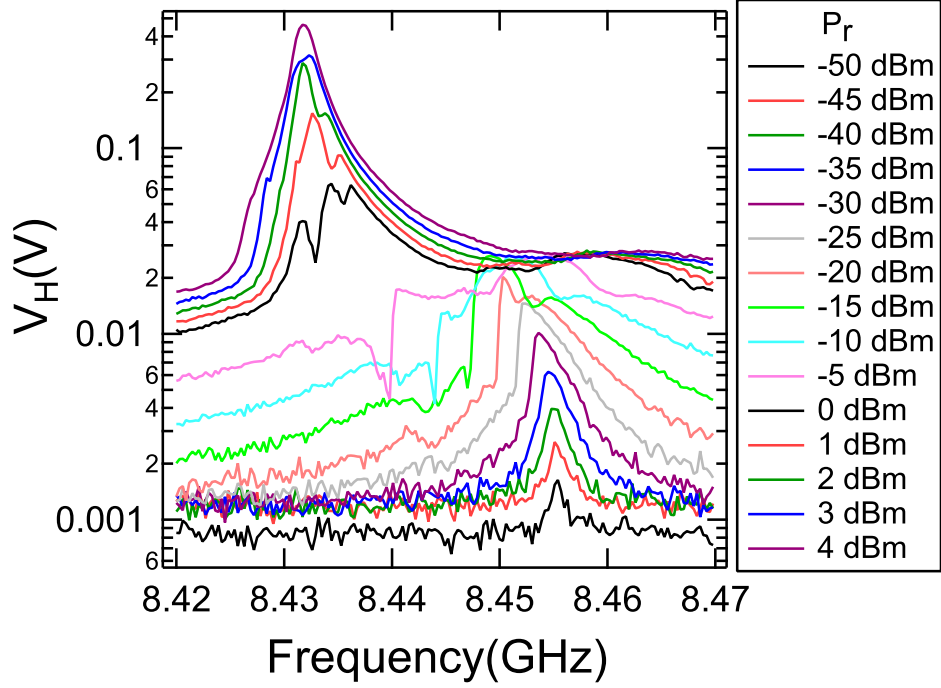


Figure 5.1: Transmission (heterodyne voltage V_H) versus drive frequency is depicted in semi-log plot at various microwave powers ranging from -50 dBm to 4 dBm. The peak at $P_r = 50$ dBm is dispersively shifted from the bare cavity frequency $f_c \sim 8.432$ GHz by $g^2/|\Delta|$, where Δ is the qubit-cavity detuning, $\Delta = \omega_{01} - \omega_c$. For this sample (N1), $g/(2\pi) \approx 130$ MHz.

5.2 Calibrating drive power: high-power measurement

In measuring the Meissner qubit in the copper cavity, we decided to use high-power measurement technique rather than the conventional cQED technique in a single-photon regime. There were a couple of reasons for choosing the former. First, the transmission of the copper cavity was lower than unity since the cavity was under-coupled, i.e. internal quality factor Q_i is smaller than external quality factor Q_e , $Q_i > Q_e$. The low transmission implies that the signal to noise ratio is small, so that heavy averaging for a long time is necessary. Second, since we had to measure the qubit as a function of magnetic field, we wanted to avoid changing the drive frequency; the drive frequency should be set at the dispersively shifted cavity frequency, which varies as the qubit transition frequency does. In the high-power measurement, the drive frequency can be fixed at the bare cavity frequency.

To see how the high-power measurement works, we show the transmission measured as a function of drive frequency and power first when the qubit is in the ground state in Fig. 5.2(a). At low microwave power, there is a single resonant peak at around 8.455 GHz. As the power increases, the qubit-cavity system becomes nonlinear and thus the transmission is no longer Lorentzian. Above a few dBm, the bright state

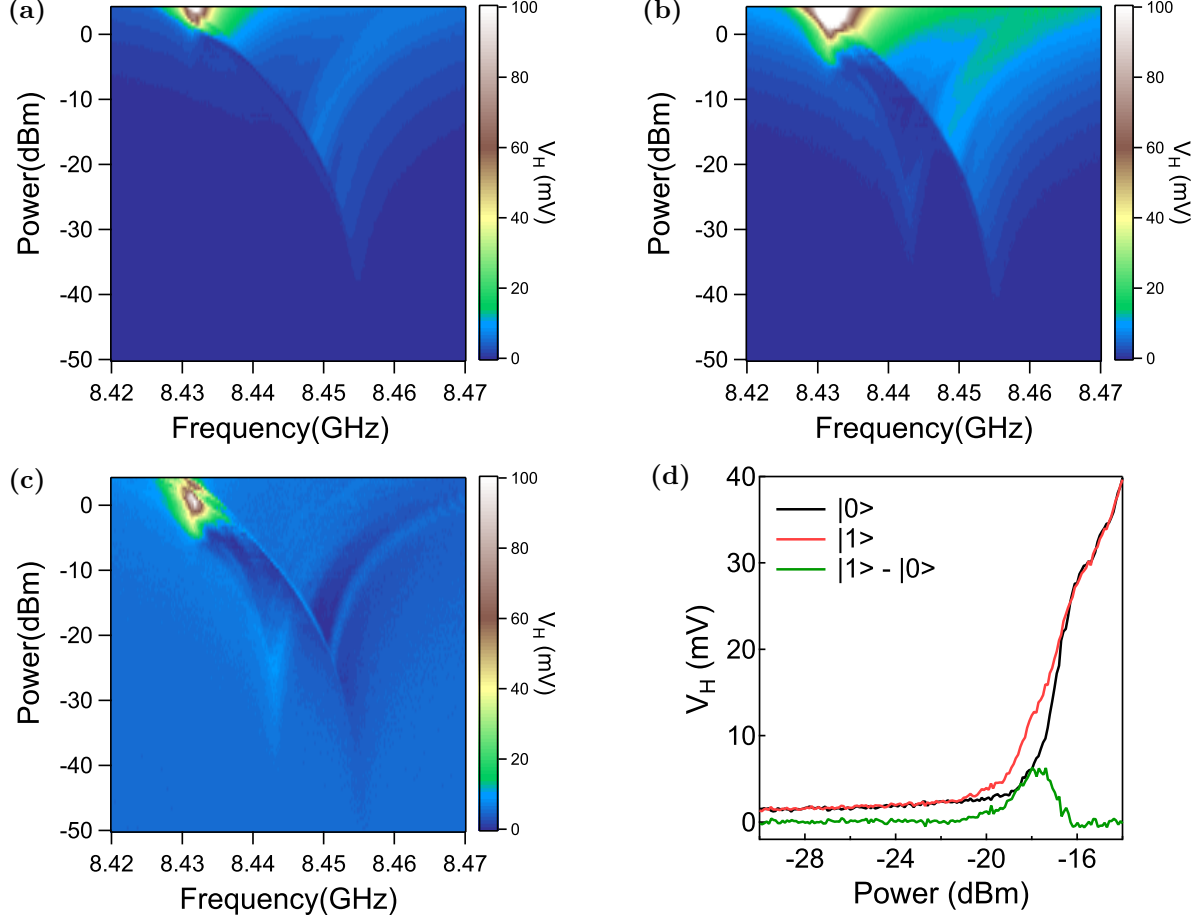


Figure 5.2: The transmission (V_H) is plotted as a function of drive frequency and microwave power when the qubit is in the ground state (a), and the mixture of both the ground and first excited state (b) for sample N1. The difference in transmission between (a) and (b) is depicted in (c). (d) A representative plot of the transmission versus drive power at the bare cavity frequency is shown for the ground state, the first excited state, and the difference between them. The maximum contrast between the ground and first excited state occurs at around -18 dBm. Also, note that the onset power of the first excited state where the transmission starts to increase steeply is lower than that of the ground state due to the asymmetry of the dispersive shift.

emerges at around 8.432 GHz, which corresponds to the bare cavity frequency, i.e., frequency without a dispersive shift. Meanwhile, the same plot was created when the qubit was in the equally mixed state of ground and first excited states [Fig. 5.2(a)]. To excite the qubit, first we performed the spectroscopy to find the qubit transition frequency and applied a saturation pulse³, which should be long enough to produce a 50/50 mixed state. The first thing to note would be that there are two resonant peaks at 8.443 GHz and 8.455 GHz. The left one is the dispersive shift corresponding to the first excited state, and the right one is the same shift seen in Fig. 5.2(a). The second thing to note is that the bright spot emerges at a slightly

³A saturation pulse is a microwave pulse which is long enough for Rabi oscillation to die out. Thus the resulting qubit state will be statistically equal ensemble of the ground and first excited state.

lower drive power. This indicates that the onset for the excited state power where the transmission at the bare cavity frequency starts to increase abruptly is lower than that of the ground state. It is the different onset power that gives contrast in transmission between the ground and excited states. The different in transmission can be better seen in Fig. 5.2(c), where the transmission difference is calculated by subtracting the ground state data from the excited state data. We can see the maximum difference in transmission occurs at the bare cavity frequency and at around 0 dBm, which is just below the bright spot for the ground state. Since this transmission is very high, we can have high-fidelity qubit measurement. In practice, to find the optimal power which gives the best contrast in transmission between two states, we can drive the cavity at the bare cavity frequency, and measure the transmission as the power is swept. A representative plot is shown in Fig. 5.2(d).

5.3 Spectroscopy

The spectroscopy of a qubit is the process to measure the transition frequencies of a qubit between each energy level. In the cQED architecture, such spectroscopy can be normally carried out by monitoring the transmission at the resonant frequency as the second microwave signal to excite the qubit is swept. Because of the state-dependent dispersive shift, the transmission should change when the spectroscopic microwave frequency matches the qubit transition frequency.

In the case of the Meissner qubit or transmon, in a single photon regime (low drive power regime), the drive frequency is set at the dispersively-shifted resonant frequency $\omega_d = \omega_c + g^2/|\Delta|$, where the $+$ sign is due to the condition $\omega_{01} < \omega_c$. As the spectroscopic frequency ω_s (second microwave signal) is swept, the transmission shows dips when the excitation frequency matches with a transition frequency, for example, $\omega_s = \omega_{01}$. Such dips occur due to the state-dependant dispersive shift of the resonant frequency as shown in Fig. 5.3(a), for example. Two data set were measured at different spectroscopy powers. The red data was shifted up by 1 mV for clarity. The transmission stays constant until the spectroscopic frequency matches qubit transition frequencies. The dip at 7.55 GHz corresponds to the qubit transition ω_{01} from the ground to the first excited state for both powers. Meanwhile, in the case of higher spectroscopic power, there shows another dip at around 7.43 GHz. It corresponds to multiphoton transition from the ground to second excited state by two-photon process, so that $\omega_{02}/2 = 7.43$ GHz and thus $\omega_{02} = 14.86$ GHz. From the obtained spectrum, ω_{12} can be computed by $\omega_{12} = \omega_{02} - \omega_{01} = 7.31$ GHz, thus the anharmonicity α is $\alpha = \omega_{12} - \omega_{01} = -240$ MHz. Also, we note that the width of the dip—linewidth—become wider at higher spectroscopic power. The half width at half maximum (HWHM) depends on the spectroscopic power and it

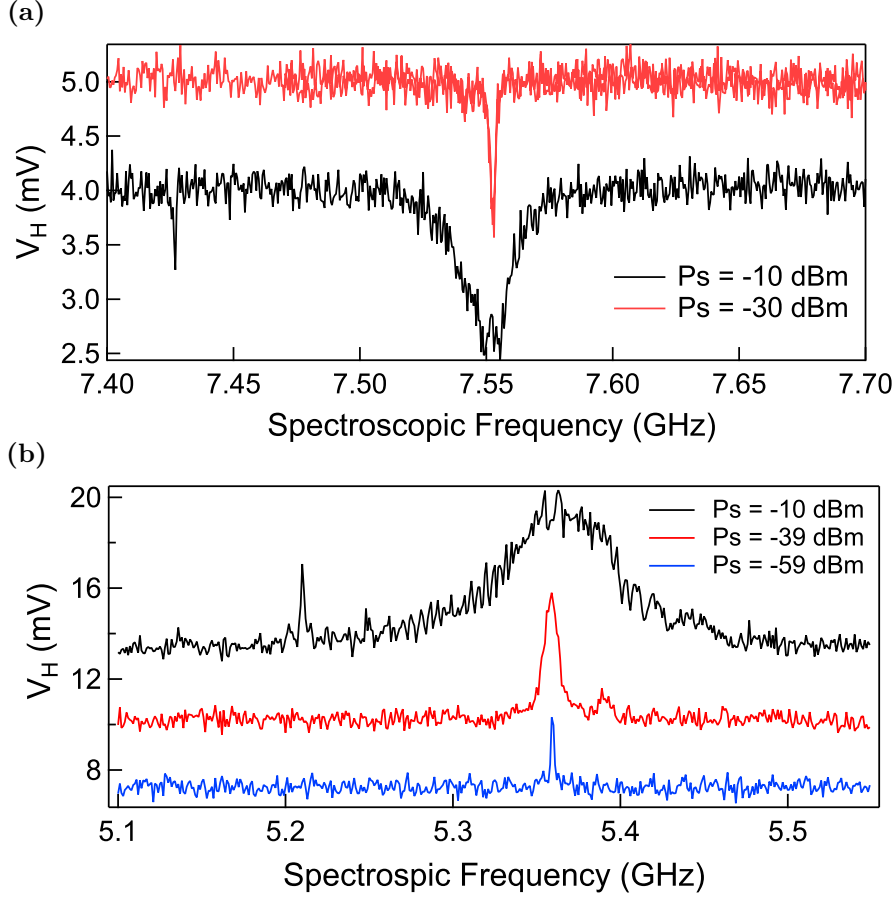


Figure 5.3: (a) A representative plot of the heterodyne voltage versus spectroscopic frequency for spectroscopy of a transmon in low readout power regime. The drive frequency was set to be the resonant frequency of the cavity, i.e., the dispersively shifted cavity frequency when the qubit is in the ground state. Two curves were measured at two different drive powers (-30 and -10 dBm) as indicated by the figure legend. The red curve is shifted by 1 mV for clarity. The dips at 7.55 GHz correspond to the qubit transition frequency ω_{01} , and the small dip at 7.425 GHz to the qubit transition ω_{02} , induced by two-photon process such that $\omega_{02}/2\pi = 7.425 \times 2 = 14.85$ GHz. (b) A representative plot of the heterodyne voltage versus spectroscopic frequency in high readout power regime [different sample from (a)]. The drive frequency was set to the bare cavity frequency. Note that the transmission is higher when the qubit is in the first excited state than in the ground state; the reason why the peaks appear, not dips. Like in (a), the peaks at 5.352 GHz correspond to the qubit transition frequency ω_{01} , while the small peak at 5.21 GHz to the transition ω_{02} by two-photon process.

may be expressed in the following expression [46],

$$2\pi\delta\nu_{\text{HWHM}} = \sqrt{\left(\frac{1}{T_2}\right)^2 + 4g^2n_s\left(\frac{T_1}{T_2}\right)}, \quad (5.1)$$

where $2\pi\delta\nu_{\text{HWHM}}$ is the half width at half maximum of the line, T_1 the relaxation time, T_2 the dephasing time, n_s the number of the spectroscopic photons, and g the qubit-cavity coupling strength. This equation illustrates that as the spectroscopic power increases, the linewidth increases accordingly. Also, in the limit

of the low power ($n_s \rightarrow 0$), the HWHM approaches $1/T_2$, which allows us to estimate the dephasing time T_2 without time-domain measurement.

Meanwhile, in the case of high-power measurement, the spectroscopy can be done in the same way as the case of the low drive power. First, the drive frequency is set at the bare cavity frequency—cavity frequency without dispersive, not the cavity frequency which is dispersively shifted by the qubit. Second, the drive power should be chosen so that the transmission depends on the qubit state. This power may be set to “onset” power. The onset power is the drive power where the transmission starts to increase abruptly, when the drive power is swept from low to high power as shown in Fig. 5.2(d). The found onset power is not optimum drive power that gives the best contrast of the transmission between the ground and the first excited state, but it should be good enough to find the qubit transition frequency ω_{01} . Once the ω_{01} is found, then the drive power can be calibrated (see Sec 5.2) and the spectroscopy procedure can be repeated. A representative plot of the spectroscopy in drive high power regime is depicted in Fig. 5.3(b). Three curves represent the transmission versus excitation frequency with three different spectroscopic power P_s . The peaks at ~ 5.352 GHz are the qubit transition ω_{01} and the small peak at ~ 5.2 GHz for P_s dBm is the 0-to-2 transition by two-photon process.

It is worth mentioning why we decided to use the high-power measurement rather than the low power measurement in measuring the Meissner qubits. First, the transmission level was quite low and thus the signal to noise ratio was so small as to require long averaging. The low transmission was partly due to the undercoupled copper cavity. Second, one advantage of the high-power measurement over the low power measurement is that the bare cavity frequency can be used for the drive frequency, irrespective of the qubit transition frequency. If we would have used the low power measurement, we should have found the qubit transition frequency whenever it was changed, as we studied the magnetic field dependence of the Meissner qubit. However, time to time we had to recalibrate the driver power to find the optimal values.

5.4 Magnetic field dependence of transmission

In this section, we investigate the magnetic field dependence of the qubits, anticipating to observe periodic oscillations. In Fig. 5.4, we show the transmission versus applied magnetic field measured with low drive power $P_r = -40$ dBm. The drive frequency for readout was 8.4125 GHz, which is dispersively shifted from the bare cavity frequency 8.403 GHz. The dispersive shift is $g^2/|\Delta| = g^2/|\omega_{01} - \omega_c|$, where $\omega_{01} < \omega_c$ for the sample measured. The periodic oscillation is attributed to the periodic change of the qubit transition frequency, which leads to the periodic change of the dispersive shift. As the magnetic field increases from

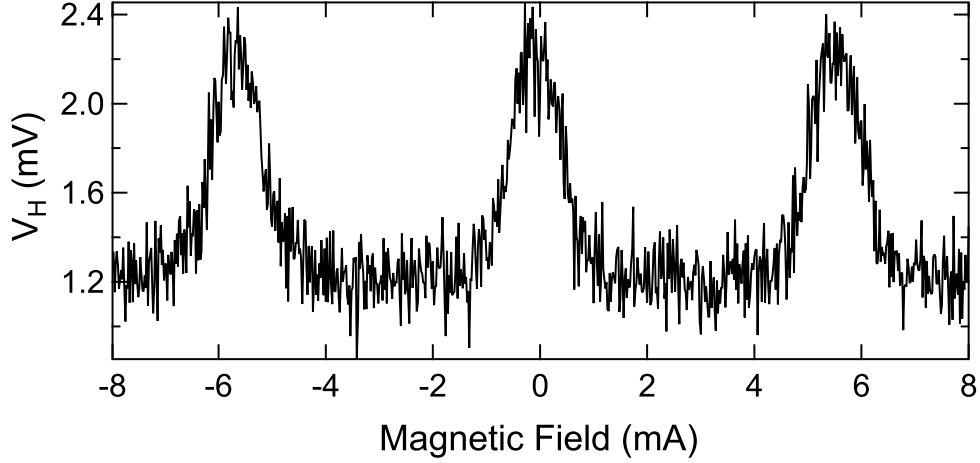


Figure 5.4: The magnetic field dependence of the transmission (V_H), illustrating the periodic oscillation of the qubit transition frequency. The transmission was measured at the cavity resonant frequency 8.4125 GHz in low drive power regime., which is dispersively shifted from the bare cavity frequency 8.403 GHz. As the magnetic field increases from zero, the transmission drops off since the cavity resonant frequency shifts to lower frequency as the qubit-cavity detuning increases.

zero, the qubit frequency decreases ($|\Delta|$ goes up) and thus the cavity resonant frequency ($\omega_r = \omega_c + g^2/|\Delta|$) also decrease leading to the reduction of the transmission.

Now we switch to the high power measurement. The transmission (heterodyne voltage V_H at the bare cavity frequency versus the magnetic field varied is shown for sample N7 in Fig. 5.5. During its measurement the qubit remains in its ground state. The cavity input power is chosen such that the transmission of the cavity is the most sensitive to the qubit transition from the ground to the excited state, i.e., to maximize the contrast as explained in Sec. 5.2. Four segments in different color represent four separate measurement runs. The magnetic field was swept round-trip (forward and then backward) in the first three segments (black, red and green), but one-way (forward) in the last segment (blue). The modulation of the transmission at low B -field arises from the change of the onset power—microwave power at which the cavity starts to show sharp increase in transmission called “bright state” (near-unity transmission) in Ref. [57]. The onset power depends on the qubit-cavity detuning $\Delta = \omega_{01} - \omega_c$ —difference between the qubit transition frequency (ω_{01}) and bare cavity frequency (ω_c). ω_{01} is modulated periodically by the applied magnetic field, because the Meissner qubit is based on a SQUID loop. Thus, as magnetic field was increased, we observed periodic or quasi-periodic heterodyne voltage oscillation (HV-oscillation). The voltage changes reproducibly and periodically as a function of the external magnetic field, up to a field of about 1.6 Gauss. This is the critical field for the vortex penetration. Below this critical field the transmission stays periodic and perfectly reproducible. The corresponding period, ΔB , can be defined as the distance between the adjacent maxima, as is illustrated

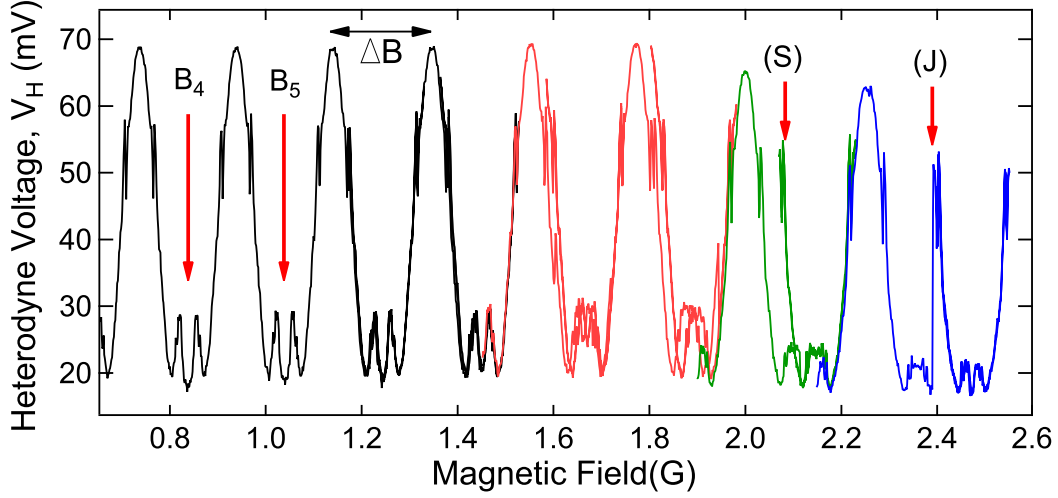


Figure 5.5: (a) Periodic heterodyne voltage oscillation (“HV-oscillation”) as a function of magnetic field. Four different colors represent the separate measurement runs where the magnetic field swept either round-trip or one-way. ΔB shows the period of the modulation. The arrows marked B_4 and B_5 indicate the positions of two adjacent sweet spots, characterized by $df_{01}/dB=0$. Each sweet spot is equivalent to $B=0$ state. The actual $B=0$ sweet spot is outside the range of the plot. The mark “S” indicates the field at which the periodic signal was shifted to the right, revealing some hysteresis caused by vortex entrance to the electrodes. This hysteretic behavior can be seen in the second (red) segment of the B-field sweep ranging from about 1.45 to 2 Gauss. The mark “J” shows the moment when a vortex (or a small group of vortices) entered the electrodes during the forward-sweeping magnetic field.

in Fig. 5.5 by the horizontal arrow. Equivalently, the period can be defined as the separation between the so-called *sweet spots*. Some of these sweet spots, namely B_4 and B_5 , are indicated by the vertical arrows in Fig. 5.5. The sweet spots are the points equivalent to zero magnetic field. Usually the sweet spots occur periodically because the critical current of the SQUID loop changes periodically with magnetic field. If the device is tuned to a sweet spot then it is insensitive, in first order, to the flux noise, because $df_{01}/dB=0$ [see Fig. 5.8(a)] and $dV_H/dB=0$ (see Fig. 5.5).

In the second segment in red, the transmission shows hysteresis behavior as if there is a certain offset magnetic field. Our sample design is such that the phase gradient created by vortices entering the electrodes couples to the SQUID loop. Therefore the exact periodicity of the sweet spots is broken when vortices begin to penetrate. At higher magnetic fields (B-fields), however, abrupt jumps in the transmission [marked as “J”] appear, leading to a shifting of the periodic signal as clearly seen at the position marked “S” in Fig. 5.5. Such behavior indicates vortex entrance into the electrodes (we will discuss this in the following sections), making the hysteretic transmission.

5.5 Periodicity of qubit frequency oscillation

In our qubits, the effective Josephson energy is modulated by the external magnetic field, but the period is set differently as compared to a SQUID-type device [58]. Unlike in usual SQUIDs, the modulation of the total critical current of two JJs in the present case is driven mostly by the Meissner currents in the electrodes, and to a much lesser extent by the magnetic flux through the SQUID loop. This is why the observed period is much smaller than for an ordinary split-junction transmon and the sensitivity of the qubit energy to the external field is higher (See Table 5.1). Thus we achieved an effective amplification of the sensitivity of the qubit to the magnetic field. Note in Table 5.1 that the experimental period (ΔB) is much smaller than the period computed using the area of the superconducting loop (ΔB_{YZ}).

One can understand this new period by considering the phase constraint [59, 60]:

$$\theta_1 - \theta_2 + 2\delta(B) = 2\pi n_v, \quad (5.2)$$

where $\theta_{1,2}$ is the gauge-invariant phase difference across each JJ, n_v the vorticity, $\delta(B)$ the phase difference generated in the thin-film electrodes by the Meissner currents and defined as the phase difference from the entrance point of one JJ “bridge” to the entrance into the other JJ bridge. Each phase difference is depicted in Fig. 5.6(a). The accumulation along the dashed line in Fig. 5.6(a) should be multiples of 2π . Since the current-phase relationship of JJs is single-valued, $n_v = 0$ for our SQUID-type devices, just like in the usual SQUIDs. The field-dependent phase accumulation $\delta(B) = \int \nabla \varphi(B) \cdot d\vec{l}$ where $\Delta \varphi(B)$ is the phase of the order parameter, originates from the Meissner (screening) current in the *electrodes*, induced by the applied magnetic field. Thus we have dubbed our qubit as “Meissner transmon”. Following the Ref. [60], the magnetic period can be estimated as

$$\Delta B = \left[\left(\frac{\Phi_0}{cXZ} \right)^{-1} + \left(\frac{\Phi_0}{YZ} \right)^{-1} \right]^{-1}, \quad (5.3)$$

Table 5.1: Comparison of the experimental and theoretical periods for five samples. ΔB is the measured period of oscillation. ΔB_{YZ} , ΔB_{YZ+cXZ} , and $\Delta B_{kYZ+cXZ}$ are the theoretical periods calculated using three different effective areas denoted by the subscripts.

Sample	X (μm)	Y (μm)	Z (μm)	ΔB (G)	ΔB_{YZ} (G)	ΔB_{YZ+cXZ} (G)	$\Delta B_{kYZ+cXZ}$ (G)
N1	10	1	5	0.38	4	0.49	0.30
N2	10	2	5	0.3	2	0.43	0.29
N3	15	1	5	0.43	4	0.34	0.22
N6	10	2	8	0.16	2.5	0.30	0.19
N7	10	2	8	0.2	1.25	0.27	0.18

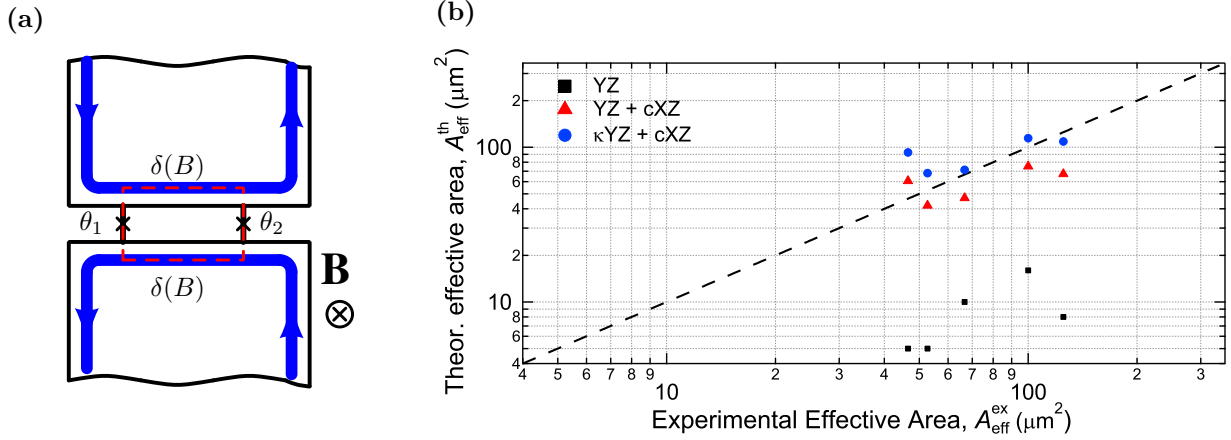


Figure 5.6: (a) A diagram that near both electrodes illustrates the phase constraint [Eq. (5.2)]. The blue thick arrow lines represent the Meissner currents. The red dashed line is the path along which the phase gradient is integrated clockwise. θ_1 and θ_2 are gauge-invariant phase difference across the JJs. The magnetic field is assumed to be into the page. (b) Comparison of theoretical ($A_{\text{eff}}^{\text{th}}$) and experimental ($A_{\text{eff}}^{\text{ex}}$) effective areas of five samples. The dashed line depicts the ideal case of $A_{\text{eff}}^{\text{th}} = A_{\text{eff}}^{\text{ex}}$. See text for the definition of these quantities.

where the numerical coefficient $c = (8/\pi^2) \sum_{n=0}^{\infty} (-1)^n / (2n+1)^2 \approx 0.74$ can be found by solving appropriate boundary problem for the Laplace equation. We cautiously notice that the Eq. (5.3) may not be strictly applicable to our case because it was derived for mesoscopic lead where λ_{\perp} is much larger than X , the width of the electrode. Indeed, we estimate $\lambda_{\perp} \approx 552 \text{ nm} \ll 10 - 15 \mu\text{m}$. Meissner currents are stronger in the case of a relatively small perpendicular magnetic length, and thus this theory still may provide a semi-quantitative estimate.

We emphasize that unlike a regular SQUID the period is not set by the area YZ enclosed by SQUID loop only, but rather by a new effective area $YZ + cXZ$ in Fig. 3.1(d) [59, 60]. To compare those two effective areas, we plotted in Fig. 5.6(b) the measured effective area $A_{\text{eff}}^{\text{ex}}$ versus theoretical effective areas $A_{\text{eff}}^{\text{th}}$ for five samples; those effective areas were calculated by the flux quantum Φ_0 divided by the period of oscillation. The black squares and red triangles represent $A_{\text{eff}}^{\text{th}} = YZ$ and $A_{\text{eff}}^{\text{th}} = YZ + cXZ$, respectively. The effective area of $YZ + cXZ$ matches the data much better than simply the SQUID loop area does. This fact confirms our expectation that the qubit energy is controlled mostly by the Meissner current.

Another possible contribution to the observed amplification of the magnetic sensitivity is the focusing of the magnetic field into the SQUID loop area by the large superconducting film nearby which is also due to the Meissner effect and the relatively small λ_{\perp} . This field focusing effect enhances the magnetic field by a factor of $\kappa = B_1/B_0 > 1$, the ratio of enhanced magnetic field B_1 to applied magnetic field B_0 . Thus the effective area set by the SQUID loop increases by a factor of κ . To incorporate the field focusing effect, we

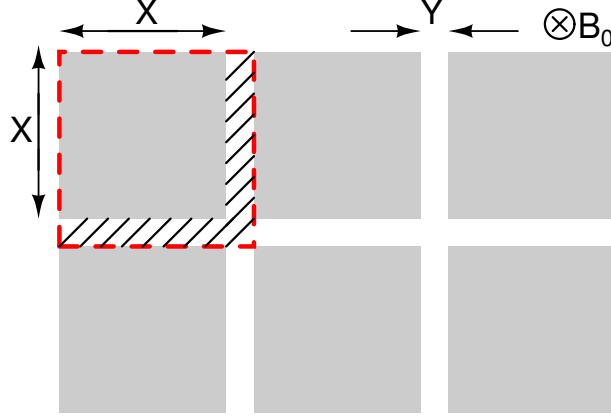


Figure 5.7: An array of square superconducting aluminium films. A magnetic field is applied perpendicular to the surface of the films. The enclosed area by dashed line indicates one unit cell.

replaced YZ with κYZ , thus the equation for the period ΔB is given by

$$\Delta B = \left[\left(\frac{\Phi_0}{cXZ} \right)^{-1} + \left(\frac{\Phi_0}{\kappa YZ} \right)^{-1} \right]^{-1}. \quad (5.4)$$

The result is plotted in Fig. 5.6(b), and shows an improved agreement with experimental data.

Before we close this section, we will show how to calculate κ . Consider a two-dimensional array of square superconducting films with magnetic field B_0 applied perpendicular to the in-plane of the array as shown in Fig. 5.7. The squares represent the electrodes in actual Meissner qubits. We consider a unit cell enclosed by a red dashed line to calculate κ . When the magnetic field B_0 is applied over the unit cell, the magnetic field inside the films is expelled by Meissner effect, and thus the magnetic field (B_1) in the hatched area is enhanced by a factor of $\kappa = B_1/B_0$. κ is calculated in the following way. We denote A_0 to the area of a unit cell and A_1 the hatched area. The magnetic flux in one unit cell is $\Phi = B_0 A_0 = B_1 A_1$, so

$$\kappa = \frac{B_1}{B_0} = \frac{A_0}{A_1} = \frac{(X+Y)^2}{(X+Y)^2 - X^2} = \frac{(X+Y)^2}{Y(2X+Y)} \quad (5.5)$$

We note that $\kappa > 1$, i.e., field focusing effect.

5.6 Magnetic field dependence of Meissner qubit frequency

In this section, we turn to the magnetic field dependence of the qubit transition energy ($\hbar\omega_{01}$). For the spectroscopy, we set the magnetic field for the qubit to be in the sweet spot which is closed to $B = 0$. The sweet spot can be found by measuring transmission as the magnetic field is swept, similarly, as in

Fig. 5.5. Once the qubit is in the sweep spot, then the qubit transition frequency was found in spectroscopy measurement as described in Sec. 5.3. After that, the optimal drive power was chosen by sweeping the drive power for both ground state and 50/50 mixed state. Then, the range of magnetic field and the excitation frequency were set to take data. The qubit was excited with 2 μ s long saturation pulse, which was immediately followed by a few microsecond readout pulse. The excitation frequency was swept up—low to high frequency—with a fixed step size at a fixed magnetic field, and this process was repeated for equally spaced magnetic field. Fig. 5.8(a) shows the 2D color plot of the transmission as a function of the excitation frequency and external magnetic fields. The color represents the heterodyne voltage of the transmission of the cavity. when the excitation frequency matches the qubit transition frequency, the transmission increases (turns brown in the 2D plot), leading to parabola-like trace. It is not hard to expect the change of qubit frequency since the critical current I_c and in turn Josephson energy $E_J = \hbar I_c / (2e)$ oscillates periodically.

The dashed line in Fig. 5.8(b) is a fit to the qubit spectrum with the following fit function:

$$f_{01} = f_0 \sqrt{|\cos(\pi(B - B_0)A_{\text{eff}}/\Phi_0)|}, \quad (5.6)$$

where f_0 , B_0 and A_{eff} are the fitting parameters. In deriving the fitting function, we used the approximate relation for $f_{01} \approx \sqrt{8E_J E_C}/h$ for the high ratio $E_J/E_C \gg 1$, where $E_J = \hbar I_c / (2e)$, and $I_c(B) = 2I_{c1} |\cos(\pi\Phi/\Phi_0)| = 2I_{c1} |\cos(\pi B A_{\text{eff}}/\Phi_0)|$. B_0 and A_{eff} are offset field to account for the residual magnetic field present in the setup, and the effective area, respectively. The best fit values of B_0 and f_0 were -4.5 mG and 6.583 GHz. Particularly, the best fit value of $A_{\text{eff}} = 55.2 \mu\text{m}^2$ was obtained and consistent with the measured $A_{\text{eff}} = 55 \mu\text{m}^2$ determined from the periodic oscillations of Fig. 5.5.

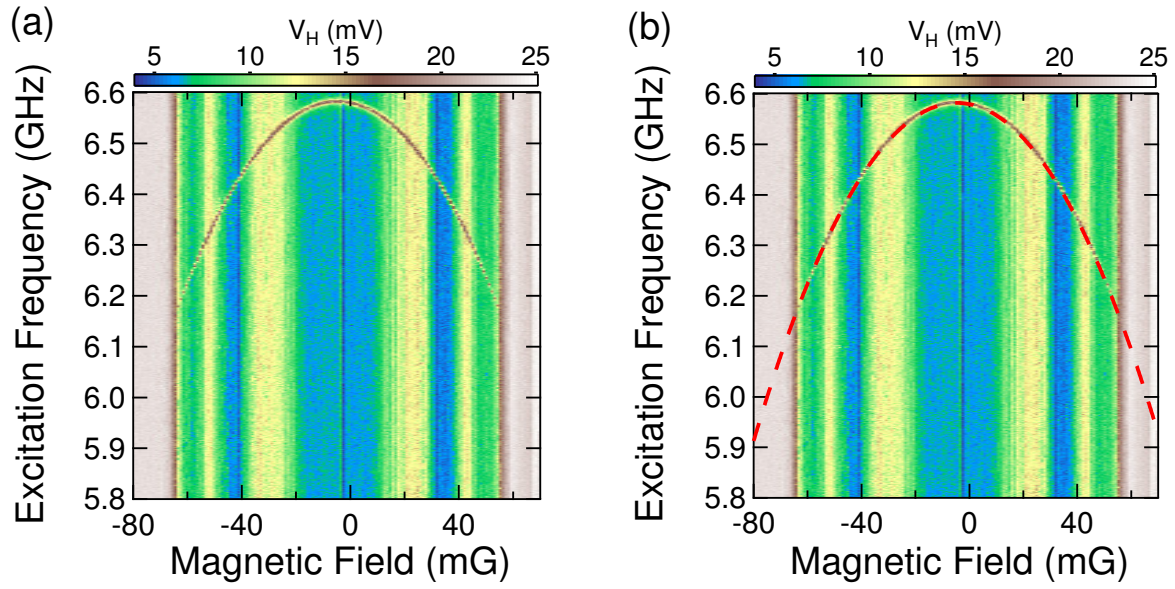


Figure 5.8: (a) Spectroscopy of Meissner transmon (N1) as a function of applied magnetic field. This is raw data. (b) The parabola-like dashed line shows a phenomenological fit to the qubit transition frequency f_{01} versus magnetic field B .

Chapter 6

Time-domain measurements of Meissner qubit

6.1 Rabi oscillation measurement

As shown in the theory section [Sec. 2.1.3], Rabi oscillation is the quantum coherent oscillations between two quantum states (qubit) when classical harmonic radiation is applied. During the oscillation, the relative phase between the coefficients of the ground and excited state remains well-defined. The Rabi oscillation is a key signature of a qubit since it shows quantum coherence between two energy state. The qubit state under continuous microwave radiation evolves in the case of zero detuning, i.e. qubit frequency = microwave frequency, as given by Eq. (2.38)

$$|\Phi(t)\rangle = \cos(\Omega_0 t/2)|0\rangle + \sin(\Omega_0 t/2)e^{-i\omega_{01}t}|1\rangle, \quad (6.1)$$

where the global phase factor $e^{-E_0 t/\hbar}$ is ignored without losing generality, and Ω_0 is Rabi frequency in the case of zero detuning. One should remember that the Rabi frequency is proportional to the amplitude of the applied microwave.

To observe the Rabi oscillations, one needs to measure the probability to find the qubit in the first excited state as a function of time at the same time that microwave is applied to the qubit. In practice, a microwave pulse with variable duration, with the qubit in the ground state, is applied and immediately the readout pulse is sent to measure the qubit state. The pulse sequence is shown in Fig. 6.1(a), where the Δt is the pulse length or duration.

During Δt , the microwave with frequency ω_s is applied continuously, in other words, the microwave pulse with length Δt is applied, followed by a readout pulse to measure the qubit state. In Fig. 6.1(b), the trajectory of the qubit state during the Rabi oscillation is depicted. Note that the Bloch vector rotates around $+\mathbf{x}$ counterclockwise by an angle $\theta = \Omega_R \cdot \Delta t$ at an angular frequency Ω_R .

A representative plot of the Rabi oscillation in zero detuning can be seen in Fig. 6.2(b). The heterodyne voltage (V_H) is not converted to the probability P_1 —the qubit in the excited state, but they have linear

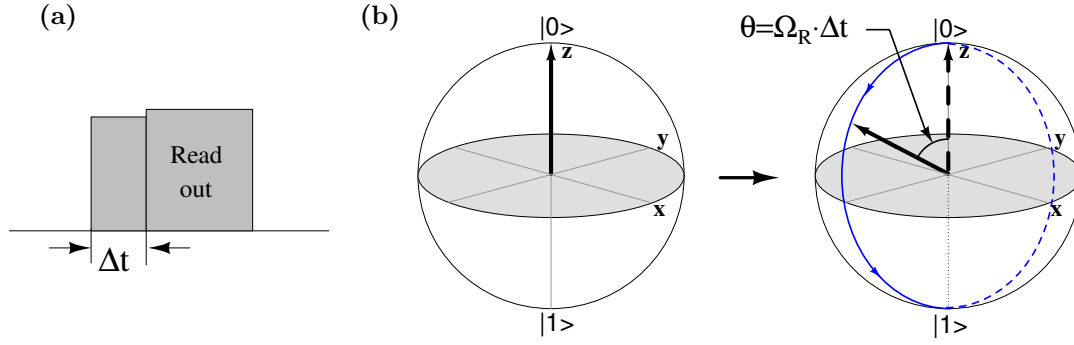


Figure 6.1: (a) A schematic of pulse sequence for Rabi oscillation measurement. Δt is variable pulse length. (b) Bloch sphere representation of Rabi oscillation measurement. The qubit is initially in the ground state $|0\rangle$. During the microwave with pulse length of Δt , the arrow rotates around $+x$ by $\theta = \Omega_R \cdot \Delta t$, indicating that the qubit state becomes a superposition of the ground and first excited state. The arrow is used to point to the qubit state mapped on the surface of Bloch sphere. The blue solid and dashed lines shows the trajectory of the qubit state during Rabi oscillation, during which the arrow rotates at an angular frequency Ω_R .

relation; the minimum voltage corresponds to $P_1 = 0$ and the maximum voltage to $P_1 = 1$. The step size of the pulse length is 40 ns. The data also shows that the Rabi frequency is $\Omega_0 = 1$ MHz, and the envelope of the oscillations decays gradually, but not necessarily exponential. In fact, the decay law originates the decoherence rate ($\tilde{\Gamma}_2$), analogous to T_2 . The corresponding dephasing rate is given by [42]

$$\tilde{\Gamma}_2 = \frac{3 - \cos^2 \eta}{4} \Gamma_1 + \Gamma_\varphi \cos^2 \eta + \frac{1}{2} \Gamma_\nu \sin^2 \eta, \quad (6.2)$$

where $\Gamma_\nu \equiv \pi S_{\delta\omega_z}(\omega_R)$ is the spectral density at Rabi frequency, and η is defined by $\eta = \tan^{-1}(\omega_0/\Delta)$, following the notation in Eq. (2.35). In particular, for the zero detuning case ($\cos \eta = 0$), $\tilde{\Gamma}_2 = 3\Gamma_1/4 + \Gamma_\nu/2$, which contrasts with $\Gamma_2 = \Gamma_1/2 + \Gamma_\varphi$ for free evolution case. Thus, the decay time of the Rabi oscillation is determined by both the qubit relaxation rate and the noise spectral density at Rabi frequency.

The Rabi frequency at zero detuning is proportional to the amplitude of the harmonic irradiation, i.e., amplitude of spectroscopic microwave signal, as explained in Sec. 2.1.3. The measured Rabi frequency versus amplitude of spectroscopic microwave is depicted in Fig 6.2(a). As expected, the Rabi frequency is linear to the amplitude.

Meanwhile, so far, we considered the zero detuning case. With nonzero detuning, we already discussed that the Rabi frequency is larger than that of the zero detuning case, and also the amplitude of the probability $P_1(t)$ reduces as the detuning increases as shown in Fig. 2.3. The Rabi oscillations for both zero and nonzero detuning cases can be seen in the 2D image plot in Fig. 6.2(c). The color represents the heterodyne voltage. The Rabi oscillations are represented as wavy patterns. Obviously, the qubit transition frequency is the

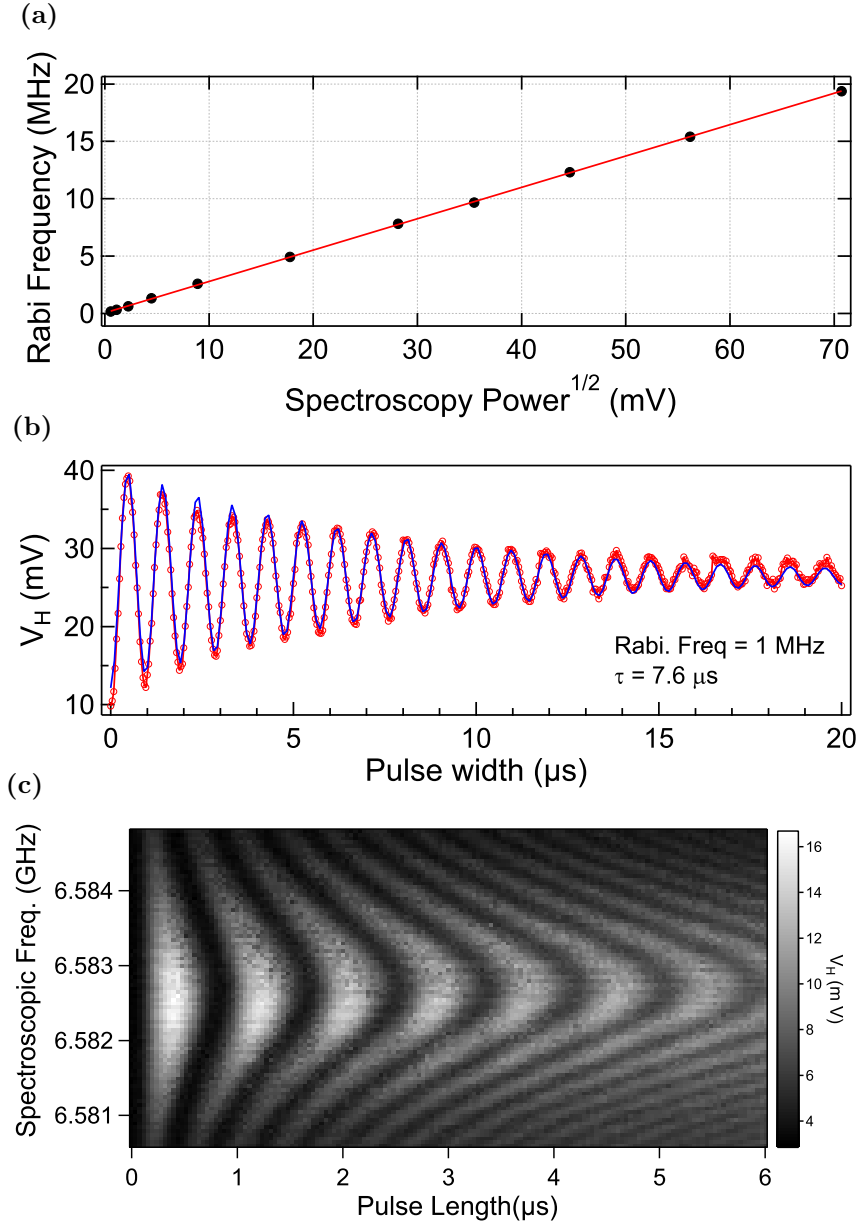


Figure 6.2: (a) Rabi frequency versus amplitude of spectroscopic microwave is plotted for zero detuning case ($\omega_{01} = \omega_s$) in linear scale. The line is a linear fit, illustrating that the Rabi frequency is proportional to the amplitude of the applied microwave. (b) A representative plot of the Rabi oscillation for zero detuning case. The blue solid line is a sine-damped fit to the data. The amplitude decays almost exponentially with time scale of $7.6 \mu\text{s}$. The Rabi frequency turns out 1 MHz. (c) An image plot of the transmission as a function of spectroscopic frequency and pulse length, showing Rabi oscillations over the wide range of detuning. At a fixed spectroscopic frequency, the alternating black and white color represents the Rabi oscillation. The qubit transition frequency is ~ 6.5828 GHz, where the separation between the white region is maximum. As the detuning increase, i.e., the frequency gets farther away from 6.5828 GHz, the Rabi frequency increases as evidenced by the patterns become squeezed. Also, the overall oscillation amplitude is reduced as observed that the patterns get darker.

frequency “line” with respect to which the pattern is symmetric; $\omega_{01}/2\pi = 6.5828$ GHz. Clearly, one can see that the Rabi frequency increases as the detuning grows—the distance between adjacent maxima gets smaller. Also, it can be seen that the amplitude of the oscillation gets reduced as the detuning increases—darker.

6.1.1 Calibrating π and $\pi/2$ pulses

In performing time-domain measurements, we need to use π and $\pi/2$ pulses to rotate the qubit. They are nothing but the short microwave pulses whose lengths are t_π and $t_{\pi/2}$ such that $P_1(t_\pi) = 1$ and $P_1(t_{\pi/2}) = 1/2$ as shown in Fig 2.3. In principle, π and $\pi/2$ pulses can be found from Rabi oscillation measured in equal time step as shown in Fig. 6.2(b). However, creating pulses with the length of the measured t_π and $t_{\pi/2}$ are not always possible due to the limited time resolution provided from a pulse-generating device or in our case arbitrary waveform generator (AWG). In fact, it is not very practical to create a pulse with arbitrary pulse length due to technical issue ¹. Alternatively, it is much more practical to choose a desired Rabi frequency (depending on our need) and in turn the pulse length for π and $\pi/2$ pulses. Since the Rabi frequency can be adjusted easily by changing the amplitude of the microwave pulse, one can find the right pulse amplitude in straightforward way.

In calibrating the pulse amplitude, we first set the pulse length calculated from the chosen Rabi frequency, and sweep the pulse amplitude starting from sufficiently low amplitude such that Rabi frequency is pretty small. For example, in Fig. 6.3(a), five Rabi oscillations are depicted. Let us suppose that we want Rabi frequency of 50 MHz so that π pulse is 10 ns. Now the 10 ns microwave pulse is applied, followed by readout. As the pulse amplitude increases, the Rabi frequency and P_1 increase accordingly until the Rabi frequency becomes 50 MHz. Once the Rabi frequency is over 50 MHz, the P_1 starts to fall; the P_1 should oscillate as the pulse amplitude keeps increasing. Therefore, the calibration of π pulse comes down to finding the pulse amplitude which gives the first maximum probability P_1 or the maximum heterodyne voltage V_H in high-power measurement. Experimental data on the heterodyne voltage versus pulse amplitude is shown in Fig. 6.3(b). The blue line is a fit with a sine function. The sinusoidal behavior is expected as can be seen in Eq. (2.39) : $P_1(t) = \sin(\Omega_0 t)$, where the Rabi frequency Ω_0 is proportional to pulse amplitude. It is worth noting that the pulse amplitude can be changed in two different ways, when a microwave pulse is created by mixing a continuous microwave (LO) and a voltage pulse (IF) with RF mixers in series. First, the height of voltage pulse shaped by arbitrary waveform generator (AWG) changes the amplitude of the output pulse almost in linear manner. Second, the power of the microwave in local oscillator port (LO) can be changed

¹To create a voltage pulse that shapes a microwave pulse, one has to create a ascii file.

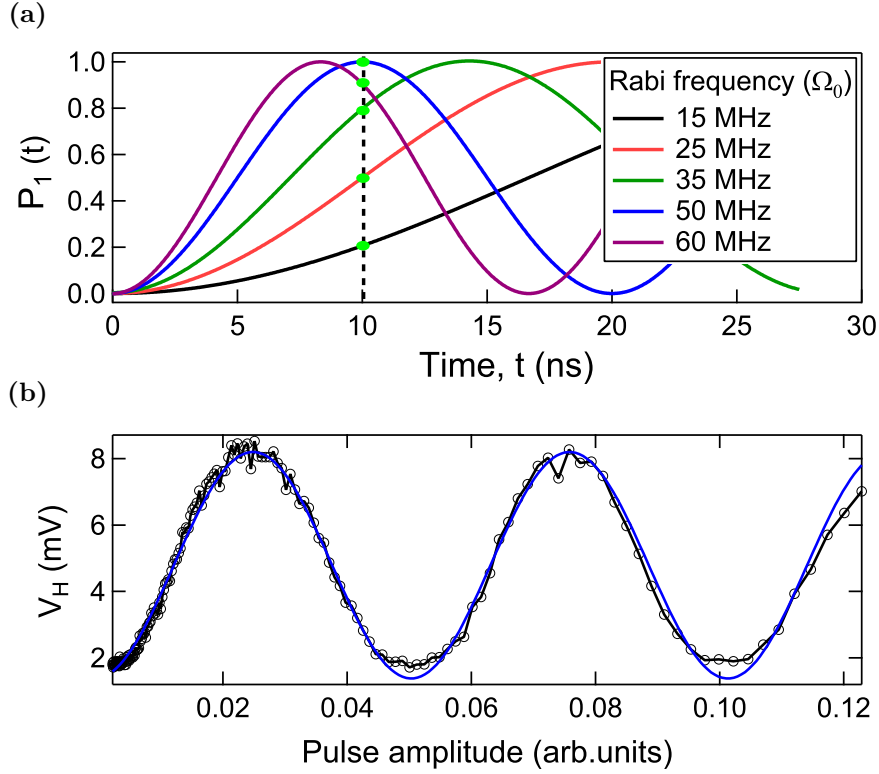


Figure 6.3: (a) Theoretical plot of the probability $P_1(t)$ of the excited state versus time or pulse length t , illustrating Rabi oscillations with different Rabi frequencies. The green dots at $t = 10$ ns show how P_1 changes as Rabi frequency is varies, for example, by changing the amplitude of excitation pulse. (b) A representative data of the transmission versus the amplitude of excitation pulse. The transmission, i.e., P_1 , is supposed to follow a sine wave as expected by Eq. (2.39): $P_1(t) = \sin(\Omega_0 t)$, where the Rabi frequency Ω_0 is proportional to the pulse amplitude, and t is fixed. The blue line is a fit with the sine function.

to vary the pulse height, however, this method doesn't necessarily provide the linear relation between the amplitude of the LO microwave power and output pulse height due to intrinsic nature of a RF mixer. For example, if the supplied RF power at LO is lower than specified LO drive power, the output goes quite linearly, but if the LO power is set to the specified LO drive power, the output almost doesn't change. This is because the specified LO drive power is the power required to turn on and off diodes in the mixer circuitry. More importantly, more concerning part in using the lower LO power than the specified LO drive power is that the on-off ratio of a pulse is normally mitigated, which adversely affects the qubit—leakage microwave could cause unexpected qubit transitions. Therefore, care must be taken in calibrating microwave pulses. It is recommended to check on-off ratio of a microwave pulse, whenever possible.

6.2 Relaxation time, Ramsey fringe and Hahn spin echo measurement

In previous section, we showed how to prepare π and $\pi/2$ pulses, which are needed for all three conventional time-domain measurements: relaxation time, Ramsey Fringe, and spin echo measurement. The three times scales obtained from those measurement provides a qubit's dynamical characteristics. In general, extensive effort to increase the time scales have been made over the last several decades, and with the transmon, about $100\ \mu\text{s}$ can be achieved.

6.2.1 Relaxation time measurement

The relaxation time measurement is carried out simply by applying a π pulse to make pure excited state and read out the state after a time interval Δt . First, the qubit is initialized in the ground state by waiting enough time for the qubit to relax to the ground state at base temperature. The waiting time must be much longer, practically, at least three time longer than the actual relaxation time. In fact, such required waiting time sets the upper bound for repetition rate. For example, T_1 is about $30\ \mu\text{s}$ and a single shot measurement takes $100\ \mu\text{s}$, then the repetition rate should be slower than $10\ \text{kHz}$ ($=1/100\ \mu\text{s}$).

Once the qubit is prepared in the ground state, then π pulse is applied to the sample, placing the qubit in pure excited state. The excitation (or spectroscopy) frequency ω_s is set to be the same as the qubit transition frequency, $\omega_s = \omega_{01}$. Since the qubit is in pure state, not a superposition, there is no pure dephasing involved—no phase evolution. The qubit is left for a variable time Δt , and is read out using a readout pulse. A representative plot of the relaxation measurement is shown in Fig. 6.4(a). In this measurement, $100\ \text{ns}$ π pulse was used. We can see the heterodyne voltage V_H exponentially decays as a function of time. The T_1 is obtained by fitting the data with a typical exponential function, $f(t) = y_0 + A \exp(-t/T_1)$.

Meanwhile, Fig 6.4(b) show the timing diagram of voltage pulses from the arbitrary waveform generator (AWG). $100\ \mu\text{s}$ voltage output acts as a single shot measurement (one cycle) and each cycle is repeated to get the readout voltage signal average over about 10k times; the number of averages required depends on the desired signal to noise ratio. The voltage pulse from the CH1 is mixed with a continuous microwave signal in a mixer to create a square-pulse, and the rising edge occurs at the position of $85\ \mu\text{s}$. The CH2 voltage is used to shape one π pulses which are separated by Δt from the readout pulse. The Mark1 is one of the digital outputs from the back panel of the AWG, and is used to trigger the high-speed digitizer to measure the heterodyne voltage of the transmission of the cavity—voltage amplitude of the transmitted readout pulse. If the number of average is 10k and the repetition rate is $5\ \text{kHz}$, then each data point in the

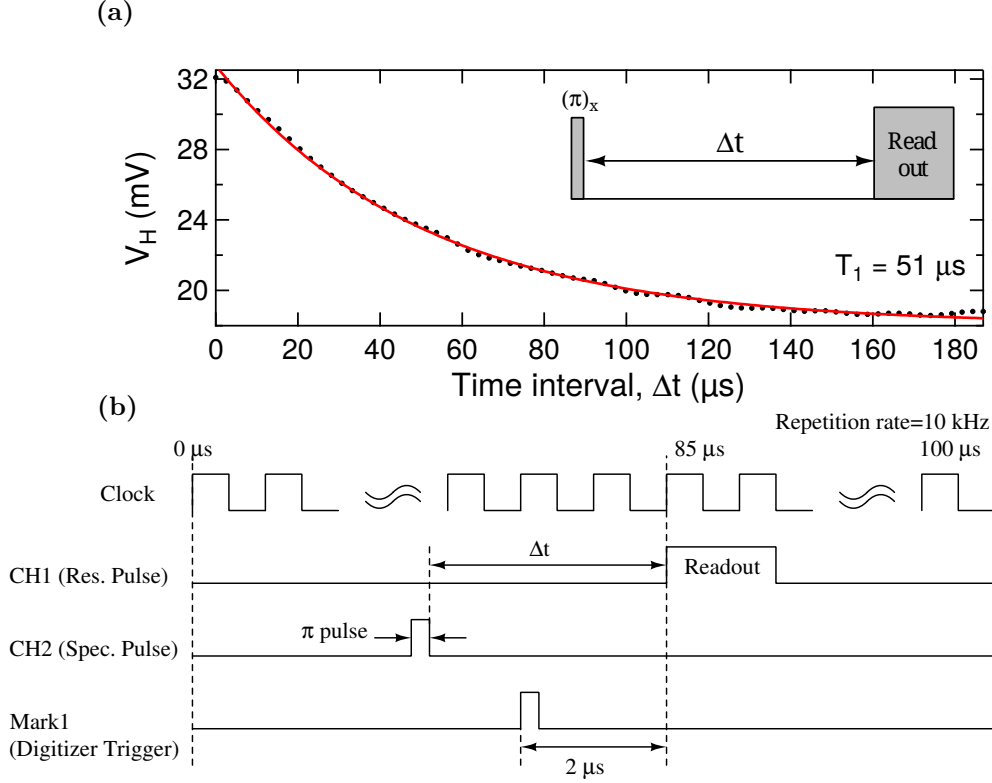


Figure 6.4: (a) A representative plot of relaxation time measurement for sample N7. The 100 ns π pulse was used. The heterodyne voltages of $V_H = 18$ and 33 mV correspond to the qubit being in the ground state and excited state. The red solid line is an exponential fit, giving $T_1 = 51 \mu\text{s}$. The inset shows the schematic of the pulse sequences. The time interval Δt was varied from 0 to 185 μs . (b) The timing diagram of the voltage pulses from the arbitrary waveform generator. One cycle (single shot) takes 200 μs , so the repetition rate is 5 kHz. For each Δt , the CH2 is updated only.

T_1 measurement takes approximately $10000 \times 200 \mu\text{s} = 2 \text{ s}$.

6.2.2 Ramsey fringe measurement

The Ramsey fringe measurement is a conventional technique to measure the decoherence time T_2^* . The measurement method is quite similar to the relaxation time measurement described in the previous section. Unlike the T_1 measurement, the Ramsey fringe measurement requires the qubit be initialized in the 50/50 superposition state to trigger phase evolution. Therefore, the first step is to apply the first $\pi/2$ pulse to prepare the qubit for $(|0\rangle - i|1\rangle)/\sqrt{2}$. Then we let the qubit evolve during Δt_R freely—free evolution—and the second $\pi/2$ pulse is applied to rotate the qubit around $+\mathbf{x}$ by 90 degree, followed by immediate readout pulse. The Bloch sphere representation of the qubit state before the readout is depicted in Sec. 2.1.4. It should be reminded that the qubit state is represented in the rotation frame which rotates at the excitation frequency ω_s with respect to the lab frame. To observe the fringe, it is necessary, unlike the relaxation

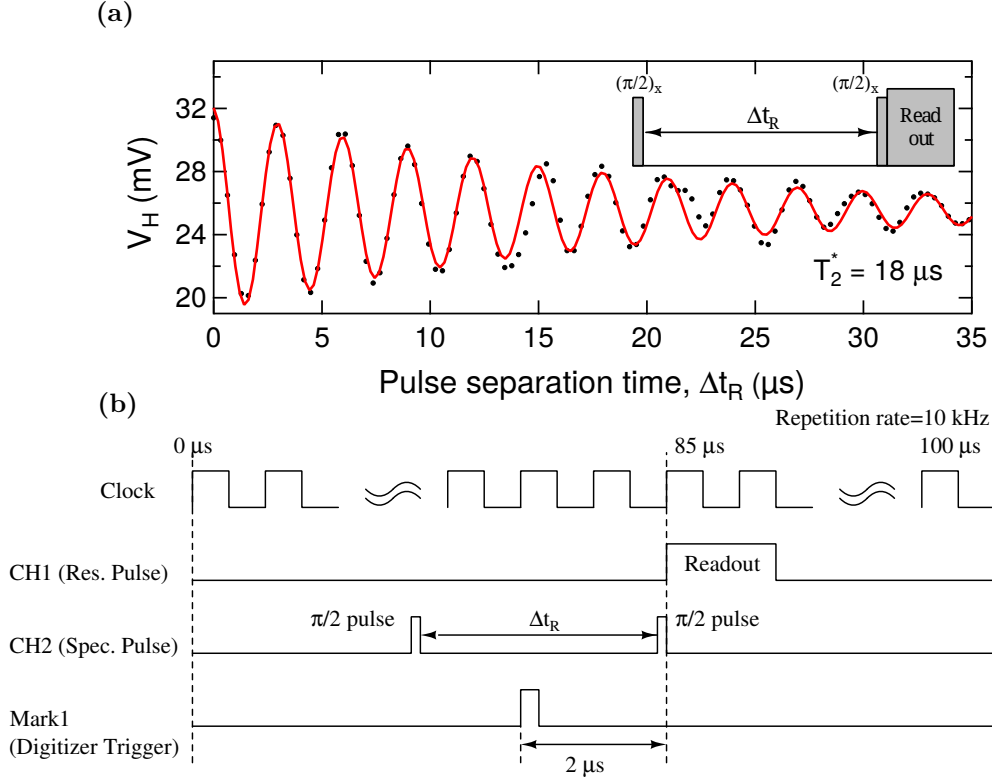


Figure 6.5: (a) A representative plot of Ramsey fringe measurement for sample N7. The heterodyne voltages of $V_H = 18$ and 33 mV correspond to the qubit being in the ground state and excited state. The red solid line is a fit with the sine-damped function, giving $T_2^* = 18 \mu$ s. The inset shows the schematic of the pulse sequences. The time separation Δt_R was varied from 0 to 35μ s. (b) The timing diagram of the voltage pulses from the arbitrary waveform generator. One cycle (single shot) takes 100μ s, so the repetition rate is 10 kHz. For each Δt , the CH2 is updated only.

measurement, to detune the excitation frequency from the qubit transition frequency, i.e., $\Delta = \omega_q - \omega_s \neq 0$. The absolute value of the detuning becomes the oscillation frequency ω_R of the Ramsey fringe, $\omega_R = |\Delta|$. If the detuning is zero, then the qubit does not rotate on the equator of the Bloch sphere—thus no fringe. In addition, this detuning should be much smaller than the Rabi frequency at zero detuning, Ω_0 , i.e., $|\Delta| \ll \Omega_0$ so that $\Omega_R = \sqrt{\Omega_0^2 + \Delta^2} \approx \Omega_0$, since otherwise the microwave pulses calibrated for π and $\pi/2$ pulses at zero detuning would not be π and $\pi/2$ any more—Rabi frequency depends on the detuning.

However, even if the detuning is zero, there is a way to create a fringe: adding an additional phase shift $\omega_s \cdot \Delta t_R$ to the second $\pi/2$ pulse. The additional phase shift makes a new rotation axis $\mathbf{n} = \cos(\omega_s \Delta t_R) \mathbf{x} + \sin(\omega_s \Delta t_R) \mathbf{y}$, where \mathbf{n} , \mathbf{x} , and \mathbf{y} are unit vectors.

A representative plot of Ramsey fringe measurement for sample N7 is shown in Fig. 6.5(a). Here, 50 ns

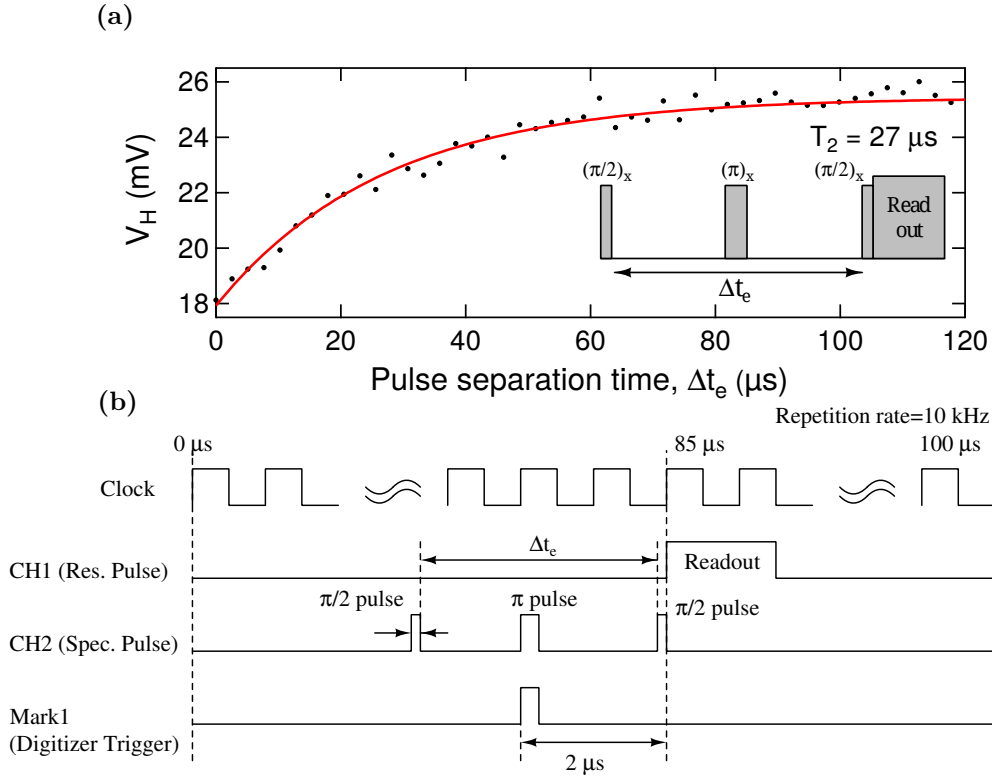


Figure 6.6: (a) A representative plot of relaxation time measurement for sample N7. The heterodyne voltages of $V_H = 18$ and 33 mV correspond to the qubit being in the ground state and excited state. The red solid line is an exponential fit, giving $T_2 = 27$ μ s. The inset shows the schematic of the pulse sequences. The time separation Δt_e between two $\pi/2$ pulses was varied from 0 to 120 μ s. The π pulse is placed right in the middle of two $\pi/2$ pulses. (b) The timing diagram of the voltage pulses from the arbitrary waveform generator. One cycle (single shot) takes 100 μ s, so the repetition rate is 10 kHz. For each Δt , the only CH2 is updated.

$\pi/2$ pulse was used. The T_2^* is obtained by fitting the data with a sine-damped function

$$f(t) = y_0 + Ae^{-t/T_2^*} \sin(\omega_R \Delta t_R + \phi_0) \quad (6.3)$$

The timing diagram of the AWG voltages for the Ramsey fringe measurement is shown in Fig. 6.5(b). The pulse sequence is the same as that of the relaxation measurement except the CH2 voltage pulses.

6.2.3 Hahn spin echo measurement

The Hahn spin echo measurement allows us to get T_2 time. The only difference from the Ramsey fringe measurement is that a π pulse, called refocusing pulse in NMR, is inserted between two $\pi/2$ pulses. The π pulse refocuses the broadening of the qubit state, cancelling out the dephasing caused by low frequency noise present during ensemble average measurements.

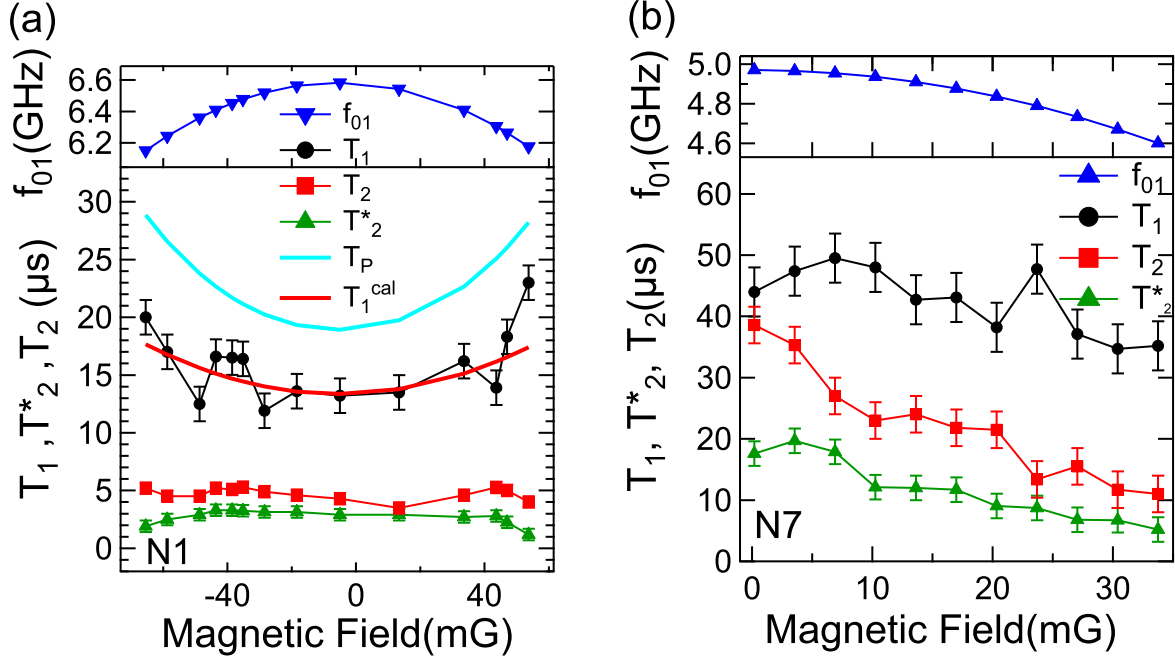


Figure 6.7: (a) Magnetic field dependence of the qubit frequency (f_{01}), three measured time scales (T_1, T_2^* , and T_2) and two calculated time scales (T_P and T_1^{cal}) at low magnetic field much smaller than the SQUID oscillation period for the sample N1. T_P (Purcell time) was calculated by $T_P = 1/\Gamma_P$ —inverse of Purcell rate, and T_1^{cal} by $1/T_1^{\text{cal}} = 1/T_{\text{NP}} + 1/T_P$ (see texts) (b) The qubit frequency and three measured time scales for N7.

A representative plot of the spin echo measurement is shown in Fig. 6.6(a), and also the pulse sequence in the inset. The $\pi/2$ and π pulses were 50 ns and 100 ns, respectively. Unlike the Ramsey fringe, there is no fringe, because the qubit returns to the ground state after the second $\pi/2$ pulse. As can be seen in the Bloch sphere representation in Sec 2.1.4, the qubit state flips to the first quadrant of the xy-plane by the π pulse and ends up being at $+\mathbf{y}$. To create a fringe, there are two ways to do it. The first method is, for a fixed Δt_e , to vary the separation time between the first $\pi/2$ pulse and the π pulse from zero to Δt_e . The second method will be, as explained in the previous section (Ramsey fringe), to add an additional phase shift to the second $\pi/2$ pulse. Practically, the second method would be easier because the phase of the excitation microwave signal can be easily tuned by simply changing I and Q voltages to an IQ mixer (see Appendix D for more detail).

6.3 Low magnetic field

In this section, we investigated the coherence times around zero magnetic field. From now on, we will show two representative sample denoted by N1 and N7. In Fig. 6.7, we present f_{01} , T_1 , T_2^* and T_2 versus magnetic

field in the vicinity of the sweet spot at $B=0$. The weak magnetic field less than 60 mG is not strong enough for vortices to penetrate into the electrodes, while they may enter the antenna. In fact, vortices begin to enter the electrodes at a much higher field, approximately 2 Gauss (see Fig. 6.8). The higher field case will be discussed in the next section.

The measurement procedure was as follows. First, the magnetic field was set. Second, the spectroscopy in high power measurement was carried out to find the qubit transition frequency. Third, the optimum drive power was found by sweeping the drive power both for the ground and the first excited state, and taking the difference of the transmissions for the two cases. Fourth, the amplitude of spectroscopic pulse was calibrated (found) for π pulse (100 ns) corresponding to Rabi frequency 5 MHz. Finally, the relaxation time, Ramsey fringe and spin echo measurement were performed to measure T_1 , T_2^* and T_2 . These steps were repeated for all magnetic field points.

We first examined the energy relaxation time, T_1 , for both samples. They were measured separately in the same cavity which has its loaded lowest order mode at ~ 8.42 GHz with a loaded (measured) quality factor $Q_L = 5000$. As Fig. 6.7(a) and 6.7(b) show, at zero field T_1 was substantially larger for N7 than for N1. Furthermore, when a small magnetic field was applied, the energy relaxation time for N1 increased, while hardly any change was observed for N7. Both of these effects can be understood as consequences of the Purcell effect in which the rate of spontaneous emission is increased when a cavity mode to which the qubit couples lies close by in frequency. The excitation frequency of N7 (4.97 GHz) was further from the cavity frequency than was the excitation frequency of N1 (6.583 GHz) and this almost completely determines the difference in T_1 . To see this we first compare the measured ratio Γ_{N1}/Γ_{N7} and the calculated ratio of Purcell rates for the two devices. (Since the next higher cavity resonance is more than 11 GHz above the fundamental, we ignore its contribution to the Purcell relaxation rate.) For the Purcell relaxation rate we use $\Gamma_P = \kappa(g/\Delta)^2$, where $\kappa = \omega_c/Q_L$ is the cavity power decay rate, g is the qubit-cavity coupling rate, and Δ is the qubit-cavity detuning $|\omega_{01} - \omega_c| = 2\pi|f_{01} - f_c|$. The ratio of the Purcell rates depends only on the qubit-cavity frequency differences which are easy to measure. We find that the ratio of the measured lifetimes for qubit 1 divided by qubit 2 is $T_{1,N1}/T_{1,N7} = 13 \mu s / 44 \mu s = 0.3$ while the ratio of the calculated Purcell times, $T_P = 1/\Gamma_P$ is $(\Delta_{N1}/\Delta_{N7})^2 = 0.29$. Since these numbers are very close to each other, most of the relaxation must be Purcell limited.

However, knowing the qubit-cavity coupling which was measured to be $g = 130$ MHz, we can go further and more carefully account for other loss mechanisms by writing the total relaxation rate $\Gamma = 1/T_1$ as $\Gamma = \Gamma_P + \Gamma_{NP}$, where Γ_{NP} is the non-Purcell rate and Γ_P is the Purcell rate discussed above. Using the known Q_L and cavity coupling, we can evaluate Γ_P for both devices and then obtain Γ_{NP} for each

one by subtracting Γ_P from the measured relaxation rate. For N1 we obtain $\Gamma_{P,N1} = 2\pi \times 8.5$ kHz, giving $\Gamma_{NP,N1} = 2\pi \times 3.5$ kHz ($T_{NP,N1} = 45$ μ s) and for N7 we obtain $\Gamma_{P,N7} = 2\pi \times 2.4$ kHz, giving $\Gamma_{NP,N7} = 2\pi \times 1.2$ kHz ($T_{NP,N7} = 132$ μ s). This analysis reveals that the relaxation time would reach more than 100 μ s if it were not Purcell-limited, indicating that the coupling to energy absorbing defects in the circuit and qubit is low.

The increase in relaxation time for N1 as magnetic field was applied and the notable lack of such dependence for N7 can also be understood as consequences of the Purcell effect. Since the qubit frequency decreases with applied magnetic field, this causes the detuning to increase. This makes a measurable difference in Γ_P for N1 but not for N7, since the detuning of N7 is almost twice as large as N1. Also for N1, we plotted the relaxation time T_1^{cal} versus the magnetic field B as shown in Fig. 6.7(a). The T_1^{cal} was calculated by $1/T_1^{\text{cal}}(B) = \Gamma_P(B) + \Gamma_{NP}$, where $\Gamma_{NP} = 2\pi \times 3.5$ kHz is a constant Non-Purcell rate estimated at zero magnetic field and the Purcell rate Γ_P solely depends on the experimental qubit frequency f_{01} for cavity-detuning. We see this estimate explains the relaxation time data for N1 reasonably well.

We now consider the spin echo coherence time T_2 at $B=0$ which measures the phase coherence attainable in a qubit process. T_2 is related to T_1 by the constitutive relation $1/T_2 = 1/(2T_1) + 1/T_\varphi$, where T_φ is the dephasing time due to random phase fluctuations. N1 had a much shorter T_2 than N7. Specifically, $T_{2,N1} = 4.2$ μ s and $T_{2,N7} = 39$ μ s, almost ten times as large. Using the measured values of T_1 we obtain $T_{\varphi,N1} = 3$ μ s and $T_{\varphi,N7} = 70$ μ s. We attribute the much longer dephasing time for N7 to the fact that the testing conditions were different. For measurements of N7, base-temperature copper powder filters were added to the input and output ports of the test set-up. These are known to reduce photon noise by providing attenuation at low temperature. Such photon noise may be responsible for the significantly lower dephasing time seen in the N1 measurements. Photon noise can induce dephasing because of strong ac-Stark shift [61]. Meanwhile, the T_2 of both samples became shorter as magnetic field was applied. Since this leads to shifting from the magnetic sweet spot, this behavior can be expected. The qubit becomes more susceptible to dephasing caused by flux noise as the slope of the qubit frequency versus magnetic field increases away from the sweet spot where it is zero.

6.4 High magnetic field

Now we consider a different regime where the high magnetic field creates vortices on the electrodes. We primarily investigated the effect of vortices on the coherence times. Since we zero-field-cooled the devices, there were no vortices in the electrodes to begin with. We managed to gradually increase the number of

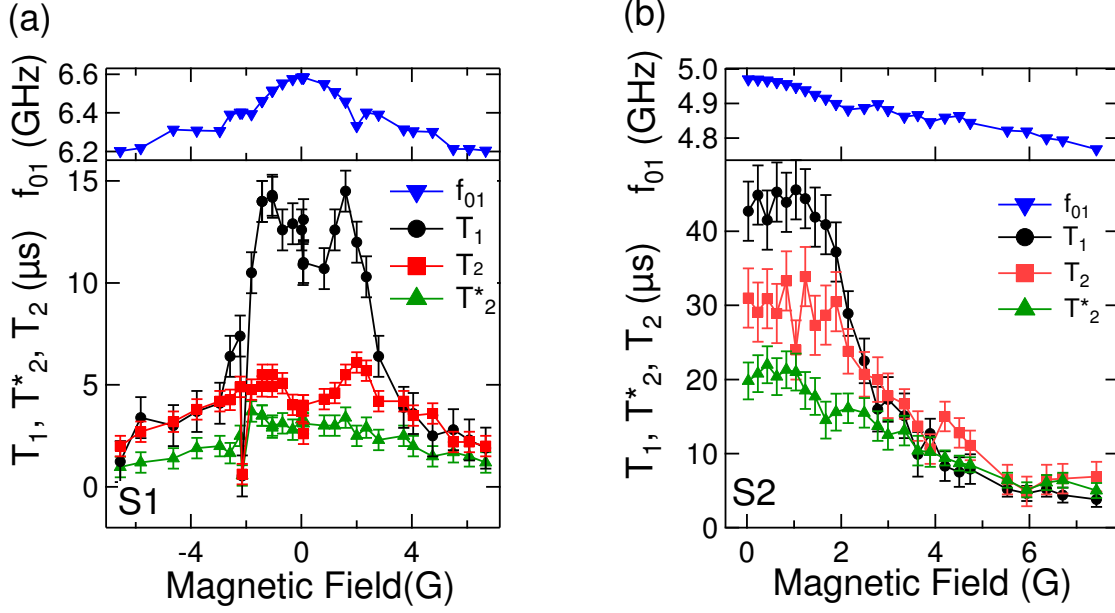


Figure 6.8: The qubit transition frequencies (f_{01}) and three times scales (T_1, T_2^* , and T_2) were measured at the sweet spots over the wide range of magnetic field for the N1 (a) and N7 (b).

vortices by turning up the external perpendicular magnetic field. In what follows, we present measurements at high magnetic fields, i.e., sufficiently high that vortices may be introduced into the electrodes. All these measurements have been made at sweet spots, which occur periodically with the magnetic field.

In contrary to a single transmon, the Meissner transmons have advantage to allow us to observe the entrance of a vortex (or multiple vortices) into the electrodes. In actual measurement, we ramped up the magnetic field until the next sweet spot was reached [see Fig. 5.5]. Upon the event of vortex entrance, we observed two signatures: hysteresis of the transmission plotted versus the magnetic field and a shift of the next sweet spot to higher magnetic field than expected. In other words, the vortex entrance into one of the electrodes is always manifested by a violation of the exact periodicity of the Little-Parks oscillation [Fig. 5.5]. All the time-domain measurements were performed at the consecutive sweet spots.

A vortex in the film adds to the Meissner current the vortex current, so the entrance of a vortex shifts the location of the sweet spots with respect to the original location. Therefore, we realize in our device a direct coupling of a vortex to the qubit. The qubit can be used to study decoherence processes in the vortex, which is discussed below in detail.

In Fig. 6.8(a), we show the magnetic field dependence of three times scales and the qubit frequency for N1. We found that T_1 was enhanced from 10 μ s to 14 μ s as the magnetic field was applied up to about 2 Gauss and then sharply falls down above it. However, for N7 [Fig. 6.7(b)], all three time scales stayed almost

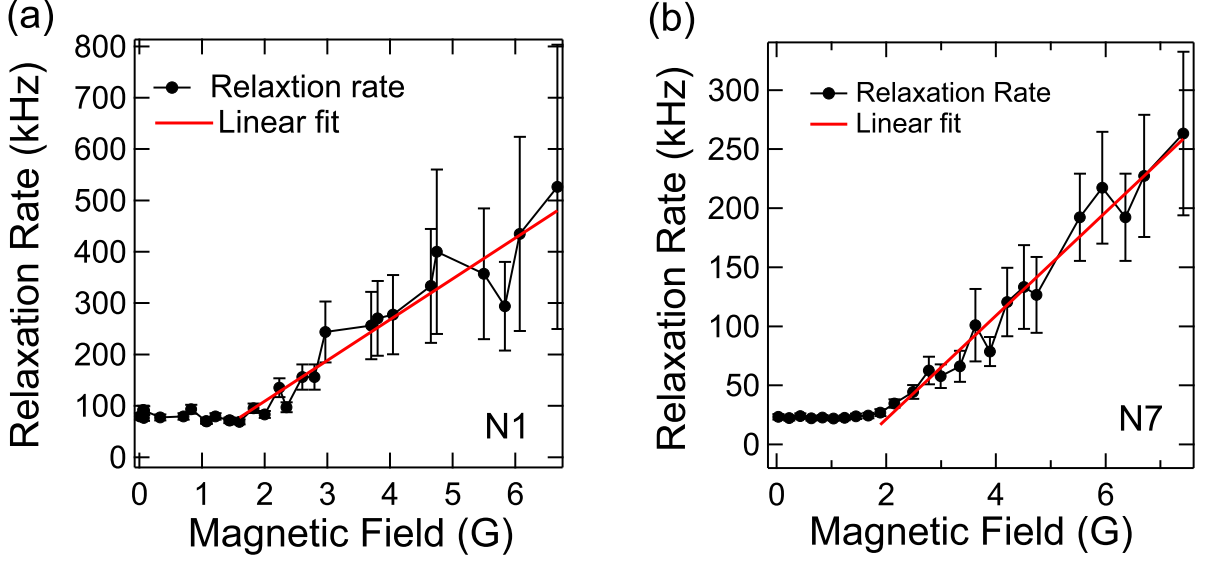


Figure 6.9: The relaxation rates $\Gamma=1/T_1$ versus magnetic field were plotted for both N1 (a) and N7 (b). All measurements have been done at the sweet spots. The linear fits (red solid lines) were shown over the magnetic field range where the vortices were present in the electrodes.

constant up to about 2 Gauss and started to drop as the field was increasing further. Below $B \approx 2$ Gauss that we call a critical field for vortex entrance to the *electrodes* B_{c1} , we did not see any shift of the sweet spots and the hysteresis of transmission. This observation reflects that no vortex entered the electrodes. Note that vortices in the antenna should make negligible effect on the shift of transmission because they stay far away from the electrodes and have negligible effect on Meissner current in the electrodes.

In Ref. [62], the authors estimated the critical field $B_{c1} = \Phi_0 / [2\pi\xi\sqrt{2\lambda_\perp X}]$, where $\lambda_\perp = 2\lambda(0)^2/d$ is a Pearl length [63]. Using the relations, $\lambda(0) = \lambda_L \sqrt{1 + \xi_0/l}$ and $\xi = \sqrt{\xi_0 l}$, we calculated $B_{c1} = 8.6$ Gauss which gives the same order of magnitude, compared with the measured value, 2 Gauss. Here ξ is the coherence length, ξ_0 is the clean limit coherence length, $\lambda(0)$ is the bulk penetration depth, λ_L is the clean-limit penetration depth for Al, and λ_\perp is the perpendicular penetration depth for our thin film electrodes. The actual values are listed: $\xi_0 = 1600$ nm, $l = 16.7$ nm, $\lambda_L = 16$ nm, $\lambda(0) = 158$ nm, $\lambda_\perp = 552$ nm, $X = 10$ μm .

At the higher field than B_{c1} , the vortices started to enter the electrodes and suppressed the relaxation time significantly (see Fig. 6.8). Meanwhile, the coherence time T_2 (and T_2^*) also decreases mainly due to the reduction of T_1 . Since the measurements were carried out at the sweet spots, the dephasing caused by non-zero dispersion of $f_{01}(B)$ may be neglected.

6.5 Relaxation rate

Our goal now is to achieve a quantitative characterization of the non-radiative relaxation process caused by vortices. For this, we plotted the relaxation rate (Γ) versus magnetic field (B) in Fig. 6.9. The relaxation rate starts to increase above about 2 Gauss, and holds an approximately linear relationship with the magnetic field. The changes of the relaxation rate per Gauss ($d\Gamma/dB$) are 78.5 kHz/G and 43.7 kHz/G for N1 and N7, respectively.

We speculate that the energy relaxation of the qubits is mainly due to energy dissipation from vortex flow resistance caused by viscous drag force per unit length of a vortex, $\mathbf{f}_v = -\eta_1 \mathbf{v}$, where η_1 is a viscous drag coefficient for a vortex of unit length, and \mathbf{v} is the velocity of a vortex [64]. This process is a non-radiative relaxation where energy is released as heat, not photons. We estimate this relaxation rate semi-classically using the Bardeen-Stephen model [64].

6.6 Vortex counting and vortex-qubit interaction

Here we attempt to estimate the energy relaxation rate (Γ_v) caused by a vortex via viscous damping which retards the vortex motion. The amount of energy dissipated per unit time—power—of a vortex is $P = -\mathbf{f}_v d \cdot \mathbf{v} = f_v^2 d / \eta_1$. Thus the energy relaxation rate of a transmon by a vortex can be evaluated as $\Gamma_v = P / (\hbar \omega_{01}) = (f_v^2 / \eta_1) d / \hbar \omega_{01}$, where d is the thickness of film. Meanwhile, the velocity of vortex \mathbf{v} is driven by Lorentz force $\mathbf{f}_L = \mathbf{J} \times \Phi_0$ (this is the force per unit length), \mathbf{J} is a supercurrent density. We set $f_v = f_L$ based on assumption that the effective mass of vortex and pinning force are negligible. Consequently, we obtained the energy relaxation rate per vortex,

$$\Gamma_v = \frac{J^2 \Phi_0^2 d}{\eta_1 \hbar \omega_{01}}, \quad (6.4)$$

The simplest guess would be to conclude that this dissipation rate is zero because the expectation value of the current is zero, $\langle J \rangle = 0$, both in the ground and in the excited state of the qubit. Yet we suggest that, since the dissipation is proportional to J^2 therefore the relevant parameter is $\langle J^2 \rangle$, where the averaging is done for the excited state of the qubit. Thus, in the case of Eq. (6.4), $J = \sqrt{\langle I^2 \rangle} / (Xd)$ is the effective current density magnitude, $\langle I^2 \rangle$ is the expectation value of the squared supercurrent operator with respect to the first excited state, i.e., $\langle e | I^2 | e \rangle$ evaluated numerically, X is the width of the electrodes, and d is the thickness of a film. At this time we are not aware of a theory which would prove this intuition-driven assumption. According to the Bardeen-Stephen model, the viscosity η_1 per unit length was calculated by

the following formulas: $\eta_1 = \Phi_0 H_{c2} / \rho_n$, $H_{c2} = \Phi_0 / (2\pi \xi^2)$, and $\xi = \sqrt{\xi_0 l}$. Here H_{c2} is the critical field of aluminium film; ρ_n is the normal resistance; ξ is the coherence length in disordered limit; ξ_0 is the Pippard coherence length; l is the mean free path.

The model outlined above leads to the following estimates for the relaxation rate induced on the qubit by a single vortex: $\Gamma_v = 89$ kHz/vortex and $\Gamma_v = 48$ kHz/vortex, for samples N1 and N7 correspondingly. The following set of sample-specific parameters has been used for sample N1, $\sqrt{\langle I^2 \rangle} = 29.5$ nA, $J = 32.8$ kA/m², $\omega_{01}/2\pi = 6.583$ GHz, $\eta_1 = 1.1 \times 10^{-9}$ N·s/m², $H_{c2} = 12.2$ mT, $\rho_n = 2.4 \times 10^{-8}$ $\Omega \cdot \text{m}$, $\xi = 164$ nm, $\xi_0 = 1600$, $X = 10$ μm , and $d = 90$ nm. For sample N7, all the parameters are the same, with the exception of $\sqrt{\langle I^2 \rangle} = 18.9$ nA, $J = 21.0$ kA/m², and $\omega_{01}/2\pi = 4.972$ GHz. The electronic mean free path l is calculated from the measured resistivity of the Al films forming the electrodes, according to Ref. [65], using $l\rho_n = 4 \times 10^{-16}$ Ωm^2 . The result is $l = 16.7$ nm.

To compare the relaxation rate Γ_v , computed per a single vortex (see above), with the experimental relaxation rates, $d\Gamma/dB$, measured “per Gauss”, we need to estimate the average number of vortices entering the electrodes as the applied field is increased by one Gauss, dN/dB . Then one can use a formula $d\Gamma/dB = \Gamma_v(dN/dB)$, which assumes that the relaxation rates of all vortices simply add up. It is not possible to know this number with high precision, so we outline three different approaches below. The first two methods, which are very similar, will provide a high bound for dN/dB , while the third one will give us the low bound for this quantity. First, we define B_n as magnetic field values corresponding to consecutive sweet spots, indexed by the integer index $n=0, 1, \dots, 27$. Here 27 is the maximum number of the sweet spots measured on sample N7. The sweet spots correspond to the minima of the HV-signal shown in Fig. 5.5.

At low fields [for $n \leq 6$ in Fig. 6.10(a)], B_n (black open circle) increase linearly with n , as is expected for the situation in which the sweet spots occur periodically with magnetic field. Such exact periodicity is observed only in the low field regime, when there are no vortices in the electrodes. Since the oscillation is perfectly periodic in this vortex-free regime, the positions of the sweet spots of the qubit can be approximated as $B_n = \Delta B \cdot n + B_0$, where ΔB is the unperturbed period of the HV-oscillation and B_0 is the position of the zero’s sweet spot. The linear fit (blue line) in the low-field regime (see Fig.[Fig. 5.5]) gives the value of the period, $\Delta B = 0.2$ G for $n \leq 6$. Note that in such representation the period equals the slope of the B_n versus n dependence, i.e., $\Delta B = dB_n/dn$.

In what follows we discuss the regime occurring above the critical field, with vortices entering the electrodes as the magnetic field is swept up. Since the slope of the B_n versus n dependence changes significantly at $n = 7$, we conclude that $n = 7$ is the first sweet spot at which the external magnetic field is sufficiently strong to introduce vortices into the electrodes. Consequently, the period becomes larger compared to the

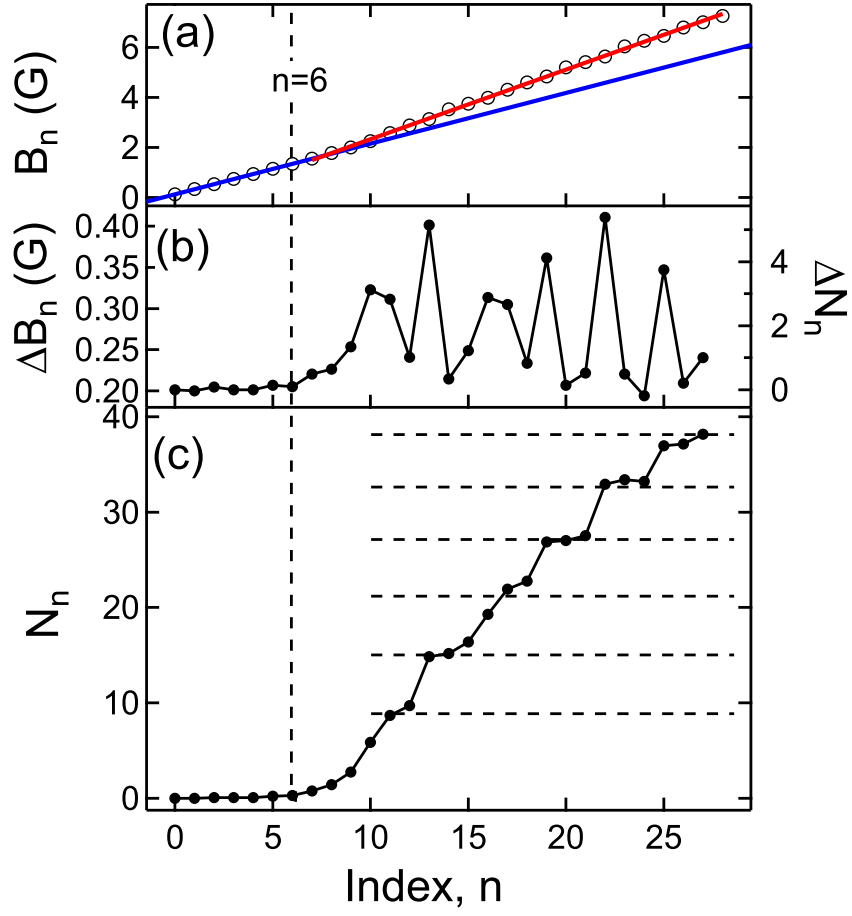


Figure 6.10: (a) The magnetic fields B_n at sweet spots (black open circle) are depicted as a function of n —index of the sweet spots, for sample N7. The blue and red solid lines represent a linear fit to the data for $n \leq 6$ and $n \geq 7$, respectively. The blue fitted line is extended for $n \geq 7$ to show the expected B_n when no vortex penetration is assumed. (b) The difference $\Delta B_n = B_n - B_{n-1}$ is shown on the left axis, while the number of vortices ΔN_n (defined in the text) provides the scale for the right axis. (c) The total number of vortices is calculated by summation of ΔN_n . The dashed lines are periodically spaced. They provide a guide-to-the-eye to emphasize the stepwise characteristics of the increasing number of vortices in the electrodes.

unperturbed case with no vortices. This is because the current of each vortex is opposite to the Meissner screening current. Thus the total phase bias imposed on the SQUID loop by the electrodes [59] increases slower with the magnetic field if the number of vortices in the electrodes increases with magnetic field. Thus the sweet spots tend to occur at higher field values. The new dependence of the position of the sweet spots versus their consecutive number is still approximately linear [see Fig. 6.10(a)], but the slope is larger. The formula for the sweet spot sequence becomes $B_n = (\Delta B + \Delta B_v)n + B_0$, where ΔB_v is the value by which the average interval between the sweet spots is increased, due to the continuous increase of the number of vortices N in the electrodes. The new slope, and, correspondingly, the new period is $\Delta B + \Delta B_v = 0.278$ G,

in the present example of sample N7. This best-fit value is obtained from the linear fit represented by the red solid line in Fig. 6.10(a).

The increase of the period $\Delta B_v = 0.078$ G is attributed to the additional phase bias induced on the SQUID loop by the vortices [66] entering in the electrodes as the field is swept from one sweet spot to the next one, i.e., per one period of the HV-oscillation. This change in the period can now be used to estimate the number of vortices entering the electrodes within one period of the HV-oscillation. Let $\Delta\varphi_v$ denote the phase difference imposed by each single vortex on the SQUID loop of the qubit and ΔN be the average number of vortices entering the electrodes during each period. Then the additional phase difference $\Delta\varphi_{vv}$ accumulated during each period due to all newly entered vortices is $\Delta\varphi_{vv} = \Delta\varphi_v \cdot \Delta N$. Since the vortex currents oppose the Meissner current, the phase difference $\Delta\varphi_{vv}$ is opposite to the phase $\Delta\varphi_M$ imposed by the Meissner current. Therefore the total phase bias generated within one period can be written as $\Delta\varphi_t = \Delta\varphi_M - \Delta\varphi_v$. As in any SQUID-based device, one period of oscillation corresponds to the total phase change by 2π . Thus we have to require $\Delta\varphi_t = 2\pi$ and so $\Delta\varphi_M = 2\pi + \Delta\varphi_v \Delta N$.

The value of $\Delta\varphi_M$, corresponding to the completion of one period, is determined by the function $2\delta(B)$, which is the function defining how much phase bias is produced by the applied magnetic field B [see Eq. (5.2)], taking into account only the Meissner-current-generated phase gradients in the electrodes [59, 60]. Since in the vortex-free regime the period equals ΔB and the phase should change by 2π to complete one period, and also because δB is a linear function of B , we can write $2\delta(B) = 2\pi(B/\Delta B)$, for the vortex-free regime. As vortices begin to enter the electrodes, the period increases, on average, to $\Delta B + \Delta B_v$, as was discussed above. Again, the total phase generated within one period should be 2π . Thus, when vortices are entering we can write $2\delta(\Delta B + \Delta B_v) = 2\pi + \Delta\varphi_v \Delta N$. The last term is needed since at the end of one period the phase generated by the Meissner current has to be larger than 2π , to compensate the opposite phase bias, $\Delta\varphi_v \Delta N$, generated by the newly entered vortices. Remember that the function $\delta(B)$ can be written as $2\delta(B) = 2\pi(B/\Delta B)$. Therefore $2\pi(\Delta B + \Delta B_v)/\Delta B = 2\pi + \Delta\varphi_v \Delta N$. Finally we get the formula $\Delta N = (2\pi/\Delta\varphi_v)(\Delta B_v/\Delta B)$, which defines the average number of vortices entering the electrodes per one period of the HV-oscillation. Thus, for example of sample N7, the number of entering vortices, per one period, is $\Delta N = 2$. In this estimate we have used $\Delta B_v = 0.078$ G, $\Delta B = 0.2$ G, and $\Delta\varphi_v = 1.22$. The latter quantity represents the phase bias generated by one vortex, which is discussed in the following paragraph. Now we are ready to make an estimate of the average number of vortices entering the electrodes as the applied field is changed by one Gauss, which is $\Delta N/(\Delta B + \Delta B_v) = 7.2$.

The estimate above required us to make an assumption that each vortex generates a phase bias $\Delta\varphi_v = 1.22$, on average. In this paragraph we present a justification for this assumption. For this, consider one

vortex in the center of one of the electrode, illustrated in Fig. 3.1(d). Then, according to Ref. [66], $\Delta\varphi_v$ is equal to the polar angle Θ_v subtended by the line connecting the entrance points of the two bridges leading to the JJs forming the SQUID. Therefore, for our samples, $\Delta\varphi_v = \Theta_v = 2 \tan^{-1}[2Z/(25 - Y)]$ [Y and Z are shown in Fig. 3.1(d)]. For sample N7 the phase bias imposed by one vortex located in the center of the electrode is $\Delta\varphi_v = 1.22$ rad. The geometry of the electrodes of the sample N1 is very similar to N7.

Of course, the number of vortices entering the electrodes exhibits fluctuations. In what follows we present a different approach to analyse and average out these fluctuations. First, we calculate the difference between the consecutive sweet spot fields $\Delta B_n = B_n - B_{n-1}$. The result is plotted in Fig. 6.10(b). Note that $\Delta B_n - \Delta B$ is the increase of the measured period above the vortex-free period ΔB . Note that here we treat the period as a fluctuating quantity, because vortices enter somewhat randomly. Evidently the measured period becomes larger than ΔB for $n \geq 7$. Note in passing that for $n < 7$ the period does not depend on n and can be written as $\Delta B_n = \Delta B$. The number of vortices entering the electrodes between two adjacent sweet spots, ΔN_n , can be estimated using formula $\Delta N_n / (\Delta B_n - \Delta B) = \Delta N / \Delta B_v$, which simply assumes that the number of vortices entering per period is linearly proportional to the period. Thus computed number ΔN is shown on the right axis in Fig. 6.10(b). Finally, we integrate ΔN_n with respect to n to output the total number of vortices, N_n , versus the sweet spot index n . The result is shown in Fig. 6.10(b). From this plot one can estimate that that 38 vortices enter as the index is increased by 20. Thus one obtains 1.9 vortices per period. Since the period equals 0.278 G, on average, one estimates that 6.8 vortices enter the electrodes as the field is changed by 1 G, in the case of sample N7. Since N1 has about the same size of the electrodes as N7, we used the same conversion factor 6.8 vortices per Gauss for N1.

Now we discuss our third approach to estimate the number of vortices entering the electrodes per unit B-field, $dN/dB = (N_{n+1} - N_n)/\Delta B$. This approach is based on the observation that the function N_n , computed by the algorithm outlined above, exhibits a stepwise increase as the magnetic field is increased [Fig. 6.10(c)]. The steps are made more noticeable by placing the horizontal dashed lines. The spacing between the lines is constant and they serve as guide to the eye, to make the steps more pronounced. The step size of data turns out almost constant. We speculate that each step corresponds to the entrance of a single vortex which is effectively coupled to the qubit. This scenario assumes that not all vortices present in the loop are sufficiently well coupled to the supercurrent generated by the qubit but only those which enter the area near the SQUID loop. At the same time, many other vortices get pushed in the middle of the electrode, thus making their impact on the qubit very minimal. It is naturally expected that vortices entering the electrodes near the loop would make a relatively large impact on the change of the period, $B_{n+1} - B_n$ and therefore can cause an sharp increase in the estimated N_n number. Thus the steps apparent

in Fig. 6.10(c) represent the vortices effectively coupled to the qubit, and only these vortices are relevant for our estimate of the relaxation rate. In this scenario, the total number of effectively coupled vortices equals the number of steps, i.e. equals 6. These 6 vortices have entered over the interval of 5.6 Gauss. Thus the effective entrance rate can be taken as $dN/dB=6/5.6=1.07$ vortex/G.

Finally, the experimental relaxation rates per Gauss $d\Gamma/dB$, obtained from Fig. 6.9, are 78.5 and 43.7 kHz/G for samples N1 and N7. Now these values need to be divided by 6.8, which is the rate of the vortex entrance, dN/dB . Thus we conclude that the experimental relaxation rate is $\Gamma_v = 11.5$ and $\Gamma_v = 6.4$ kHz/vortex, for samples N1 and N7, calculated using $\Gamma_v = (d\Gamma/dB)/(dN/dB)$. These values are somewhat smaller than the theoretical estimates of 89 kHz and 48 kHz/vortex. This fact serves as indirect evidence that the number of vortices is overestimated.

With the conversion factor obtained by our third method, based on the observation of the steps, the experimental relaxation rates per vortex become 73 and 41 kHz/vortex for sample N1 and N7. These are in good agreement with the calculated values, 89 and 48 kHz/vortex, for the same samples. Thus the approach based on the step counting appears to be the most accurate for the estimation of the effective number of vortices coupled to the qubit.

To understand the significance of the obtained results for the macroscopic quantum physics, it is instructive to compare the relaxation rates generated by individual vortices to the theory of localization caused by environmental dissipation. According to the Caldeira and Leggett (CL) theory [67], the particle wave function should be exponentially localized with the localization length scale estimated as $x_{CL}^2 \sim \hbar/\eta$, where η is the viscous drag coefficient of the considered particle. This theory was later generalized to the case of periodic potentials by Schmid [68] and Bulgadaev [69]. They obtained a precise value for the localization scale, namely $x_{CL}^2 = \hbar/\eta$, where $\hbar = 2\pi\hbar$ is the Planck's constant. They conclude that if the period of the potential is larger than x_{CL} then the particle becomes localized in one of the wells in the limit of zero temperature. On the other hand, If the period is smaller than x_{CL} then the particle can tunnel from one minimum to the next one even at zero temperature. It is important that the scale of the environmental localization, x_{CL} , is independent of the amplitude of the modulation of the potential energy. Thus it can provide a useful estimate even if the potential is approximately flat, which is the case for the Abrikosov vortex in the Al film in our devices. The viscous drag coefficient for a single vortex is $\eta = d \cdot \eta_1 = 9.9 \times 10^{-17}$ N·s/m, where $d = 90$ nm is the vortex length. Then the Caldeira-Leggett (CL) localization scale is $x_{CL} = \sqrt{\hbar/\eta} = 2.5 \times 10^{-9}$ m = 2.6 nm.

The CL localization scale of a vortex is the scale at which the wave function tends to collapse. This scale should be compared to the estimated smearing of the wave function of the center-of-mass of the vortex. The

smearing of the wave function can be estimated as follows, for the example of sample N1. The root-mean-square (rms) value of the Lorentz force is $F_L = d \cdot f_L = 6.1 \times 10^{-18}$ N. Then, assuming viscous motion, the rms velocity is $v = F_L/\eta = 6.2 \times 10^{-2}$ m/s. Therefore, the rms quantum fluctuations, x_v , of the position of the vortex core can be estimated as $x_v = v/\omega_{01}$. The latter relation would be exact if the motion of the vortex would be described by a classical trajectory, such that the deviations from its point of equilibrium would be proportional to $\sin(\omega_{01}t)$. In the case considered the vortex is not described by a trajectory, since it should act as a quantum particle at time scales shorter than the relaxation time of the qubit. But we assume that the relationship between the quantum fluctuation of the position and the velocity is the same as in the case of classical harmonic motion. Such assumption is motivated by the natural expectation that the vortex should behave as a quasi-classical particle. Thus we can now evaluate the rms smearing, x_v , of the wave function of the vortex center of mass occurring due to the quantum fluctuations of the Lorentz force. The result is $x_v = (F_L/\eta)/\omega_{01} = 1.5 \times 10^{-12}$ m = 1.5 pm. Here we have used the qubit frequency $f_{01} = \omega_{01}/2\pi = 6.58$ GHz for sample N1. The conclusion is that the smearing of the uncertainty of the vortex position is much smaller than the CL localization scale, $x_v \ll x_{CL}$, namely $x_{CL}/x_v = 1700$.

The CL scale provide the maximum value of the rms smearing of the wave function. When such level of smearing is achieved, the wave function collapses and the qubit experiences a decoherence event. The number of complete phase revolutions of the qubit, N_{dch} , which is needed to achieve the CL scale, at which the probability of decoherence becomes of the order of unity, can be estimated assuming that the wave function of the vortex spreads similar to a diffusive random walk. Then $N_{dch} = x_{CL}^2/x^2 = 3.0 \times 10^6$. Thus the corresponding decoherence time can be estimated as $t_{dch} \sim N_{dch}/f_{01}$. This heuristic argument can be made more precise using Eq. (6.4). From that equation, using the relations listed above, one obtains $t_{dch} = (1/2\pi)^2 N_{dch}/f_{01} = 12 \mu s$. Finally, the estimate for the relaxation rate, added to the system due to one vortex coupled to the qubit, is $\Gamma_v = 1/t_{dch} = 83$ kHz. This analysis leads to a conclusion that the relaxation rate induced by one vortex can be linked to the extent of the smearing of its wave function. The relaxation occurs typically at the time when the wave function smearing reaches the Caldeira-Leggett localization scale.

Chapter 7

Conclusion

We demonstrate the operation of the Meissner qubit, which is a transmon qubit strongly coupled to the Meissner current in the electrodes. The period of the magnetic field was set mainly by the width of the electrodes rather than the SQUID loop area. Both the frequency and the time domain measurements were performed using the circuit-QED architecture. The three time scales of T_1 , T_2^* and T_2 were measured as functions of the applied magnetic field. The increase of the relaxation rates was attributed to the radiation-free dissipation associated with the viscous motion of Abrikosov vortices pushed by the Lorentz force. Each vortex can exist in a quantum superposition of different position states for about $100 \mu\text{s}$, but eventually causes the wave function of the coupled qubit to collapse. The collapse happens when the smearing of the center-of-current position of the vortex becomes of the order of the Caldeira-Leggett dissipative localization scale. The presented Meissner qubit provides an effective and controlled coupling of the qubit to Abrikosov vortices. Such coupling provides a new tool to study vortices, which can eventually be applied to vortices harboring Majorana states.

Appendix A

Recipe

A.1 Stainless steel powder filter

In this section, we will show how the stainless steel (SS) powder filters were made. These filters are designed to filter out high-frequency components over a few GHz of whatever comes into the filters. They are in origin dissipative since high frequency signals are naturally damped by skin effect. A motivation to use such filters is to eliminate photon noise to a strongly coupled transmon-cavity system, thus improving dephasing time. Note that in the strong coupling regime, a cavity photon can shift the qubit transition frequency by ac-Stark effect, leading to photon dephasing process.

The SS power filters have two requirements: cutoff frequency, attenuation per GHz, 50 Ω characteristic impedance. The cutoff frequency is where the transmission of the filter drops by 3 dB. This frequency is found to depend on the length of the filter. The longer the filter is, the lower the cutoff frequency is. Obviously, the filter length also sets the attenuation (dB) per GHz. The longer the filter is, the higher the attenuation per GHz is. Thus, the length of the filter should be decided to meet the need for noise filtering. Meanwhile, the characteristic impedance should be closed to 50 Ω to maximize the transmission in passband—below the cutoff frequency. The characteristic impedance is determined by type of powder material, dielectric constant of the epoxy, and dimension of the center and outer conductor of the filter.

The SS power filters have similar geometry with a coaxial cable. They consist of a cylindrical copper jacket for outer conductor, two circular SMA connectors, a copper wire for inner conductor, and stainless steel powder ¹ mixed with Stycast epoxy. The filters were made in the following procedures.

1. Machine a copper rod to make outer conductor jacket.
2. Cut a copper wire (26 AWG, OD=0.016", magnet wire) to a little longer than desired length.
3. Strip off insulation at both ends of the wire about 1 mm with a razor blade.
4. Solder one end of the wire to the first SMA connector.

¹SS powder was selected rather than copper powder, because SS powder has higher attenuation and filter characteristics change less over temperature variation.

5. Insert both SMA connectors into the copper outer conductor and adjust the length of the wire such that there is less than 0.5 mm gap between the wire and the second SMA connector.
6. Tin the center pin of the second SMA.
7. Solder the unconnected end of the wire to the second SMA connector through the slit of the copper outer conductor.
8. Solder both SMA connectors to the outer conductor using a stainless steel flux . Make sure the solder sticks to the SMA outer conductors.
9. Inject the mixture of SS powder and Stycast into the copper outer conductor.
10. Bake the filter at low temperature to speed up curing. Do not heat above 65 C initially or bubbles form.
11. Fill silver paint in the recessed slit.
12. Test the filter at RT. Measure attenuation and characteristic impedance with a network analyzer. S_{21} (transmission) and S_{11} (reflection) should be measured after network analyzer calibration.

Some extra notes:

1. Machining step
 - Cut a copper rod to the right length.
 - Mill a slit on the side of the rod.
 - Drill a hole through the rod
2. Composition of the mixture of SS powder and Stycast epoxy.
 - Stycast epoxy: By weight, mix two components. (1) thermally conductive epoxy encapsulant =80% 2850 + 20% 1266, (2) catalyst LV23 = 7.5% of the total encapsulant.
 - SS powder : Stycast = 1 : 1

The two SS powder filters made had the following characteristics. First, the length the center conductor (wire) was 1/4 inch long. The attenuation rate was ~ 0.056 dB/mm/GHz. A photograph of two SS powder filters [one (filter No2) is 1/4" long, and the other one (filter No4) is 1/2" long] are shown in Fig. A.1(a). Also, the transmission versus frequency data (filter No2) at three different temperatures is plotted in Fig. A.1(b). The cutoff frequency turned out ~ 8.5 GHz.

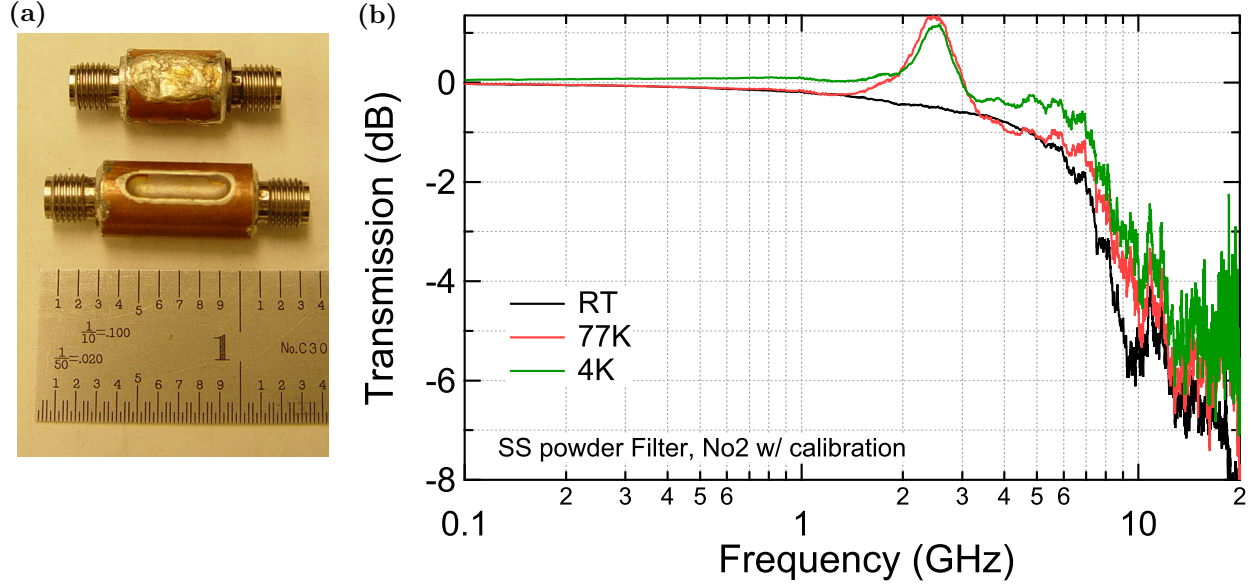


Figure A.1: (a) A photograph of two SS powder filters. The top and bottom ones have 1/4" and 1/2" long center conductors, respectively. The slot on the copper structure is to access the wire inside for soldering. The slot is covered with silver paint. (b) The transmission data versus frequency of No2 SS powder filter (1/4" long) is depicted for three different temperatures: RT, 77 K and 4.2 K. The transmission shows small temperature dependence. A bump in transmission near 2.5 GHz is an artifact from unreliable cable, not the filter transmission (see black curve instead). The cutoff frequency is ~ 8.5 GHz.

A.2 Infrared-absorbing material

It was revealed that stray infrared radiation can cause quasiparticle generation in superconducting qubit, leading to the increase of relaxation rate [55]. Thus it is advised to coat inner walls of a Faraday cage with an infrared-absorbing substance. By courtesy of Martinis' group, we made such material with their recipe as described below. The procedures to coat inner walls of a metal can are shown here.

1. Put on a mask and safety gloves.
2. Mix the following together in the following order:
 - Stycast 1266 part A: 4.00 g
 - Stycast 1266 part B: 1.12 g
 - crystalline silica (SiC) grains (MIN-U-SIL 5 - Mill creek plant): 3.00 g
 - carbon powder: 0.12 g
3. Place the mixture under vacuum to get the air bubbles out. Pump ~ 15 minutes.



Figure A.2: A photograph of aluminium Faraday cage whose inner walls are coated with black infrared-absorbing material.

4. Take a paintbrush and coat the metal can with the black mixture.
5. Throw and spread out the SiC grains over the walls of the can.
6. Heat up the can at 100 C and wait 1-2 hours until the bottom layer of the grains are firmly fixed.
7. Coat the grains thinly with the black mixture. Make sure the grains are fully coated, but do not use too much. If there is too much, the surface will become too smooth again.
8. Heat up the can so the coating solidifies in a few hours.

A photograph of completed coating on the aluminium Faraday cage is shown in Fig. A.2. The Stycast enables a solid bonding of all the materials used to the can. The surface looks rough because of mm-size SiC grains.

Appendix B

Measuring on/off ratio of microwave pulses

An on/off ratio of a microwave pulse is the ratio of the voltage amplitude in “on” state to in “off” state, $V_{\text{on}}/V_{\text{off}}$. Normally, the ratio is expressed in dB,

$$\text{On/Off ratio(dB)} = 20 \log \left(\frac{V_{\text{on}}}{V_{\text{off}}} \right) \quad (\text{B.1})$$

An illustration of a chain of microwave pulses is shown in Fig. B.1(a). The on/off ratio is a measure of how well “off” state is defined—how close to zero the amplitude is in off state. A good on/off ratio—about 80 dB—is critical in pulsed measurements of a superconducting qubit. A poor on/off ratio implied that there is a microwave leakage when no microwave signal is expected. In the case of excitation microwave pulses, such leakage can affect qubit state, e.g., the qubit is not purely in the ground state any more even in the off state of a pulse. For a readout pulse, the non-zero photon number in off state—leakage photons—induces the fluctuation of qubit transition frequency via ac-Stark effect, leading to additional photon dephasing.

We will describe how to measure such on/off ratio of a microwave pulse. The setup diagram is shown in Fig. B.1. The rectangular pulse train generated by the arbitrary waveform generator (AWG520, Tektronix), and a continuous microwave by a microwave generator are mixed by an RF mixer, and fed into a spectrum analyzer (H8566B, Hewlett-Packard). The spectrum analyzer is externally triggered by a marker signal from the AWG520, to get a stationary signal trace on the screen of the spectrum analyzer. The idea is to measure the amplitude (envelope) of microwave pulses by continuously monitoring the frequency component of the pulses. For that purpose, we set the *center frequency* to be same as that (ω_{LO}) of the microwave generator, and *span* to be 0 Hz. The data is taken and transferred to a computer via GPIB and plotted using a Labview program. Programmatically, on/off ratio as a function of various parameters such as microwave power and frequency, can be measured to find optimum conditions. For example, in Fig. B.2, on/off measurement of two mixers in series (M8-0420, Markis) is depicted. The LO power was 5 dBm and IF voltage was 1.9 V. The amplitudes of the measured microwave signal are expressed in dBm unit, so the on/off ratio in dB can be obtained by subtracting off-state power from on-state power. The on/off ratio is close to 70 dB in

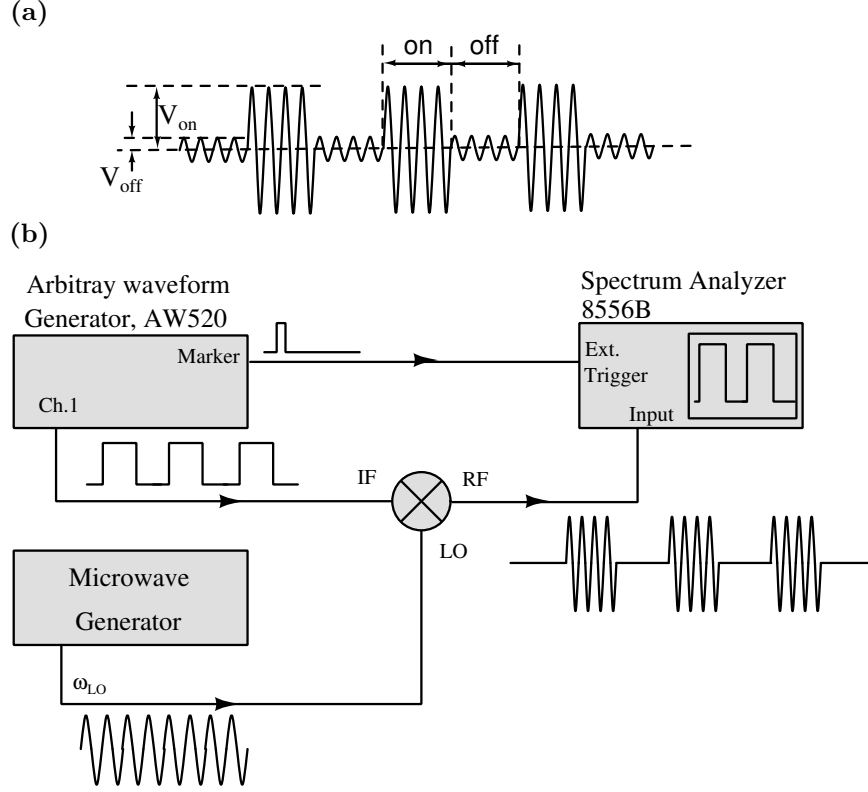


Figure B.1: (a) An illustration of a chain of microwave pulses. V_{on} is the amplitude of microwave pulse in “on” state, and V_{off} in “off” state. The on/off ratio is defined by $20 \log(V_{\text{on}}/V_{\text{off}})$ in dB—ratio $V_{\text{on}}/V_{\text{off}}$ in log. (b) Schematic diagram of the electronic setup for measuring the on/off ratio of microwave pulses. The voltage pulses created by an arbitrary waveform generator (AWG) is mixed with a continuous microwave by an RF mixer. The mixed signal is fed into a spectrum analyzer and the Fourier component at ω_{LO} is measured. Such frequency component represents the voltage envelope of the microwave pulses shown in (a), which enables us to measure the ratio of $V_{\text{on}}/V_{\text{off}}$.

the frequency range of 5.5- 8 GHz. In other frequency range, the on/off ratio is not high enough for qubit measurement.

It is important to note that the on/off ratio also depends on the LO power. In general, the on/off ratio increases as the LO power does, until the LO power reaches the specified LO drive level ¹. Therefore, at a fixed LO frequency, it is necessary to find the best on/off ratio by scanning the LO power.

Since the LO power affects the on/off ratio, the LO power should be fixed and instead the IF power should be changed when the pulse height needs to be changed, e.g., for Rabi pulses calibration. If IF power can not be low enough to set the desired RF output power, it would be better to use a variable attenuator with a wide dynamic range, while LO and IF power are fixed.

Finally, we mention that the non-zero off-state power—or microwave amplitude intrinsically comes from the leakage of microwave from the LO port to RF port. A measure of leakage is specified as a term “isolator”

¹The LO drive level is the power required for proper operation of the mixer—power required to switch the mixer diodes fully on and off.

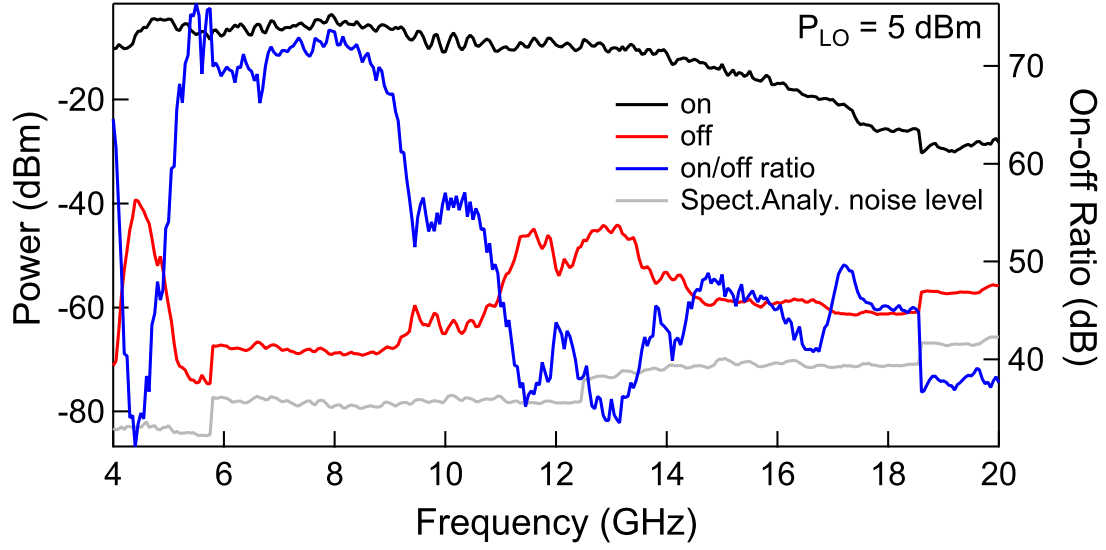


Figure B.2: The on/off ratio (dB) versus LO frequency ω_{LO} is plotted in blue solid line. Also the output powers of on-state and off-state are shown. The on/off ratio is obtained by subtracting the off-state power from the on-state power. The noise level of the spectrum analyzer is plotted to show that the off-state power is higher than the noise level—off-state power is not limited by the noise level.

in dB, and the isolation is at best about 40 dB. Thus, to achieve high on/off ratio (> 60 dB), two mixers can be used in series to increase the total isolation. In some frequency range, we had to use three mixers in series.

Appendix C

Influence of microwave leakage on time-domain measurement

When creating microwave pulses for the readout and excitation of a qubit, it is critical to have a good on/off ratio. The low on/off ratio implies that there can exist non-zero qubit excitation in time when the microwave amplitude should be small enough not to affect the qubit rotation. Here is an example of what would happen during Rabi oscillation measurement, if there is a significant leakage of microwave in off-state of pulses. In Fig. C.1(a), the Rabi oscillations are shown for zero detuning (black solid circle) and non-zero detuning (red open circle) case. Here the detuning is the difference between qubit transition frequency and qubit excitation (or spectroscopic) frequency. At $\Delta t = 0$, the qubit is in the ground state. The detuning is just $\Delta/2\pi = 0.1$ MHz, which is much smaller than the Rabi frequency 4.9 MHz. Thus the Rabi amplitude of non-zero detuning case should be almost the same as that of zero detuning case. Nevertheless, the Rabi amplitude of zero detuning case is much smaller, about one third of the amplitude of detuned case. This is because a microwave leakage makes a statistical mixture of the ground and excited state. Since there is always a probability to find the qubit in the excited states, the V_H never reaches the minimum voltage, ~ 7 mV. The image plot of the transmission V_H as a function of pulse length and spectroscopic frequency is plotted in Fig. C.1(b). Similarly, the transmission does not swing in the full range, unlike non-zero detuning case. In addition to the Rabi oscillation, the relaxation time and Ramsey fringe measurements are also affected by the microwave leakage as shown in Fig. C.1(c) and Fig. C.1(d). In the case of the relaxation measurement, the qubit state for zero detuning case, as evidenced by the high transmission, does not decay fully to the ground state.

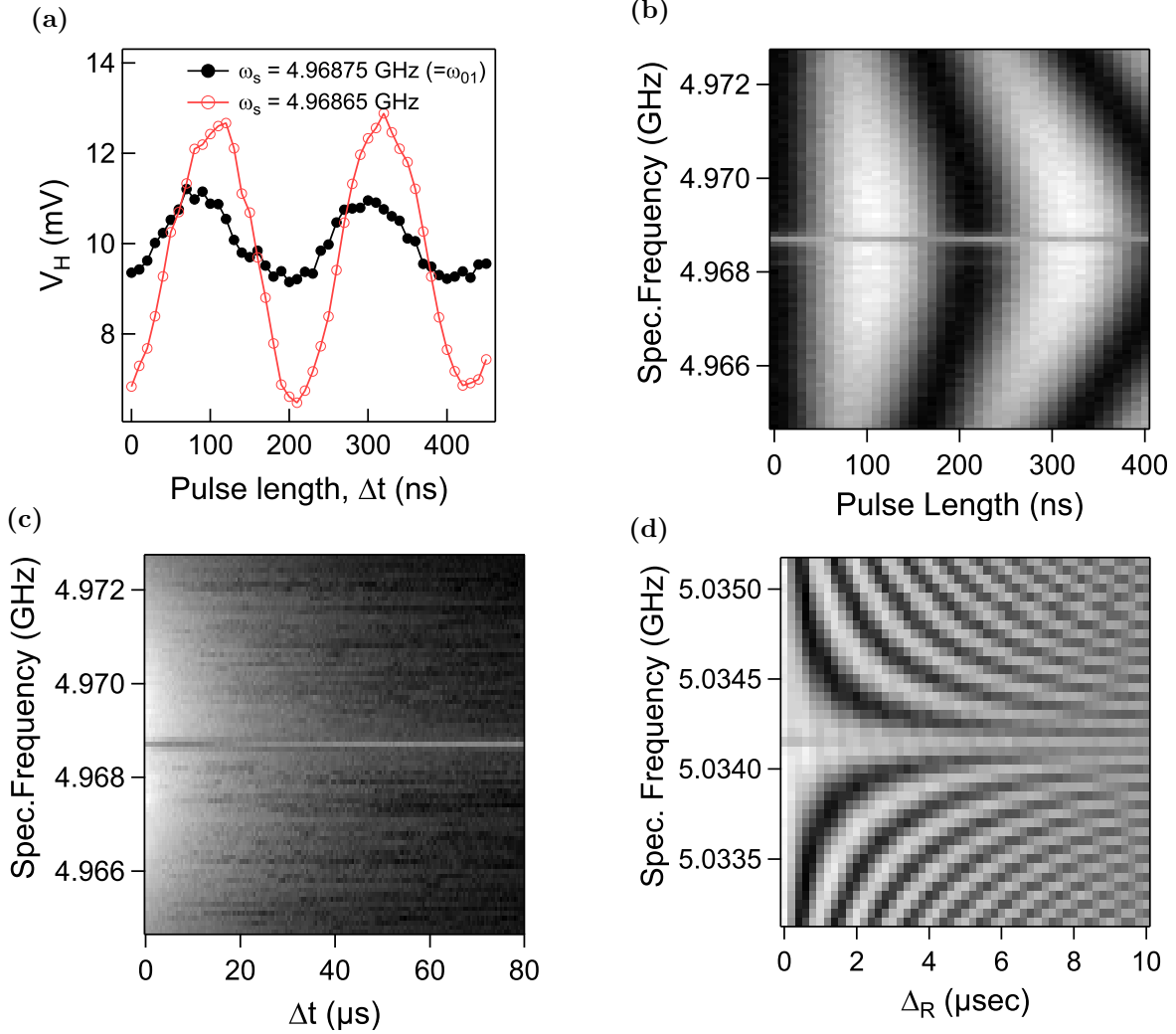


Figure C.1: (a) Rabi oscillations for zero and non-zero detuning case. Note that the oscillation amplitude is smaller in zero detuning (black solid circle) than in non-zero detuning (red open circle), due to the leakage in qubit excitation pulse. (b) 2D plot of transmission as a function of pulse length and spectroscopic frequency, illustrating normal Rabi oscillation in non-zero detuning and unusual oscillation in zero detuning. (c) 2D plot of transmission as a function of time interval and spectroscopic frequency for relaxation time measurement. Note that the transmission does not decay to the value of the ground state for zero detuning, indicating there is still a probability to find the qubit in the excited state due to the leakage of excitation microwave pulse. (d) 2D plot of transmission as a function of spectroscopic frequency and time separation between two $\pi/2$ pulses. It is a bit hard to see, but the transmission can be seen a bit low (dark image) in zero detuning case, where the qubit is supposed to be in the excited state (brightest image).

Appendix D

Creating a phase-tunable microwave pulse

We encounter times when the phase of spectroscopic microwave pulse needs to be tuned. Such microwave signal can be created using a continuous microwave source and an IQ mixer. An IQ mixer can be thought of as having two mixers inside. LO signal is split into two signals inside an IQ mixer, and one of the signal is phase-shifted by 90 degree. Then those two signals are mixed with voltages fed into I and Q separately, and the mixed signals are combined to give RF output. To see how the phase of output RF signal is changed, let $V(t)$ denote the LO signal, $V(t) = \sin(\omega_s t)$. Then the output RF signal $V_{\text{out}}(t)$ is given by

$$V_{\text{out}}(t) \propto I \sin(\omega_s t) + Q \cos(\omega_s t) \quad (\text{D.1})$$

$$= \sqrt{I^2 + Q^2} \sin(\omega_s t + \phi) \quad (\text{D.2})$$

$$= R \sin(\omega_s t + \phi), \quad (\text{D.3})$$

where $\phi = \tan^{-1}(Q/I)$ is the phase shift with respect to the input microwave. What the last expression tells us is that by keeping $R = \sqrt{I^2 + Q^2}$ constant, the phase ϕ can be tuned by changing the voltage ratio Q/I . For example, I and Q voltages can be generated from an arbitrary waveform generator as in Fig.D.1.

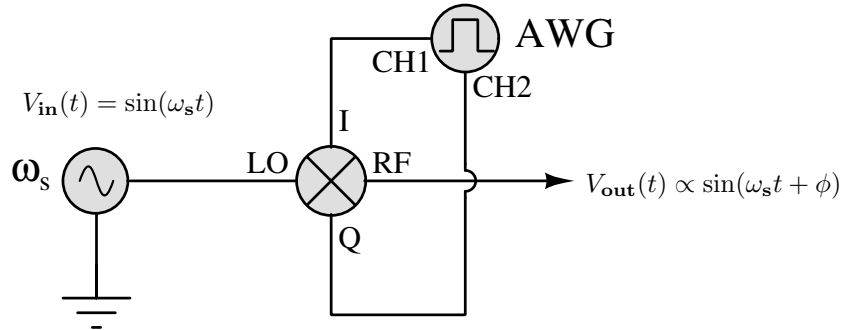


Figure D.1: Schematic diagram for creating a phase-tunable microwave pulse. The input microwave $V_{\text{in}}(t)$ at LO is mixed with I and Q signals of the arbitrary waveform generator to output the microwave signal $V_{\text{out}}(t)$ with a phase shift ϕ . The phase shift can be tunable by setting I and Q voltage levels: $\phi = \tan^{-1}(Q/I)$.

Appendix E

Quantum mechanical description in a rotating frame

One can transform Hamiltonian in the lab frame to the one in a rotating frame. The time evolution of a state $|\Psi\rangle$ with Hamiltonian \hat{H} is described by the time-dependent Schrödinger equation:

$$i\hbar \frac{d|\Psi\rangle}{dt} = \hat{H}|\Psi\rangle \quad (\text{E.1})$$

Let's consider a unitary operator \hat{U} of the form

$$\hat{U} = e^{-i\hat{A}t/\hbar}, \quad (\text{E.2})$$

by which we get the new state $|\Phi_R\rangle$ in a rotating frame,

$$|\Psi_R\rangle = \hat{U}^\dagger |\Psi\rangle \quad (\text{E.3})$$

The state $|\Psi_R\rangle$ would be *stationary* in the rotating frame. Now we derive the new Hamiltonian \hat{H}_R which satisfies the time-dependent Schrödinger equation.

$$i\hbar \frac{d|\Psi_R\rangle}{dt} = i\hbar \frac{d\hat{U}^\dagger |\Psi\rangle}{dt} \quad (\text{E.4})$$

$$= i\hbar \frac{d\hat{U}^\dagger}{dt} |\Psi\rangle + i\hbar \hat{U}^\dagger \frac{d|\Psi\rangle}{dt} \quad (\text{E.5})$$

$$= \hat{U}^\dagger \hat{H} |\Psi\rangle - \hat{A} \hat{U}^\dagger |\Psi\rangle \quad (\text{E.6})$$

$$= \left(\hat{U}^\dagger \hat{H} \hat{U} - \hat{A} \right) \hat{U}^\dagger |\Psi\rangle \quad (\text{E.7})$$

$$= \left(\hat{U}^\dagger \hat{H} \hat{U} - \hat{A} \right) |\Psi_R\rangle \quad (\text{E.8})$$

$$= \hat{H}_R |\Psi_R\rangle \quad (\text{E.9})$$

Therefore, we obtain the new Hamiltonian in the rotating frame,

$$\hat{H}_R = \hat{U}^\dagger \hat{H} \hat{U} - \hat{A} \quad (\text{E.10})$$

References

- [1] Shor, P. Algorithms for quantum computation: discrete logarithms and factoring. In , *35th Annual Symposium on Foundations of Computer Science, 1994 Proceedings*, 124–134 (1994).
- [2] Grover, L. K. A fast quantum mechanical algorithm for database search. In *Proceedings of the Twenty-eighth Annual ACM Symposium on Theory of Computing*, STOC '96, 212–219 (ACM, New York, NY, USA, 1996).
- [3] Grover, L. K. Quantum mechanics helps in searching for a needle in a haystack. *Phys. Rev. Lett.* **79**, 325–328 (1997).
- [4] Feynman, R. P. Simulating physics with computers. *International Journal of Theoretical Physics* **21**, 467–488 (1982).
- [5] Devoret, M. H. & Schoelkopf, R. J. Superconducting Circuits for Quantum Information: An Outlook. *Science* **339**, 1169–1174 (2013).
- [6] Awschalom, D. D., Bassett, L. C., Dzurak, A. S., Hu, E. L. & Petta, J. R. Quantum Spintronics: Engineering and Manipulating Atom-Like Spins in Semiconductors. *Science* **339**, 1174–1179 (2013). 00108.
- [7] Monroe, C. & Kim, J. Scaling the Ion Trap Quantum Processor. *Science* **339**, 1164–1169 (2013). 00067.
- [8] DiVincenzo, D. P. The Physical Implementation of Quantum Computation. *Fortschr. Phys.* **48**, 771–783 (2000).
- [9] Shor, P. W. Scheme for reducing decoherence in quantum computer memory. *Phys. Rev. A* **52**, R2493–R2496 (1995).
- [10] Makhlin, Y., Schön, G. & Shnirman, A. Quantum-state engineering with josephson-junction devices. *Rev. Mod. Phys.* **73**, 357–400 (2001).
- [11] Devoret, M. H. & Martinis, J. M. Course 12 superconducting qubits. In Daniel Estve, J.-M. R. & Dalibard, J. (eds.) *Quantum Entanglement and Information Processing (Les Houches Session LXXIX)*, vol. 79 of *Les Houches*, 443 – 485 (Elsevier, 2004).
- [12] Clarke, J. & Wilhelm, F. K. Superconducting quantum bits. *Nature* **453**, 1031–1042 (2008).
- [13] Nakamura, Y., Pashkin, Y. A. & Tsai, J. S. Coherent control of macroscopic quantum states in a single-cooper-pair box. *Nature* **398**, 786–788 (1999).
- [14] Martinis, J. M., Nam, S., Aumentado, J. & Urbina, C. Rabi oscillations in a large josephson-junction qubit. *Phys. Rev. Lett.* **89**, 117901 (2002).
- [15] Friedman, J. R., Patel, V., Chen, W., Tolpygo, S. K. & Lukens, J. E. Quantum superposition of distinct macroscopic states. *Nature* **406**, 43–46 (2000).
- [16] van der Wal, C. H. *et al.* Quantum superposition of macroscopic persistent-current states. *Science* **290**, 773–777 (2000).

- [17] Barends, R. *et al.* Coherent josephson qubit suitable for scalable quantum integrated circuits. *Phys. Rev. Lett.* **111**, 080502 (2013).
- [18] Schoelkopf, R. J. & Girvin, S. M. Wiring up quantum systems. *Nature* **451**, 664–669 (2008).
- [19] Astafiev, O., Pashkin, Y. A., Yamamoto, T., Nakamura, Y. & Tsai, J. S. Single-shot measurement of the josephson charge qubit. *Phys. Rev. B* **69**, 180507 (2004).
- [20] Bertet, P. *et al.* Dephasing of a superconducting qubit induced by photon noise. *Phys. Rev. Lett.* **95**, 257002 (2005).
- [21] Martinis, J. M. *et al.* Decoherence in josephson qubits from dielectric loss. *Phys. Rev. Lett.* **95**, 210503 (2005).
- [22] Neeley, M. *et al.* Transformed dissipation in superconducting quantum circuits. *Phys. Rev. B* **77**, 180508 (2008).
- [23] Song, C. *et al.* Microwave response of vortices in superconducting thin films of Re and Al. *Phys. Rev. B* **79**, 174512 (2009).
- [24] Oliver, W. D. & Welander, P. B. Materials in superconducting quantum bits. *MRS Bulletin* **38**, 816–825 (2013).
- [25] Koch, J. *et al.* Charge-insensitive qubit design derived from the cooper pair box. *Phys. Rev. A* **76**, 042319 (2007).
- [26] Paik, H. *et al.* Observation of high coherence in josephson junction qubits measured in a three-dimensional circuit qed architecture. *Phys. Rev. Lett.* **107**, 240501 (2011).
- [27] Rigetti, C. *et al.* Superconducting qubit in a waveguide cavity with a coherence time approaching 0.1 ms. *Phys. Rev. B* **86**, 100506 (2012).
- [28] Beenakker, C. Search for Majorana Fermions in Superconductors. *Annual Review of Condensed Matter Physics* **4**, 113–136 (2013).
- [29] Ginossar, E. & Grosfeld, E. Microwave transitions as a signature of coherent parity mixing effects in the Majorana-transmon qubit. *Nature Communications* **5** (2014).
- [30] Wallraff, A. *et al.* Strong coupling of a single photon to a superconducting qubit using circuit quantum electrodynamics. *Nature* **431**, 162–167 (2004).
- [31] Houck, A. A. *et al.* Generating single microwave photons in a circuit. *Nature* **449**, 328–331 (2007).
- [32] Abdumalikov, A. A., Astafiev, O., Nakamura, Y., Pashkin, Y. A. & Tsai, J. Vacuum rabi splitting due to strong coupling of a flux qubit and a coplanar-waveguide resonator. *Phys. Rev. B* **78**, 180502 (2008).
- [33] Petersson, K. D. *et al.* Circuit quantum electrodynamics with a spin qubit. *Nature* **490**, 380–383 (2012).
- [34] Ku, J., Manucharyan, V. & Bezryadin, A. Superconducting nanowires as nonlinear inductive elements for qubits. *Phys. Rev. B* **82**, 134518 (2010).
- [35] Brenner, M. W. *et al.* Cratered lorentzian response of driven microwave superconducting nanowire-bridged resonators: Oscillatory and magnetic-field induced stochastic states. *Phys. Rev. B* **83**, 184503 (2011).
- [36] Belkin, A., Brenner, M., Aref, T., Ku, J. & Bezryadin, A. LittleParks oscillations at low temperatures: Gigahertz resonator method. *Applied Physics Letters* **98**, 242504 (2011).
- [37] Mooij, J. E. & Nazarov, Y. V. Superconducting nanowires as quantum phase-slip junctions. *Nat Phys* **2**, 169–172 (2006).

- [38] Astafiev, O. V. *et al.* Coherent quantum phase slip. *Nature* **484**, 355–358 (2012).
- [39] Peltonen, J. T. *et al.* Coherent flux tunneling through NbN nanowires. *Physical Review B* **88**, 220506 (2013).
- [40] Josephson, B. D. The discovery of tunnelling supercurrents. *Reviews of Modern Physics* **46**, 251 (1974).
- [41] Rabi, I. I. Space quantization in a gyrating magnetic field. *Phys. Rev.* **51**, 652–654 (1937).
- [42] Ithier, G. *et al.* Decoherence in a superconducting quantum bit circuit. *Phys. Rev. B* **72**, 134519 (2005).
- [43] Ramsey, N. F. A molecular beam resonance method with separated oscillating fields. *Phys. Rev.* **78**, 695–699 (1950).
- [44] Raimond, J. M., Brune, M. & Haroche, S. Manipulating quantum entanglement with atoms and photons in a cavity. *Reviews of Modern Physics* **73**, 565–582 (2001).
- [45] Blais, A., Huang, R.-S., Wallraff, A., Girvin, S. M. & Schoelkopf, R. J. Cavity quantum electrodynamics for superconducting electrical circuits: An architecture for quantum computation. *Phys. Rev. A* **69**, 062320 (2004).
- [46] Schuster, D. I. *et al.* ac Stark Shift and Dephasing of a Superconducting Qubit Strongly Coupled to a Cavity Field. *Physical Review Letters* **94**, 123602 (2005).
- [47] Lamb, W. E. & Retherford, R. C. Fine structure of the hydrogen atom by a microwave method. *Phys. Rev.* **72**, 241–243 (1947).
- [48] Yoscovits, Z. R. *STUDY OF THE EFFECTS OF SURFACE CLADDING ON 3D TRANSMON*. Ph.D. thesis, University of Illinois at Urbana-Champaign (2014).
- [49] Dolan, G. J. Offset masks for lift-off photoprocessing. *Applied Physics Letters* **31**, 337 (1977).
- [50] Pop, I. M. *et al.* Fabrication of stable and reproducible submicron tunnel junctions. *Journal of Vacuum Science & Technology B* **30**, 010607 (2012).
- [51] Quintana, C. M. *et al.* Characterization and reduction of microfabrication-induced decoherence in superconducting quantum circuits. *Applied Physics Letters* **105**, – (2014).
- [52] Deppe, F., Saito, S., Tanaka, H. & Takayanagi, H. Determination of the capacitance of nm scale josephson junctions. *Journal of Applied Physics* **95**, 2607–2613 (2004).
- [53] Milliken, F. P., Rozen, J. R., Keefe, G. A. & Koch, R. H. 50 characteristic impedance low-pass metal powder filters. *Review of Scientific Instruments* **78**, – (2007).
- [54] Recipe provided by John. Martinis.
- [55] Barends, R. *et al.* Minimizing quasiparticle generation from stray infrared light in superconducting quantum circuits. *Applied Physics Letters* **99**, – (2011).
- [56] How-to: Dilution refrigerator operation Manual in the publication tab in Bezryadin group homepage.
- [57] Reed, M. D. *et al.* High-fidelity readout in circuit quantum electrodynamics using the jaynes-cummings nonlinearity. *Phys. Rev. Lett.* **105**, 173601 (2010).
- [58] Schreier, J. A. *et al.* Suppressing charge noise decoherence in superconducting charge qubits. *Phys. Rev. B* **77**, 180502 (2008).
- [59] Hopkins, D. S., Pekker, D., Goldbart, P. M. & Bezryadin, A. Quantum interference device made by dna templating of superconducting nanowires. *Science* **308**, 1762–1765 (2005).
- [60] Pekker, D., Bezryadin, A., Hopkins, D. S. & Goldbart, P. M. Operation of a superconducting nanowire quantum interference device with mesoscopic leads. *Phys. Rev. B* **72**, 104517 (2005).

- [61] Sears, A. P. *et al.* Photon shot noise dephasing in the strong-dispersive limit of circuit qed. *Phys. Rev. B* **86**, 180504 (2012).
- [62] Maksimov, I. & Maksimova, G. Stability limits, structure, and relaxation of a mixed state in superconducting films with an edge barrier. *JETP Lett.* **65**, 423–429 (1997).
- [63] Pearl, J. Current distribution in superconducting films carrying quantized fluxoids. *App. Phys. Lett.* **5**, 65–66 (1964).
- [64] Tinkham, M. *Introduction to Superconductivity*, chap. 5 (McGraw-Hill, Inc., 1996), second edn.
- [65] Romijn, J., Klapwijk, T. M., Renne, M. J. & Mooij, J. E. Critical pair-breaking current in superconducting aluminum strips far below t_c . *Phys. Rev. B* **26**, 3648–3655 (1982).
- [66] Golod, T., Rydh, A. & Krasnov, V. M. Detection of the phase shift from a single abrikosov vortex. *Phys. Rev. Lett.* **104**, 227003 (2010).
- [67] Caldeira, A. O. & Leggett, A. J. Influence of dissipation on quantum tunneling in macroscopic systems. *Phys. Rev. Lett.* **46**, 211–214 (1981).
- [68] Schmid, A. Diffusion and localization in a dissipative quantum system. *Phys. Rev. Lett.* **51**, 1506–1509 (1983).
- [69] Bulgadaev, S. A. Phase diagram of a dissipative quantum system. *JTEP Lett.* **39**, 315 (1984).